APPLICATIONS OF HYDROFOILS WITH LEADING EDGE PROTUBERANCES

Final Technical Report

for Office of Naval Research contract N00014-08-1-1043

covering the period August 1, 2008 to December 31, 2011

Hamid Johari

Mechanical Engineering Department
California State University, Northridge
Northridge, CA 91330

Tel: (818) 677-3099
Fax: (818) 677-7062
email: hjohari@csun.edu

Administrative Representative for California State University, Northridge

Scott Perez, Director
Research and Sponsored Projects

University Hall 265, Mail Drop: 8232
California State University, Northridge
Northridge, CA 91330

Tel: (818) 677-2901
Fax: (818) 677-4691
email: scott.perez@csun.edu

REPORT DOCUMENTATION PAGE

1. REPORT DATE *(DD-MM-YYYY)*	2. REPORT TYPE	3. DATES COVERED *(From - To)*
03/30/2012	Final Technical Report	01-08-2008 to 31-12-2011

4. TITLE AND SUBTITLE
Applications of Hydrofoils with Leading Edge Protuberances

5a. CONTRACT NUMBER

5b. GRANT NUMBER
N00014-08-1-1043

5c. PROGRAM ELEMENT NUMBER

6. AUTHOR(S)
Johari, Hamid

5d. PROJECT NUMBER

5e. TASK NUMBER

5f. WORK UNIT NUMBER

7. PERFORMING ORGANIZATION NAME(S) AND ADDRESS(ES)
Mechanical Engineering Department
California State University, Northridge
Northridge, CA 91330

8. PERFORMING ORGANIZATION REPORT NUMBER

9. SPONSORING/MONITORING AGENCY NAME(S) AND ADDRESS(ES)
Office of Naval Research
875 North Randolph Street
Arlington, VA 22203-1995

10. SPONSOR/MONITOR'S ACRONYM(S)
ONR

11. SPONSOR/MONITOR'S REPORT NUMBER(S)

12. DISTRIBUTION/AVAILABILITY STATEMENT
Approved for public release; distribution is unlimited.

13. SUPPLEMENTARY NOTES

14. ABSTRACT
The leading edge modified hydrofoils generally create lift equal to or greater than their baseline counterparts at higher angles of attack (beyond the baseline stall angle) whereas at lower angles of attack the baseline models produce lift coefficients equal to or greater than the modified models. The drag coefficients of all modified hydrofoils are either equal to or greater than their baseline counterparts. The relative increase in drag associated with the leading edge protuberances, in turn, results in the lift-to-drag ratio for the modified hydrofoils to be less than or equal to the baseline models. The incipient cavitation numbers for leading edge modified hydrofoils were consistently greater than their their baseline counterparts.

15. SUBJECT TERMS
Sinusoidal leading edge hydrofoils, tip vortex, cavitation

16. SECURITY CLASSIFICATION OF:			17. LIMITATION OF ABSTRACT	18. NUMBER OF PAGES	19a. NAME OF RESPONSIBLE PERSON
a. REPORT	b. ABSTRACT	c. THIS PAGE			
U	U	U		122	19b. TELEPHONE NUMBER *(Include area code)*

SYNOPSIS

The primary objective of this experimental study was to investigate the effects of high freestream velocity (up to 9 m/s) and Reynolds number, finite-span, and planform geometry on the performance of hydrofoils with sinusoidal leading edge protuberances. As part of high-speed testing, the onset and pattern of cavitation on the hydrofoils were also examined. The leading edge geometry was inspired by the protuberances on the humpback whale flippers and our previous work on full-span hydrofoil models with a sinusoidal leading edge. Force and moment measurements along with qualitative and quantitative (PIV) flow visualization were carried out in water tunnel experiments over an angle of attack range of $-9° \leq \alpha \leq 30°$ on full-span and finite-span hydrofoil models with several different planforms and protuberance geometries. The baseline hydrofoil had the NACA 63_4-021 profile, and the planform geometries included a full-span model which spanned the water tunnel width, a finite-span rectangular model, a swept leading edge model, and a flipper model that resembled the morphology of the humpback whale flipper. The sinusoidal leading edge geometries considered consisted of three amplitudes of 2.5%, 5%, and 12% as well as wavelengths of 25% and 50% of the local chordlength.

Force measurements indicate that the leading edge modified hydrofoils generally create lift equal to or greater than their baseline counterparts at higher angles of attack (beyond the baseline stall angle) whereas at lower angles of attack the baseline models produce lift coefficients equal to or greater than the modified models. With the exception of the leading edge modified flipper model over a limited range of angles of attack, the drag coefficients of all modified hydrofoils are either equal to or greater than their baseline counterparts. The relative increase in drag associated with the leading edge protuberances, in turn, results in the lift-to-drag ratio for the modified hydrofoils to be less than or equal to the baseline models over the entire angle of attack range. Flow visualization shows that streamwise vortical structures emanating from the shoulders of the protuberances generate spanwise flow on the hydrofoils even at relatively low angles. Flow remains attached on the protuberance peaks at higher angles of attack compared to the baseline while the flow separates earlier behind the protuberance troughs. Cavitation tests reveal that modified hydrofoils cavitate in pockets behind the troughs of protuberances in contrast to sheet cavitation on the baseline models under similar conditions. The incipient cavitation numbers for leading edge modified hydrofoils were consistently greater than their baseline counterparts.

Experimental Technique

All experiments reported here, with the exception of low-speed Particle Image Velocimetry (PIV) work, were carried out at the Naval Undersea Warfare Center (NUWC) high-speed closed loop water tunnel facility in Newport, RI. The water tunnel test section is 0.30 m square, and capable of reaching freestream velocities of up to $U_\infty = 10.0$ m/s. The freestream velocity in all experiments was monitored at a point in the center of the water tunnel test section and 0.66 m upstream of the hydrofoil models using a Laser Doppler Velocimeter (LDV). Monitoring and adjustment of the freestream velocity was needed due to the variation in the blockage caused by the different models and angles of attack. To account for the solid and wake blockage effects beyond freestream variations, all measured forces and moments were corrected using the methods outlined by Pope and Ray (1984). A set of low-speed PIV experiments was conducted in the Worcester Polytechnic Institute (WPI) low-speed water tunnel, which had a 0.61 m square test section, at 0.15 m/s freestream velocity. For all the experiments, the freestream velocities ranged from $0.15 \leq U_\infty \leq 9.0$ m/s, corresponding to chordwise Reynolds numbers in the range of $1.5 \times 10^4 \leq Re_c \leq 9.0 \times 10^5$.

Various hydrofoil models, with sinusoidal leading edge geometries similar to the wavelength and amplitude range of the protuberances found on the humpback whale flipper, were designed using Pro-Engineer and SolidWorks Computer-Aided Design (CAD) software suites. All hydrofoils had an underlying NACA 63_4-021 profile, which is symmetric with a maximum thickness to chord ratio of 21% at 40% of chordlength. This profile was chosen for its similarity to the humpback whale flipper cross-section. Four sets of hydrofoil models distinguished by the planform geometry were created: (a) full-span rectangular models bounded by the tunnel walls at the edges, (b) finite-span rectangular planform models with a rounded tip, (c) swept-leading edge hydrofoil models, and (d) flipper models whose planform closely resembled the morphology of the humpback whale flipper. For all models, the leading edge geometries were defined by sinusoidal patterns with fixed amplitude, A, and wavelength, λ. With the exception of the flipper models, the leading edge protuberance amplitude (and wavelength) was a constant fraction of the mean chordlength, c. The local chordlength, c_z, as a function of spanwise coordinate z of the modified hydrofoils can be described by the following expression.

$$c_z = c + A\sin(\frac{2\pi z}{\lambda} - \frac{\pi}{2})$$

Three amplitudes of $A = 0.025c$, $A = 0.05c$, and $A = 0.12c$, along with two wavelengths $\lambda = 0.25c$, and $\lambda = 0.50c$ were examined. Henceforth the leading edge geometries are described by the following nomenclature: 8 and 4 represent wavelengths of $\lambda = 0.25c$, and $\lambda = 0.50c$, respectively, and S (small), M (medium), and L (large) represent amplitudes of $A = 0.025c$, $A = 0.050c$, and $A = 0.120c$, respectively. These values were chosen as they are representative of those found on the humpback whale flippers. Table 1shows the combination of parameters for the hydrofoil models tested.

Table 1. Nomenclature used to describe modified leading edge hydrofoil models.

	$A = 0.025c$	$A = 0.050c$	$A = 0.120c$
$\lambda = 0.25c$	8S	8M	8L
$\lambda = 0.50c$	4S	4M	4L

For each set of hydrofoil models, the mean chordlength was kept the same. This was done to ensure that the planform area of all hydrofoil models in a set remained equal. All modified hydrofoil models were compared to a protuberance-free, baseline hydrofoil with the same planform.

Full-span hydrofoils

Two hydrofoil models of mean chordlength $c = 102$ mm and span $b = 305$ mm, shown in Figure 1, spanning the entirety of the NUWC water tunnel test section, were used in the examination of the force and moment characteristics of the full-span geometry. The hydrofoils were machined out of aluminum stock on a 3-axis CNC machine and anodized matte black to generate contrast for flow visualization experiments. One protuberance pattern (4L) was studied. This specific pattern was chosen because it was representative of significant performance variations from the baseline in the past experiments of Johari et al. (2007).
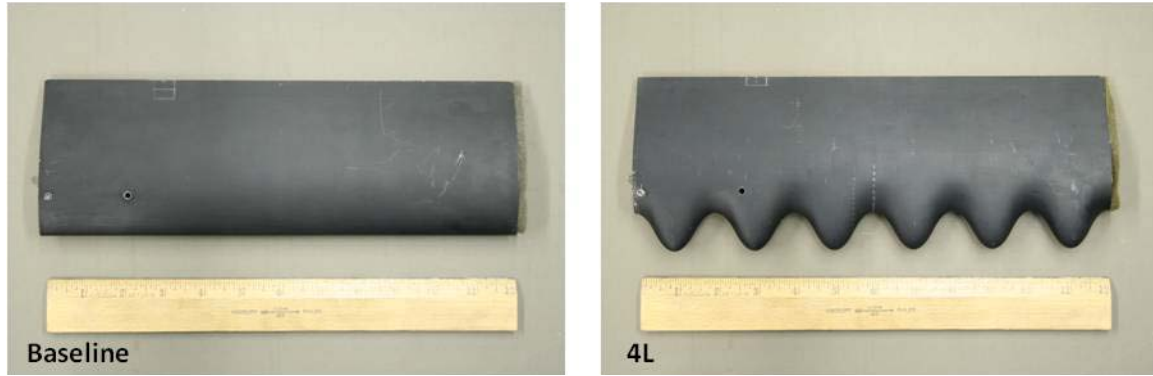
Figure 1. Full-span hydrofoil models of 305 mm span.

A second 4L hydrofoil model with mean chordlength of $c = 102$ mm and span $b = 305$ mm was also designed and fabricated using a rapid prototyping stereolithography apparatus (SLA), see Figure 2. This model was used in the low-speed PIV experiments in the WPI water tunnel. The sinusoidal leading edge geometry of this hydrofoil was identical to the leading edge of the aluminum 4L hydrofoil in Figure 1. However, to rule out possible boundary effects, the spanwise pattern of protuberances was shifted by one-half wavelength.
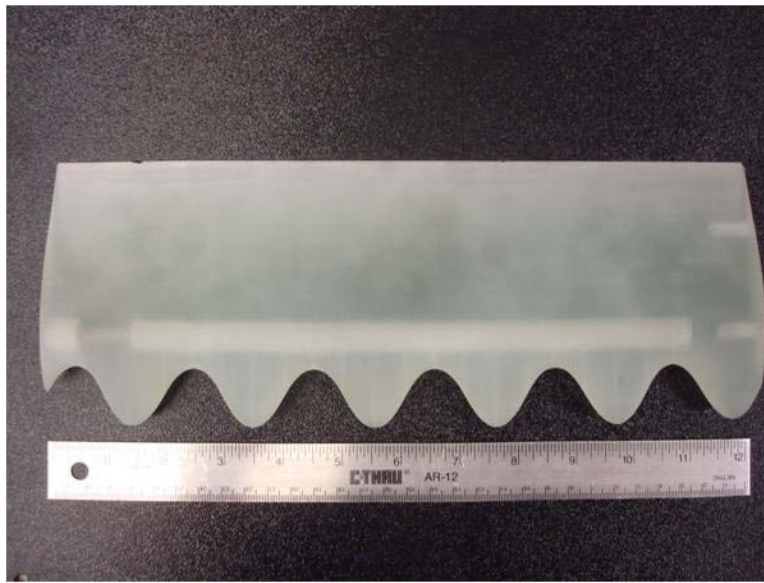

Figure 2. 4L SLA hydrofoil used in low-speed PIV water tunnel experiments.

Finite-span hydrofoils

Seven rectangular hydrofoils of mean chordlength $c = 102$ mm and span $b = 219$ mm with semi-span aspect ratio $AR = 2.15$ (including the cap) were designed and fabricated in the same

manner as the full-span aluminum hydrofoils. This set of hydrofoils was used to determine the effect of leading edge protuberances on finite-span models and therefore, by definition, had a free tip. To eliminate the sharp, flat edge at the free tip, rounded caps were attached to the free end of the hydrofoils. The finite-span rectangular hydrofoil models are shown in Figure 3.
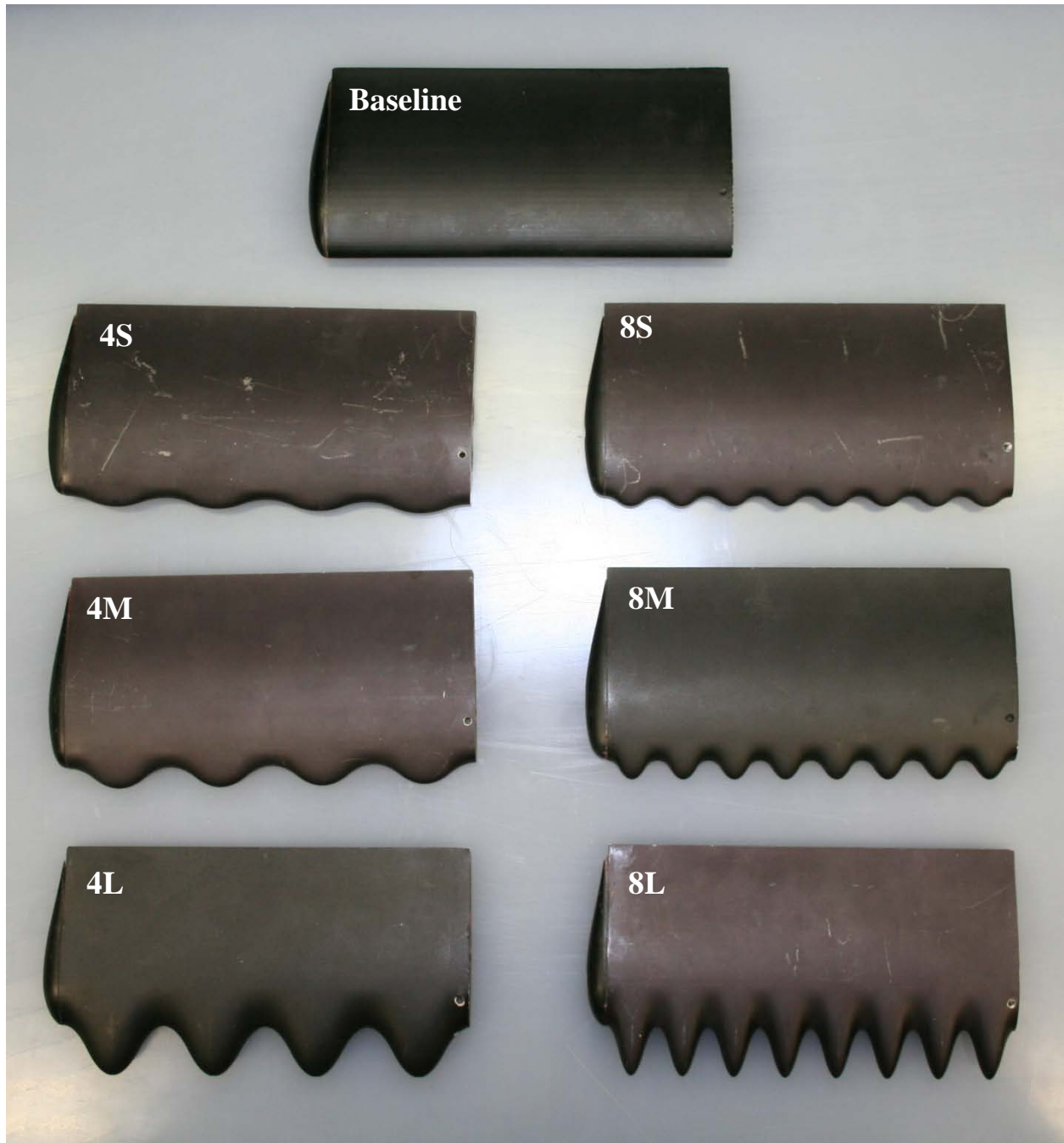

Figure 3. Finite-span hydrofoil models with end caps.

Swept leading edge hydrofoils

Two swept finite-span hydrofoils with mean root chordlength $c_r = 149$ mm, span $b = 200$ mm, and a leading edge sweep angle of 26.1°, corresponding to a semi-span aspect ratio of $AR = 2.01$, were designed and fabricated out of aluminum in the same manner as the rectangular planform models. The baseline and 4L equivalent hydrofoil (i.e., $A = 12\%$ and $\lambda = 50\%$ of the local chordlength) are shown in Figure 4. Rounded tips analogous to those used on the finite-span rectangular planform hydrofoils were implemented on these swept hydrofoils as well.
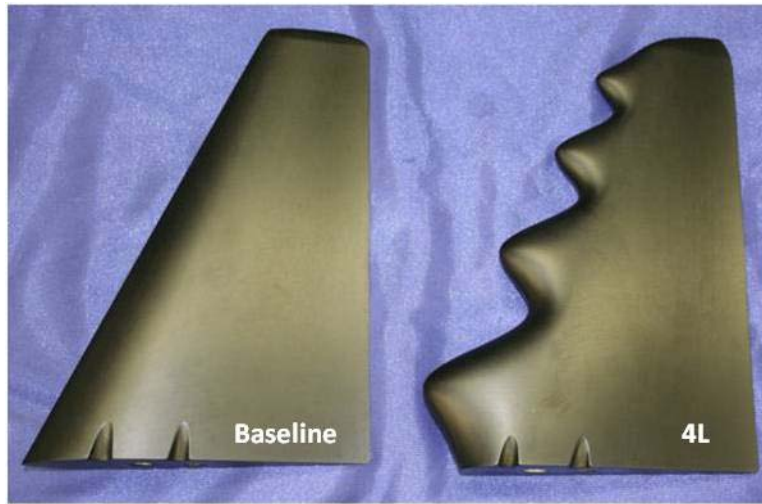

Figure 4. Swept leading edge hydrofoil models.

Flipper models

Two hydrofoil models with mean root chordlength $c_r = 62$ mm, span $b = 229$ mm, a semi-span aspect ratio $AR = 4.43$, which closely resembled the humpback whale flipper morphology, were designed and fabricated to examine the effect of protuberances on a planform found in nature, see Figure 5. The planform geometry was designed using the method outlined in Murray et al. (2005).

Figure 5. Flipper models.

Force and Moment Measurements

Load measurements were conducted on all hydrofoil models at freestream velocities ranging from $0.9 \leq U_\infty \leq 4.5$ m/s and angles of attack ranging from $-12° \leq \alpha \leq 30°$. A calibrated six-axis strain gage waterproof load cell (model AMTI MK-4741) was used to measure the forces and moments on the aforementioned hydrofoil models. The load cell was capable of measuring forces up to ±2224 N along the *x*- and *y*-axis and ±4448 N in the *z*-direction, moments of ±113 Nm about the *x*- and *y*-axis and ±56.5 Nm about the z-direction. All hydrofoils were mounted to the load cell by means of an adapter plate, which retained an axis of rotation centered about the quarter chord location $(0.25c)$ of the hydrofoils, and transferred the forces and moments on the hydrofoils directly to the load cell. The load cell was housed inside a mechanism which allowed the measurement of forces and moments at various angles of attack. The load measurement apparatus is shown in Figure 6. The measured forces and moments were converted to lift, drag, and pitching moment coefficients using the measured freestream dynamic pressure, the planform area of the hydrofoils, and the mean chordlength.
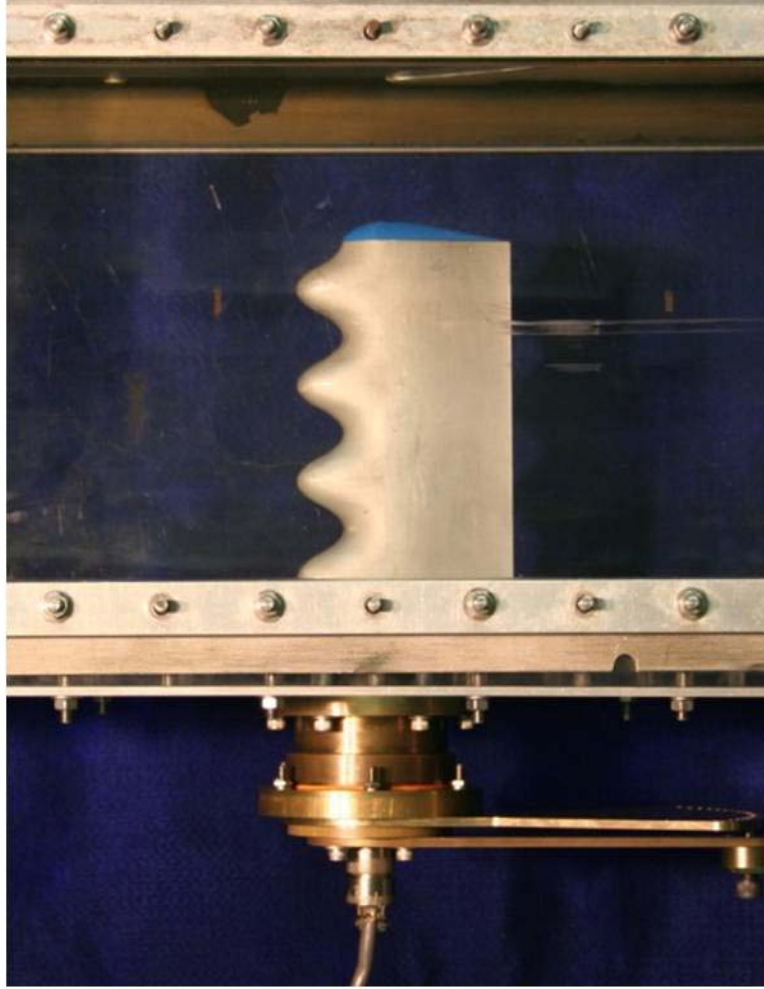
Figure 6. 4L finite-span rectangular hydrofoil in water tunnel test section with the pitch mechanism below the test section floor.

A primary objective of the experiments presented here was to determine the effect of Reynolds number on modified hydrofoils. In doing so, it was possible to expand upon past results on hydrofoils with leading edge protuberances, which due to load cell limitations, were completed at a maximum freestream velocity of $U_\infty = 1.80$ m/s, corresponding to a Reynolds number $Re_c = 1.80 \times 10^5$. To record load data at higher Reynolds numbers, the load cell discussed earlier was integrated into a customized mechanism capable of withstanding higher forces and moments. The pitch mechanism can be seen in the lower portions of Figure 6. This mechanism was capable of angle of attack adjustments ranging from $-30.0° \leq \alpha \leq 30.0°$ in increments of $1.50°$ to an accuracy of $\alpha = \pm 0.3°$.

Flow Visualization

Low-speed flow visualization experiments using dye injection was conducted on the 219-mm span baseline and 4L hydrofoils. The purpose of the experiments was to gain a qualitative understanding of the near surface flow on hydrofoils with leading edge protuberances. The experiments were carried out by injecting pressurized dye into an internal reservoir located inside the hydrofoils at the quarter chord location. A series of 1.6 mm dye ports were drilled along the leading edge of both hydrofoils that branched off from the internal dye reservoir. The ports were located at every protuberance peak, trough, and inflection point of the 4L hydrofoil, with the exception of the hydrofoil ends, while the baseline hydrofoil had ports with an equivalent spacing of 12.5 mm. A pressurized tank located outside of the water tunnel test section supplied the liquid red dye of neutral buoyancy which was injected through the dye ports. A needle valve capable of minute adjustments controlled the dye flow. A freestream velocity of $U_\infty = 0.15 \, \text{m/s}$ was used when conducting dye experiments. Very low-speed freestream velocities were necessary for a detailed examination of the flow field, particularly at high angles of attack. As the width of the NUWC water tunnel test section was larger than the hydrofoil span, fences were placed on the ends of the hydrofoil to minimize spanwise flow and prevent the formation of tip vortices.

The dye streakline patterns were captured using still image photography using a Canon DS 126071 Digital Rebel XT. The lighting consisted of a front lit gray background lit by a halogen floodlight. The reflected light created a clear contrast between the background and the hydrofoil. The digital camera used featured automatic shutter speed and aperture settings. It was necessary to use the automatic settings for shutter speed and aperture because of different reflected light intensities, depending on the angle of attack of the hydrofoil. The focus, however, was manually set at the beginning of each experiment.

Low-Speed PIV

A low-speed planar PIV experiment was carried out in the WPI water tunnel to examine the spanwise flow and streamwise vorticity on a full-span 4L hydrofoil. A freestream velocity of $U_\infty = 0.15 \, \text{m/s}$ was used, corresponding to the low-speed dye visualization experiments, and angles of attack range of $3° \leq \alpha \leq 24°$, in $3°$ increments. Seven chordwise planes were examined at each angle of attack, $-0.12, -0.06, 0, 0.06, 0.12, 0.25, 0.37 \, c$. For each case, 1000

image pairs were taken so that an accurate time averaged flow field could be acquired. The time delay over which each image pair was taken, Δt, ranged from 9 ms $\leq \Delta t \leq$ 15 ms depending on the angle of attack. The changes in Δt were necessary as local flow velocities increased with the angle of attack.

The SLA 4L hydrofoil was used for these low-speed PIV tests. An experimental apparatus was designed, which essentially hung the hydrofoil, by means of an aluminum bar spanning the test section, from the top of the water tunnel to insert the hydrofoil into the tunnel. A simple mechanism consisting of a clamped cylinder centered and attached to the hydrofoil at the quarter chord location was used to change the angle of attack. As a result, the quarter chord location was the axis of rotation. The hydrofoil ends were fenced to minimize any spanwise flow and to prevent the formation of tip vortices.

The experiments were conducted using a LaVision PIV imaging system, which consisted of a 135 mJ/pulse double pulsed Nd:YAG laser, the corresponding sheet optics, and one ImagePro2M 2-megapixel CCD camera. The orientation of the laser sheet was perpendicular to the freestream flow to acquire the cross-stream velocity vectors to enable the calculation of streamwise vorticity field. The camera used to acquire images was placed at the rear of the water tunnel looking directly upstream. A schematic of the planar, low-speed PIV setup is shown in Fig. 7.
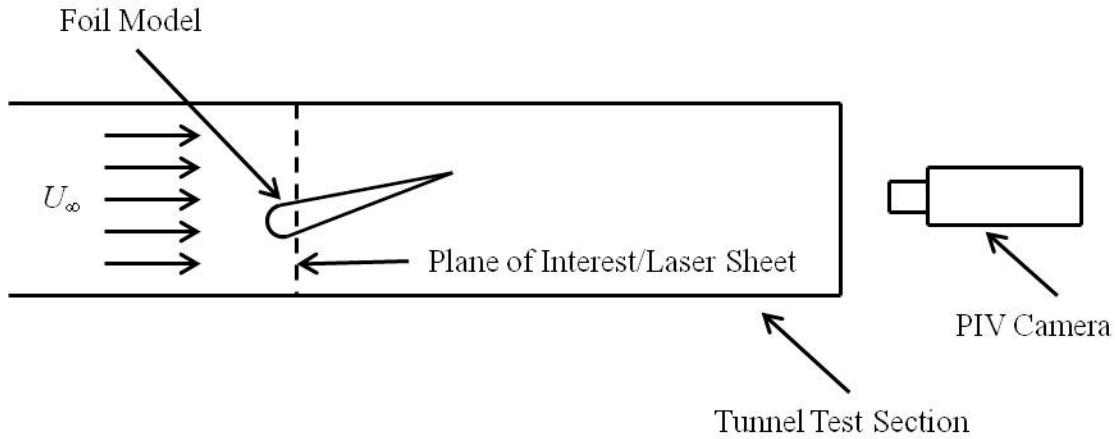

Figure 7. Schematic of low-speed PIV system at WPI.

High-Speed Stereo-PIV

Two different sets of high-speed Stereo Particle Image Velocimetry (SPIV) experiments were conducted at the NUWC water tunnel facility. An examination of the effect of Reynolds

number on the flow field of full-span hydrofoils with leading edge protuberances was conducted in one set of experiments while a study of the effect of leading edge protuberances on the spanwise flow, streamwise vorticity, and tip vortex on finite-span hydrofoils at Reynolds numbers of $Re_c = 1.8 \times 10^5$ and 4.5×10^5 was done in the second experiment. Due to physical limitations of the water tunnel test section, SPIV was necessary to determine the cross-stream velocities necessary for the calculation of the derived quantities such as vorticity.

The experiments were performed using a LaVision SPIV imaging system, which consisted of a 135 mJ/pulse double pulse Nd:YAG laser, the associated sheet optics, and two ImagerPro4M 4-megapixel CCD cameras. For all tests, the orientation of the laser sheet was perpendicular to the freestream flow (to acquire cross-stream flow field velocities). A set of 400 image pairs were taken so that a reliable time averaged dataset could be computed. Two time delay values of $\Delta t = 100$ μs and 250 μs were used at $U_\infty = 1.80$ and 4.50 m/s, respectively.

Full-span SPIV measurements

To examine the effect of Reynolds number on the flow characteristics of full-span hydrofoils, a set of high-speed SPIV experiment was conducted at the NUWC water tunnel facility. Two freestream velocities were examined, $U_\infty = 1.80$ and 4.50 m/s, along with a range of angles of attack of $6° \leq \alpha \leq 24°$ in increments of $6°$. The two hydrofoil models employed were the baseline and 4L, both having a mean chordlength of $c = 102$ mm and spanning the entire water tunnel test section. Only one chordwise plane at $0.36\,c$ was considered for direct comparison to the low-speed PIV tests conducted at WPI.

The cameras used to acquire image pairs were oriented on the same side of the water tunnel test section at 45° angles, upstream and downstream of the laser sheet. Two triangular, acrylic, water-filled prism windows were attached to the test section wall perpendicular to the respective camera. Prisms were necessary to eliminate refraction generated at the air/acrylic interface of the tunnel test section. A schematic of the high-speed full-span SPIV setup can be seen in Fig. 8.
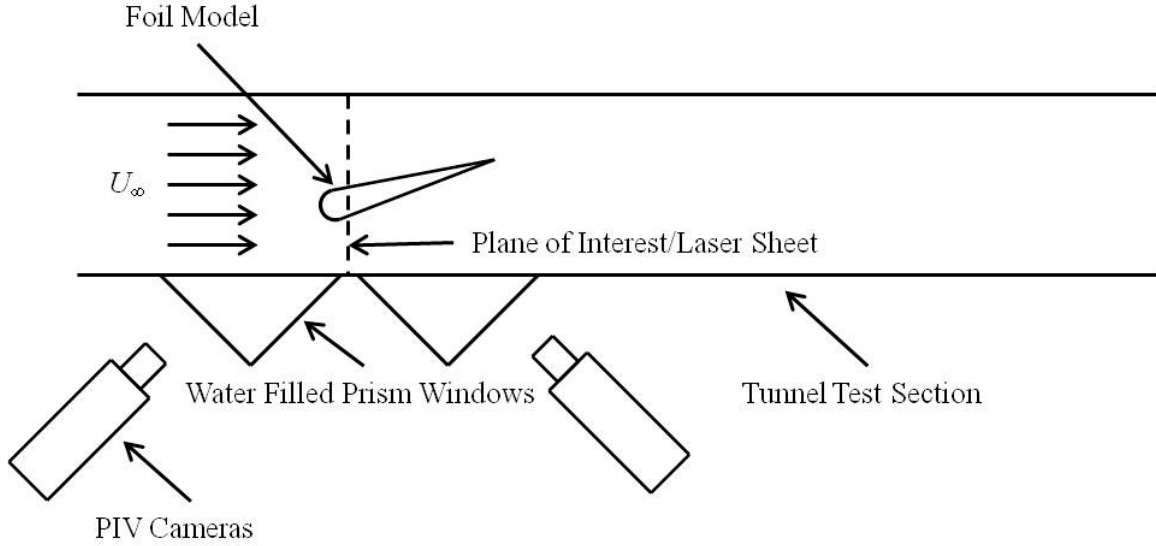
Figure 8. Schematic of full-span SPIV system at NUWC.

Finite-span SPIV measurements

The above described high-speed SPIV setup was also used to examine the effect of leading edge protuberances on the flow field of finite-span hydrofoils. Two freestream velocities were examined $U_\infty = 1.80$ and 4.50 m/s, along with a range of angles of attack of $6° \leq \alpha \leq 24°$ in increments of $6°$. Three hydrofoil models were employed, the baseline, 8M, and 4L models; all had mean chordlength of $c = 102$ mm and span $b = 219$ mm. To observe the development of the tip vortex, two planes downstream of the trailing edge were examined $1.5\ c$ and $3.0\ c$.

The camera orientation used for examination of the tip vortex consisted of two cameras downstream of the area of interest on opposite sides of the water tunnel test section placed at 45º to the freestream flow. Once again, the two triangular acrylic water-filled prism windows were used to eliminate the effects of refraction. A schematic of the high-speed finite-span SPIV setup used for the examination of the tip vortex is shown in Fig. 9.
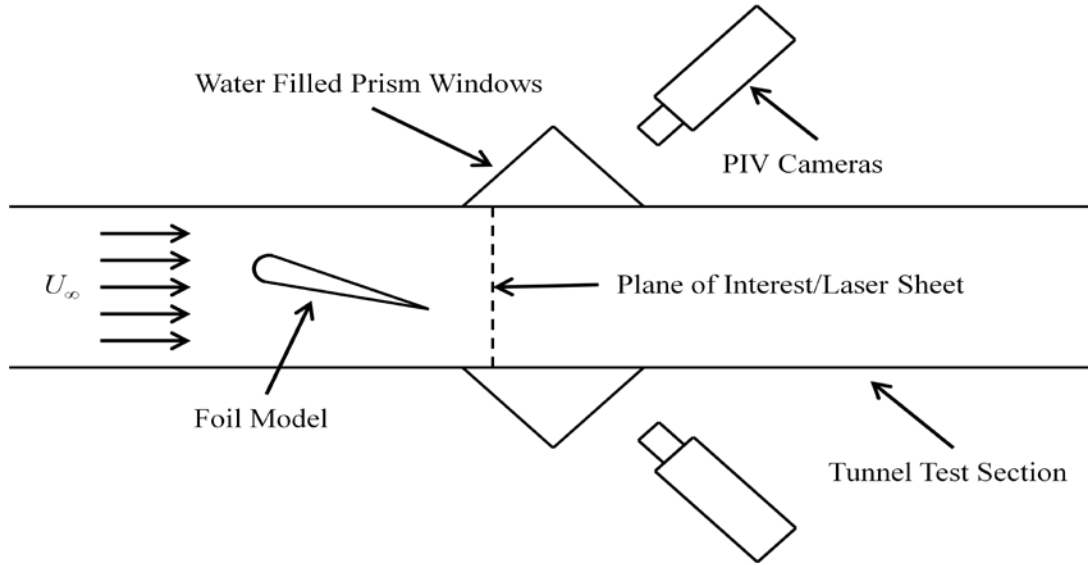
Figure 9. Schematic of finite-span SPIV system used for tip vortex study at NUWC.

Cavitation

High-speed photography

To examine the cavitation characteristics of hydrofoils with leading edge protuberances, a qualitative flow visualization study was carried out at high-speed in the NUWC water tunnel facility. The freestream velocity was held constant at $U_\infty = 7.2$ m/s for this set of tests. The angle of attack range examined was from $12° \leq \alpha \leq 24°$ in increments of $3°$. Cavitation was absent at angles of attack below $12°$ at the freestream velocity of 7.2 m/s. Images were taken with a Nikon D200 Digital SLR camera and strobe lighting to illuminate areas of cavitation. Synchronized strobe lighting with an illumination time of 200 μs was used as a single flash to illuminate both the front surface of the hydrofoils as well as the background for contrast. The photography was performed in a darkened room. The strobes were flashed once during the open shutter time effectively creating a shutter speed of 0.2 ms, which was necessary to capture the detail of cavitating flow. Images were taken on all finite-span rectangular planform hydrofoils as well as the swept planform hydrofoils.

Load measurements

Load measurements were taken on hydrofoils with and without protuberances at the 7.2 m/s freestream velocity. The procedure used was identical to that described for the lower Reynolds number tests. The freestream velocity used corresponds to a Reynolds number of $Re_c = 7.2 \times 10^5$.

Cavitation number

An examination of the effect of leading edge protuberances on the cavitation number was carried out. To determine the cavitation number of the hydrofoils it was necessary to monitor the freestream static pressure in addition to the freestream velocity. The incipient cavitation criterion was the first visual cues of presence of vaporous cavitation near the leading edge. When the incipient cavitation condition had been reached on a given hydrofoil at an angle of attack, the freestream velocity and static pressure were recorded. Subsequently, the incipient cavitation number for all hydrofoils over the range of angles of attack was determined.

Uncertainty Analysis

The uncertainties associated with the force, moment, and PIV measurements are discussed below.

Load cell bias error

The force and moment measurement uncertainties are due to the intrinsic error of the load cell output. The accuracy of the measured forces and moments were determined through an inspection of the measured values. The load cell uncertainties were extracted from unprocessed data by comparing the maximum and minimum measurements to the mean in a 100 sample dataset under steady load. The resulting uncertainties are listed in Table 2.

Table 2. Uncertainties associated with the load cell measurements at Low- and high-speeds.

	F_x (N)	F_y (N)	M_z (Nm)
$U_\infty = 1.8$ m/s	± 0.3	± 0.3	± 0.08
$U_\infty = 4.5$ m/s	± 1.78	± 1.78	± 0.05

The freestream velocity had a maximum uncertainty of $\pm 0.5\%$. The uncertainty in the angle of attack is estimated to be $\pm 0.3°$ stemming from the pitching mechanism. Due to machining errors, there are uncertainties associated with the hydrofoil dimensions. To determine the error in the hydrofoil chordlength and span, measurements were taken on the hydrofoils at several spanwise locations. The total error resulted in no more than a $\pm 0.8\%$ and $\pm 0.5\%$ difference from the expected chordlength and span values of the models, respectively.

To get a sense of the error associated with the normalized coefficients, the bias errors of these coefficients, along with those for the angle of attack and Reynolds number, were calculated and are presented in Table 3 for the full-span, baseline hydrofoil at two angles of attack in the linear regime and near stall for freestream velocities of U_∞ = 1.8 and 4.5 m/s. The methods outlined in Coleman and Steel (1989) and Wheeler and Ganji (1996) were used to determine the bias uncertainties. Except for the drag coefficient at the low angle of attack, the computed uncertainties for the force and moment coefficients are less than 5% in Table 3.

Table 3. Uncertainty values associated with force and moment measurements.

	C_L	C_D	$C_{M1/4}$	α	Re_c
U_∞ = 1.8 m/s; $\alpha = 6°$ (linear regime)	± 1.8%	± 16.5%	± 0.6%	± 5.5%	± 2.2%
U_∞ = 1.8 m/s; $\alpha = 19.5°$ (near stall)	± 1.6%	± 2.1%	± 0.2%	± 1.7%	± 2.2%
U_∞ = 4.5 m/s; $\alpha = 6°$ (linear regime)	± 1.74%	± 17.0%	± 0.5%	± 5.5%	± 2.2%
U_∞ = 4.5 m/s; $\alpha = 19.5°$ (near stall)	± 1.42%	± 4.3%	± 0.2%	± 1.7%	± 2.2%

Standard deviation of measurements

The load measurements presented here are the average values of 10 second samples. The standard deviation of the mean was calculated for the full-span, baseline hydrofoil at comparable angles and freestream velocities to the bias error analysis and is presented in Table 4. The following expression was used to calculate the standard deviation of the mean:

$$\sigma_{mean} = \frac{2}{\sqrt{N}} \sqrt{\frac{1}{N} \sum_{j=1}^{N} (x_j - \bar{x})}$$

where N is the sample size and x is the variable of interest.

Table 4. Standard deviation of the mean for the full-span baseline hydrofoil.

standard deviation of the mean	C_L	C_D	$C_{M1/4}$
$U_\infty = 1.8$ m/s; $\alpha = 6°$ (linear regime)	± 1.3%	± 11.3%	± 10.1%
$U_\infty = 1.8$ m/s; $\alpha = 19.5°$ (near stall)	± 1.3%	± 0.26%	± 1.4%
$U_\infty = 4.5$ m/s; $\alpha = 6°$ (linear regime)	± 2.2%	± 0.26%	± 0.90%
$U_\infty = 4.5$ m/s; $\alpha = 19.5°$ (near stall)	± 0.14%	± 0.20%	± 0.38%

With the exception of drag and pitching moment coefficient at the low-speed and low angle of attack case, the standard deviation of the measurements are very small as shown in Table 4 indicating that there is little fluctuation in the load measurements.

Hydrodynamic characteristic uncertainty

Several important hydrodynamic characteristics are presented in the Results section, and the maximum and minimum uncertainties associated with these parameters were calculated and are presented in Table 5. Although the measured forces and moments have uncertainties that vary on a case to case basis, the ranges shown in Table 5 represent the absolute maximum and minimum uncertainties that can be expected.

Table 5. Maximum and minimum uncertainties associated with the hydrodynamic characteristics.

hydrodynamic parameter	minimum uncertainty	maximum uncertainty
$\frac{dC_L}{d\alpha}$ [deg^{-1}]	7.0%	10.6%
C_{Lmax}	1.4%	2.0%
α @ C_{Lmax} [deg]	1.2%	2.4%
C_{Dmin}	21%	25%
L/D_{max}	3.5%	5.5%
α @ L/D_{max} [deg]	2.3%	9.8%
α_{stall} [deg]	1.3%	2.4%

PIV uncertainties

The uncertainties associated with the PIV data were also calculated based on the error associated with the resolution of pixel displacement. The pixel displacement error associated with the systems used was ± 0.1 pixels. In the areas of interest, the typical pixel displacement was measured to have a mean value between 2 and 7 pixels. The resulting uncertainty of velocity, vorticity, and circulation are presented in Table 6.

Table 6. Uncertainties associated with the PIV measurements.

	u	v	w	ω	Γ
PIV$_{2\ pixels}$	5%	5%	5%	15%	5%
PIV$_{7\ pixels}$	1.43%	1.43%	1.43%	4.3%	1.43%

Results

Force Measurements

The load characteristics of modified hydrofoils were measured as a function of angle of attack, and compared to the baseline hydrofoil. The time-averaged loads were converted into dimensionless coefficients of lift coefficient, C_L, drag coefficient, C_D, and quarter-chord pitching moment coefficient, $C_{M1/4}$, using the freestream dynamic pressure and the planform area. The effects of protuberance amplitude, wavelength, and Reynolds number were examined for each of the hydrofoils in the following sections.

Full-span Hydrofoils

An examination of the effects of protuberances on full-span hydrofoils was used to both confirm past experiments as well as to further examine the effects of Reynolds number on modified full-span hydrofoils. Two hydrofoils were examined; the 4L model along with its baseline equivalent.

Baseline hydrofoil

The baseline lift coefficient is presented in Fig. 10 as a function of angle of attack for the Reynolds number ranging from $0.9 - 4.5 \times 10^5$. The observed baseline lift coefficient is typical for the thick foil profile being examined. There is a linear increase in C_L with a lift curve slope of $\frac{dC_L}{d\alpha} \approx 0.09$ for all Reynolds numbers tested until $\alpha \approx 11°$. Past $\alpha = 11°$ the lift coefficient becomes nearly constant, which is an indication of flow separation. Flow separation can be distinguished in the drag characteristics as well, as drag increases rather quickly at higher angles of attack. This effect can be seen in Fig. 10b as the effects of separation cause C_D to increase quadratically. As the angle of attack is increased, the lift curve remains level until there is a dramatic loss of lift and increase in drag at the stall angle. The minimum C_D occurs at $\alpha \approx 0°$ with a value of $C_{Dmin} = 0.0158$ at a freestream velocity of $U_\infty = 4.5$ m/s, while the maximum occurs at the maximum angle of attack. This is the true for all Reynolds numbers examined.

At lower velocities, Reynolds number plays an important role in establishing the lift characteristics of the baseline hydrofoil. At Reynolds numbers greater than $Re_c \approx 3.6 \times 10^5$, there is no significant effect on the C_L or C_D for the baseline hydrofoil; however below this value, both an increase in maximum lift and its corresponding angle of attack along with stall angle with Reynolds number is observed.

The effect of Reynolds number on the pitching moment coefficient, see Fig. 10c, reveals that as the angle of attack is increased, $C_{M1/4}$ decreases nearly monotonically. This pattern indicates that, although the hydrodynamic center does not remain constant throughout the range of angles tested, nor is the hydrodynamic center lie on the quarter chord location. This is true for all calculated moment coefficients throughout this work. However, the small values of $C_{M1/4}$ even at high angles imply that the hydrodynamic center is near the quarter chord location at any given angle of attack. At the stall angle, $C_{M1/4}$ decreases dramatically. Little variation is seen in $C_{M1/4}$ for Reynolds numbers greater than $Re_c \approx 3.6 \times 10^5$.

The lift-to-drag ratio of the baseline hydrofoil is presented in Fig. 10d, and shows a nearly linear increase in *L/D* at low angles of attack with gradually decreasing *L/D* at higher angles. In the post-stall regime, *L/D* is nearly constant for all freestream velocities tested. Table 7 shows the key lift and drag characteristics of the full-span baseline hydrofoil.
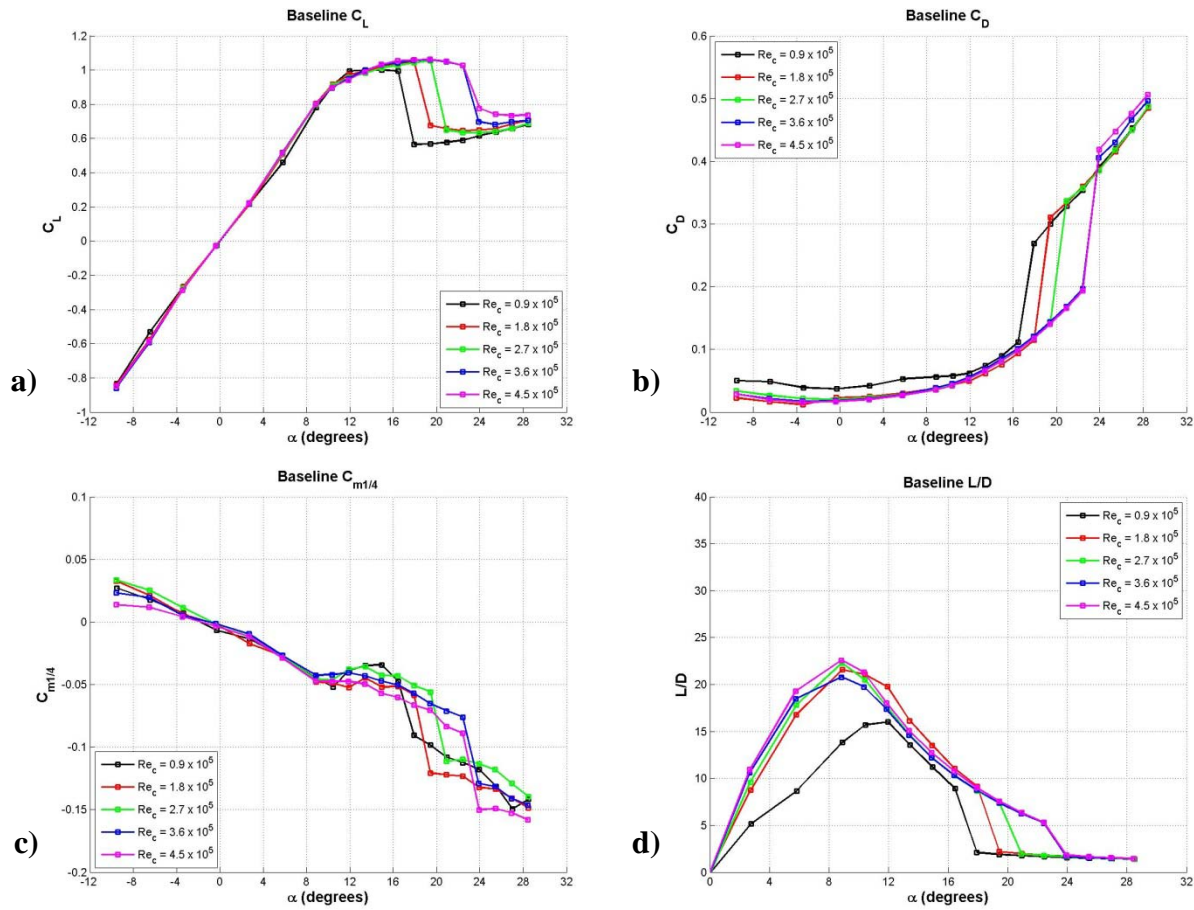
Figure 10. Full-span baseline hydrofoil load characteristics at various Reynolds numbers: a) lift coefficient, b) drag coefficient, c) pitching moment coefficient, d) *L/D* ratio.

Table 7. Hydrodynamic characteristics of full-span baseline hydrofoil. Refer to Table 5 for corresponding uncertainties.

	$Re_c = 9.0 \times 10^4$	$Re_c = 1.8 \times 10^5$	$Re_c = 2.7 \times 10^5$	$Re_c = 3.6 \times 10^5$	$Re_c = 4.5 \times 10^5$
$\frac{dC_L}{d\alpha}[\text{deg}^{-1}]$	0.079	0.079	0.081	0.083	0.084
C_{Lmax}	1.00	1.05	1.06	1.06	1.06
α @ C_{Lmax} [deg]	15.0	18.0	19.5	19.4	19.4
C_{Dmin}	0.04	0.01	0.02	0.02	0.02
L/D_{max}	16.0	21.6	22.3	20.8	22.6
α @ L/D_{max} [deg]	12.0	8.9	8.9	8.8	8.8
α_{stall} [deg]	16.5	18.9	19.5	22.4	22.4

Modified hydrofoil

The effect of Reynolds number on the full=span 4L hydrofoil is shown in Fig. 11, and the effect of protuberances on full-span hydrofoils is shown in Figs. 12 - 15. Reynolds number plays only a minor role in establishing the lift and drag characteristics of the leading edge modified hydrofoil. Maximum C_L increases with Reynolds number in the range of $0.9 \leq C_L \leq 1.01$, corresponding to Reynolds numbers of $Re_c = 9.0 \times 10^4$ and 4.5×10^5 respectively. In the linear regime, the lift curve slopes of the baseline and modified hydrofoils are similar, with values ranging from $0.078 \leq \frac{dC_L}{d\alpha} \leq 0.089$. There is little effect on the drag characteristics of modified hydrofoils over the entire range of Reynolds numbers tested. The quarter-chord pitching moment coefficient of the modified foil is shown in Fig. 11c. An overall trend of decreasing $C_{M1/4}$ is observed for all angles of attack tested. The lowest moment coefficients occur at Reynolds numbers of up to $Re_c = 1.8 \times 10^5$, while $C_{M1/4}$ at Reynolds numbers equal to or greater than 2.7×10^5 showed little difference. The lift-to-drag ratio of the modified foil, in Fig 11d reveals that L/D changes little at Reynolds numbers equal to or greater than $Re_c = 2.7 \times 10^5$ while low Reynolds number effects causing L/D to vary at lower Reynolds numbers.

The lift coefficient of the modified hydrofoil is compared with the baseline in Fig. 12. Figure 12Similar to the baseline hydrofoil, there is a linear increase in C_L with angle of attack until $\alpha \approx 6°$. As α is increased past the linear regime, the lift increases at a much lower rate, and remaining nearly constant up to the highest angles of attack examined. This leveling off of C_L is an indication of separation. At angles of attack past the linear regime, the trend in the lift

coefficient of modified hydrofoils deviates significantly from the baseline hydrofoil. In the pre-stall regime of the baseline hydrofoil, C_L is always less for any given Reynolds number. However, in the post-stall regime of the baseline, C_L of the modified hydrofoil remains nearly constant; generating 31% – 49% more lift than the baseline hydrofoil.

The drag coefficient of the modified hydrofoil is compared with the baseline in Fig. 13. Drag of the modified hydrofoil is nearly equal to that of the baseline hydrofoil at both very low angles of attack, $0° \leq \alpha \leq 6°$ and in the post-stall regime of the baseline hydrofoil. However, in the pre-stall regime of the baseline hydrofoil, C_D of the modified hydrofoil is greater than the baseline by as much as $\approx 150\%$. Although the drag of the modified hydrofoil can be significantly higher than that of the baseline in the pre-stall regime, there is no drag penalty in the post-stall regime. This indicates that in the post-stall regime of the baseline hydrofoil, as much as 50% more lift can be generated than the baseline hydrofoil with little or no drag penalty. The same trend was observed in past work by Johari et al. (2007) and Custodio (2007).

The quarter-chord pitching moment coefficient of the full-span modified hydrofoil is compared to the baseline in Fig. 14. With the exception of the two highest freestream velocities tested, $C_{M1/4}$ is generally very similar to or less than the baseline case for all positive angles of attack. At mid-range angles, $C_{M1/4}$ of the modified case can be significantly different than the baseline case. However, at post-stall angles, $C_{M1/4}$ of the modified case can be slightly greater than the baseline the highest freestream velocities.

The lift-to-drag ratio of the full-span cases are compared in Fig. 15. With the exception of Reynolds numbers below 1.8×10^5 and over a limited range of angles, in which low Reynolds number plays a significant role in establishing the performance characteristics of the foils, *L/D* of the modified foil is generally less than or nearly equal to the baseline case. This implies that although the lift coefficient of the modified case can be significantly greater than the baseline at post-stall angles, the high drag values seen in all cases in turn render any increase in *L/D* nearly negligible. Table 8 shows several important hydrodynamic characteristics of the full-span modified hydrofoil at all Reynolds numbers tested.
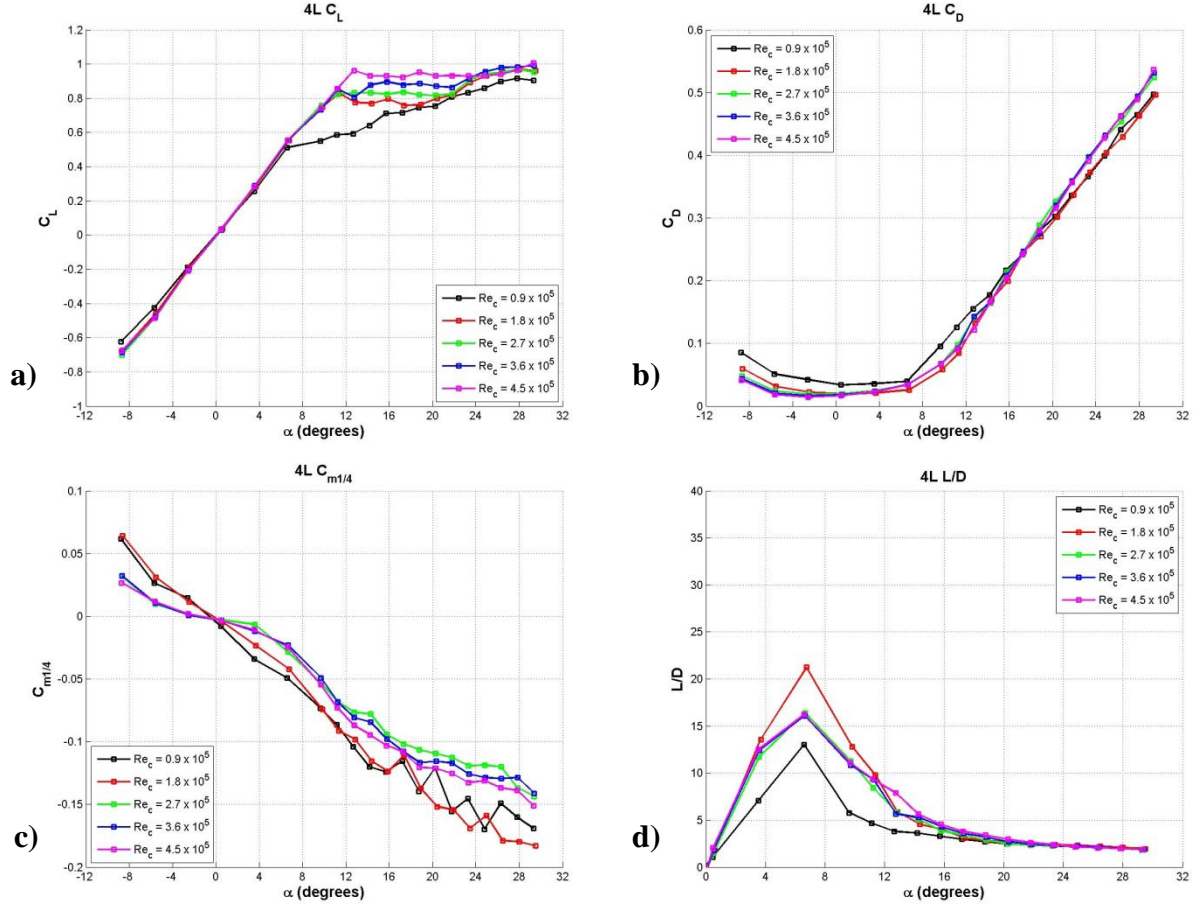
Figure 11. Full-span 4L hydrofoil load characteristics at various Reynolds numbers: a) lift coefficient, b) drag coefficient, c) pitching moment coefficient, d) *L/D* ratio.

Table 8. Hydrodynamic characteristics of full-span 4L hydrofoil.

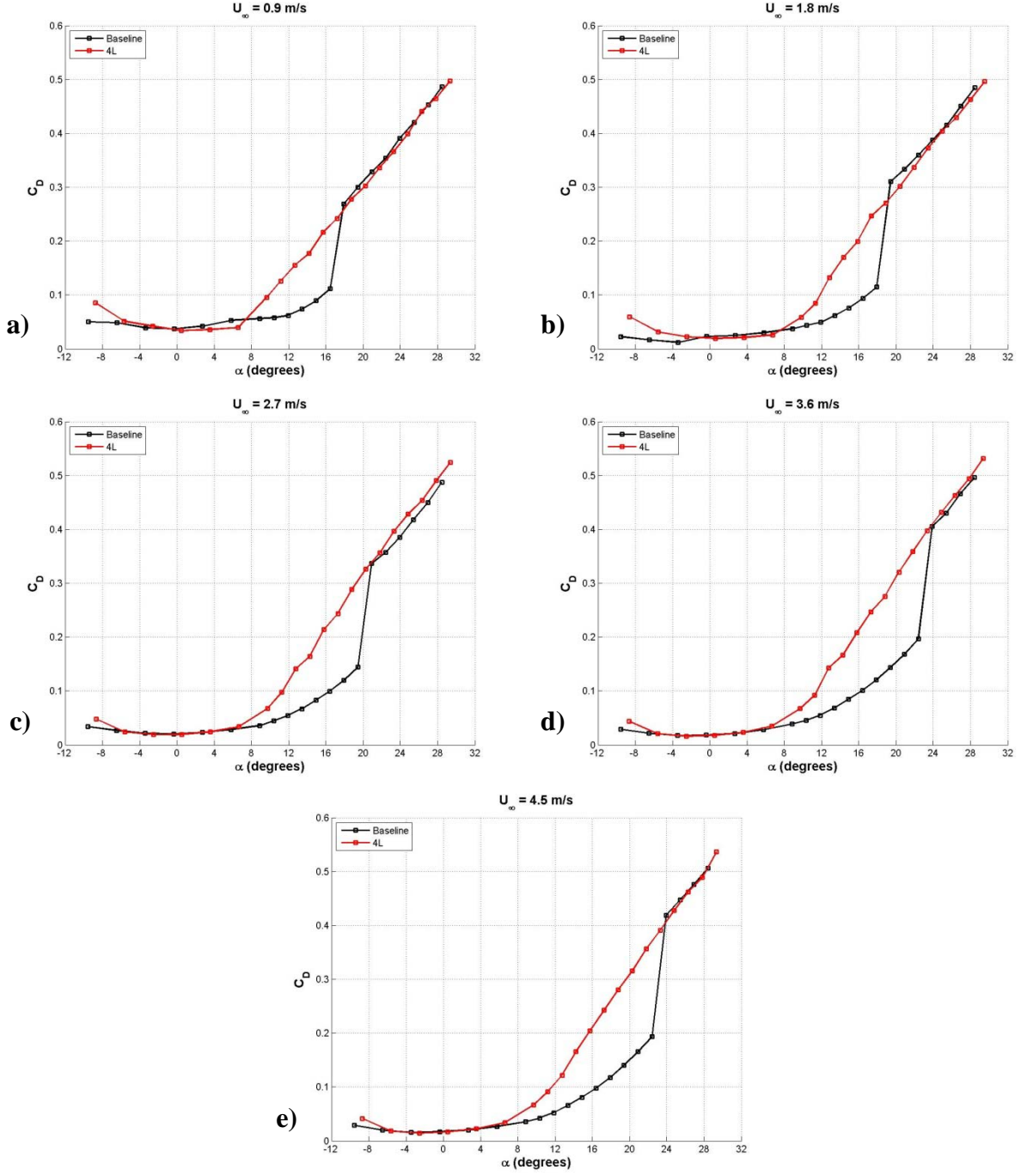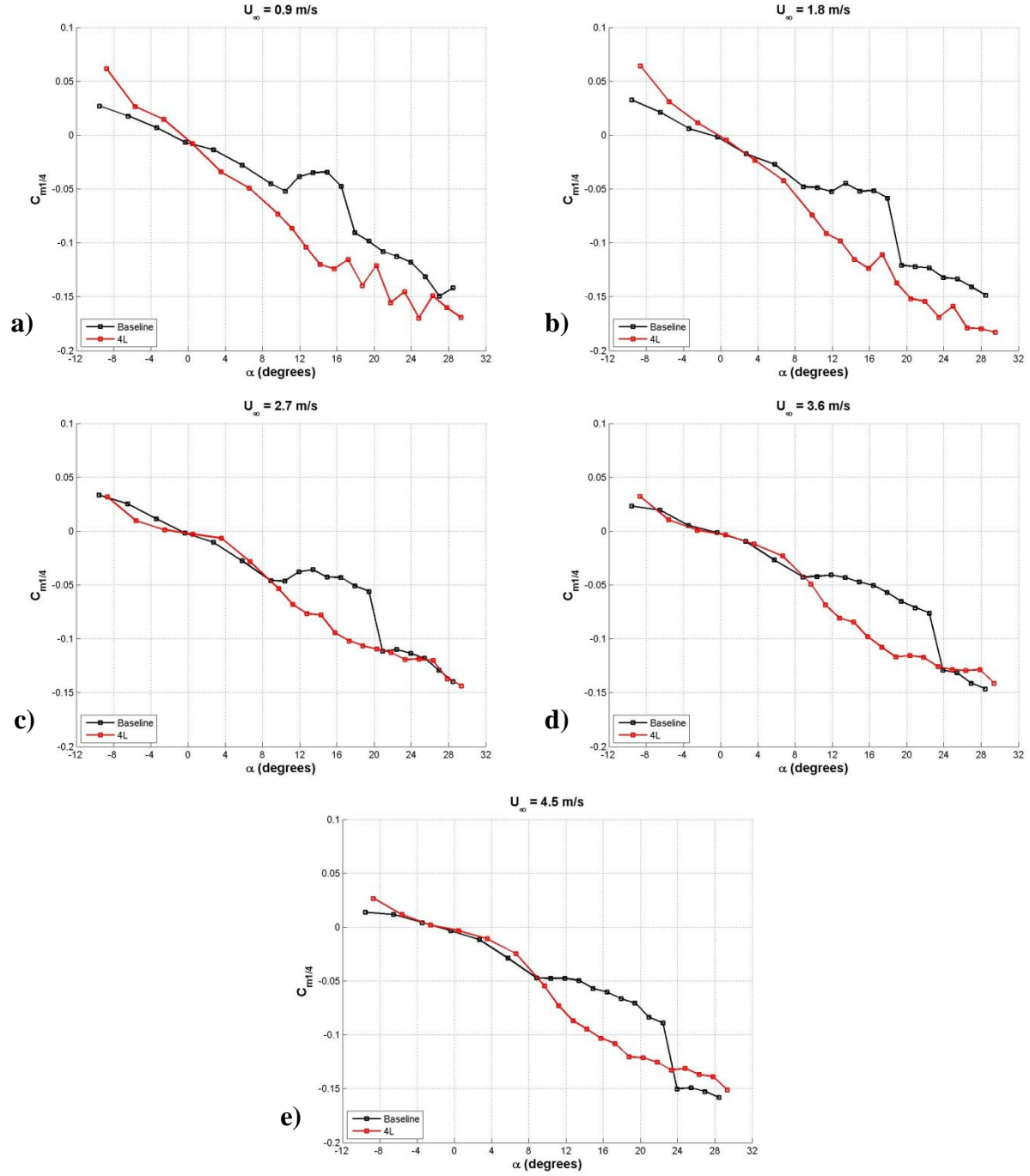|	$Re_c = 9.0 \times 10^4$	$Re_c = 1.8 \times 10^5$	$Re_c = 2.7 \times 10^5$	$Re_c = 3.6 \times 10^5$	$Re_c = 4.5 \times 10^5$
$\dfrac{dC_L}{d\alpha}$	0.072	0.077	0.080	0.081	0.080
C_{Lmax}	0.92	0.97	0.97	0.99	1.01
α @ C_{Lmax}	27.8°	28.0°	27.9°	29.4°	29.4°
C_{Dmin}	0.03	0.02	0.02	0.02	0.01
L/D_{max}	13.02	21.25	16.41	16.10	16.25
α @ L/D_{max}	6.6°	6.8°	6.7°	6.7°	6.6°
α_{stall}	N/A	N/A	N/A	N/A	N/A
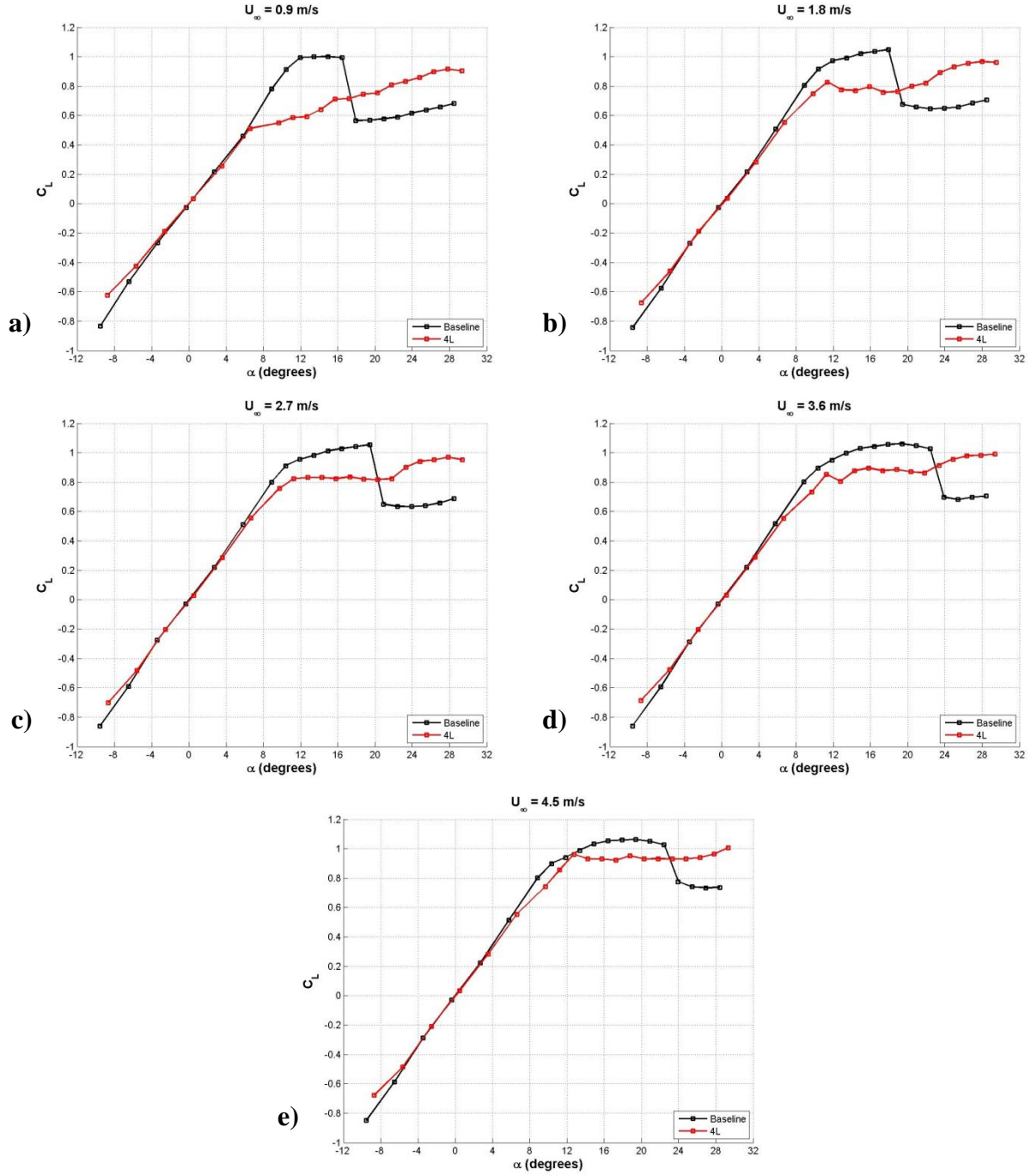
Figure 12. Lift coefficient of full-span models: a) $Re_c = 9.0 \times 10^4$, b) $Re_c = 1.8 \times 10^5$, c) $Re_c = 2.7 \times 10^5$, d) $Re_c = 3.6 \times 10^5$, e) $Re_c = 4.5 \times 10^5$.
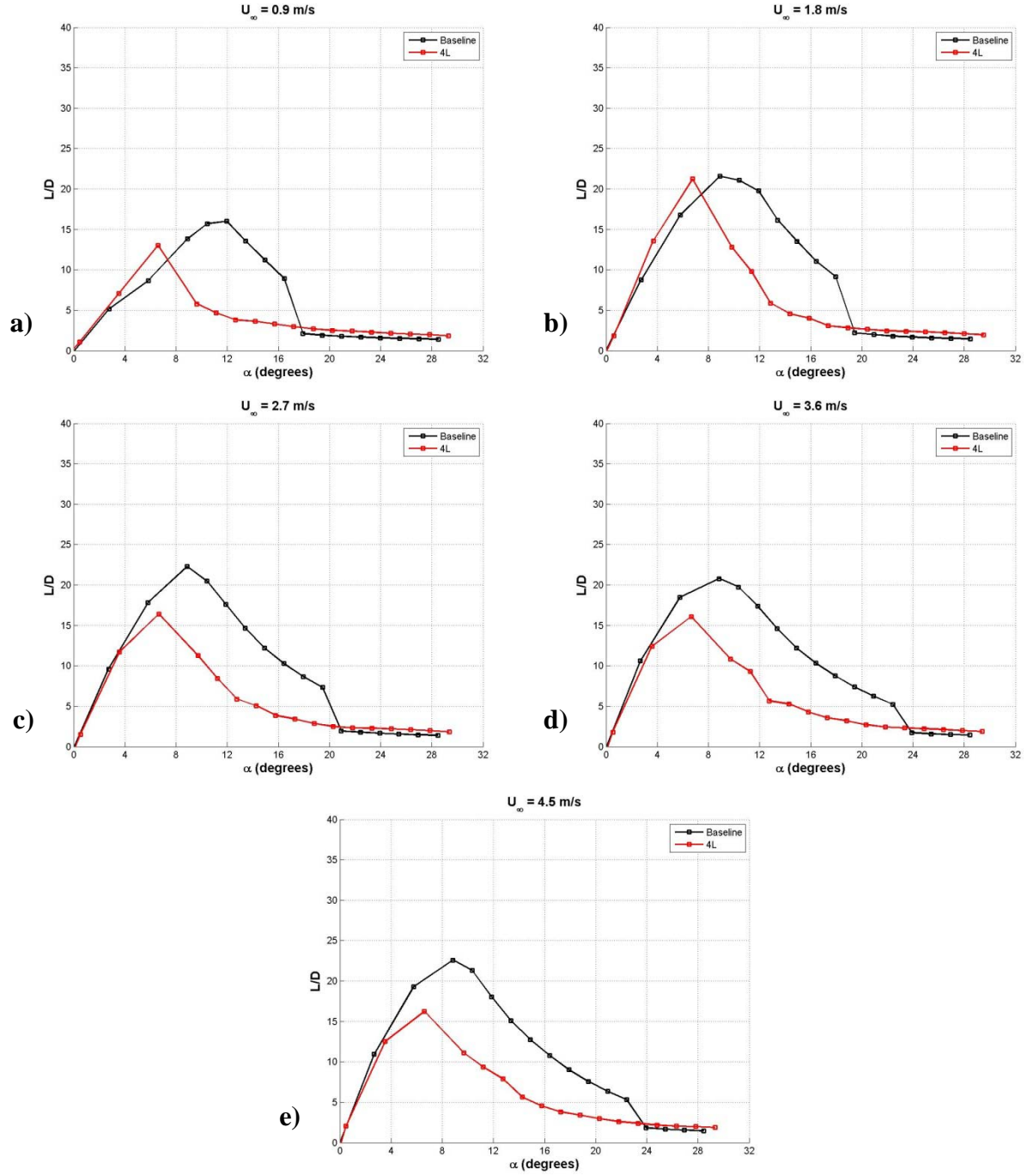
Figure 13. Drag coefficient of full-span models: a) $Re_c = 9.0 \times 10^4$, b) $Re_c = 1.8 \times 10^5$, c) $Re_c = 2.7 \times 10^5$, d) $Re_c = 3.6 \times 10^5$, e) $Re_c = 4.5 \times 10^5$.

Figure 14. Pitching moment coefficient of full-span models: a) $Re_c = 9.0 \times 10^4$, b) $Re_c = 1.8 \times 10^5$, c) $Re_c = 2.7 \times 10^5$, d) $Re_c = 3.6 \times 10^5$, e) $Re_c = 4.5 \times 10^5$.

Figure 15. Lift-to-drag ratio of full-span models: a) $Re_c = 9.0 \times 10^4$, b) $Re_c = 1.8 \times 10^5$, c) $Re_c = 2.7 \times 10^5$, d) $Re_c = 3.6 \times 10^5$, e) $Re_c = 4.5 \times 10^5$.

Finite-Span Rectangular Planform Hydrofoils

The lift, drag, and pitching moment characteristics of finite-span rectangular planform hydrofoils with different leading edge protuberance amplitudes and wavelengths are discussed in this section. Seven hydrofoils were examined: a baseline hydrofoil along with 4S, 4M, 4L, 8S, 8M, and 8L hydrofoils with a constant semi-span aspect ratio of $AR = 2.15$.

Baseline hydrofoil

Reynolds number has a major effect on the lift and drag characteristics of the finite-span baseline hydrofoil at lower speeds. The stall angle and lift coefficient at post-stall angles increase significantly with Reynolds number. As Reynolds number is increased, the effect of stall is softened, becoming less abrupt. The effect of Reynolds number on the baseline hydrofoil diminishes with increasing Reynolds number and nearly disappears at values greater than $Re_c \approx 2.7 \times 10^5$. The maximum C_L is relatively unaffected by Reynolds number.

The lift coefficient of the baseline hydrofoil in Fig. 16a reveals comparable trends to the full-span baseline case, i.e. a linear increase in C_L with α over the range of $0 \leq \alpha \leq 15°$. Past 15°, C_L levels off until the stall angle is reached, at which point lift decreases dramatically and is never recovered. In general, high Reynolds number affects the sharp loss in lift by 'softening' the stall characteristics. At the highest Reynolds number tested, $Re_c = 4.5 \times 10^5$, there is a gentle decrease in C_L at the stall angle.

The drag characteristics of the finite-span baseline hydrofoil in Fig 16b also show trends similar to the full-span baseline model. There is a quadratic increase in C_D with angle of attack at lower α, $0 \leq \alpha \leq 15°$, with the minimum drag at 0°. As Reynolds number increases to 3.6×10^5, the minimum drag coefficient decreases; however at higher Reynolds number, there is little change in the minimum drag coefficient. At the stall angle of attack, C_D increases dramatically and continues to increase over the range of angles examined.

The quarter-chord pitching moment coefficient of the baseline hydrofoil in Fig. 16c reveals that there is an increase in $C_{M1/4}$ over a wide range of angles. With the onset of separation and stall effects, $C_{M1/4}$ gradually decreases over the remaining angles tested. At Reynolds numbers greater than 3.6×10^5, there is little change in $C_{M1/4}$ over the entire range of angles tested.

The lift-to-drag ratio of the baseline hydrofoil in Fig. 16d shows that the maximum L/D increases with Reynolds number. Over the range of angles $14° \leq \alpha \leq 20°$, L/D for all Reynolds numbers tested is nearly the same while at Reynolds numbers greater than 3.6×10^5 there is little

difference in *L/D* at any angle of attack. Table 9 presents several important hydrodynamic characteristics of the finite-span baseline hydrofoil.
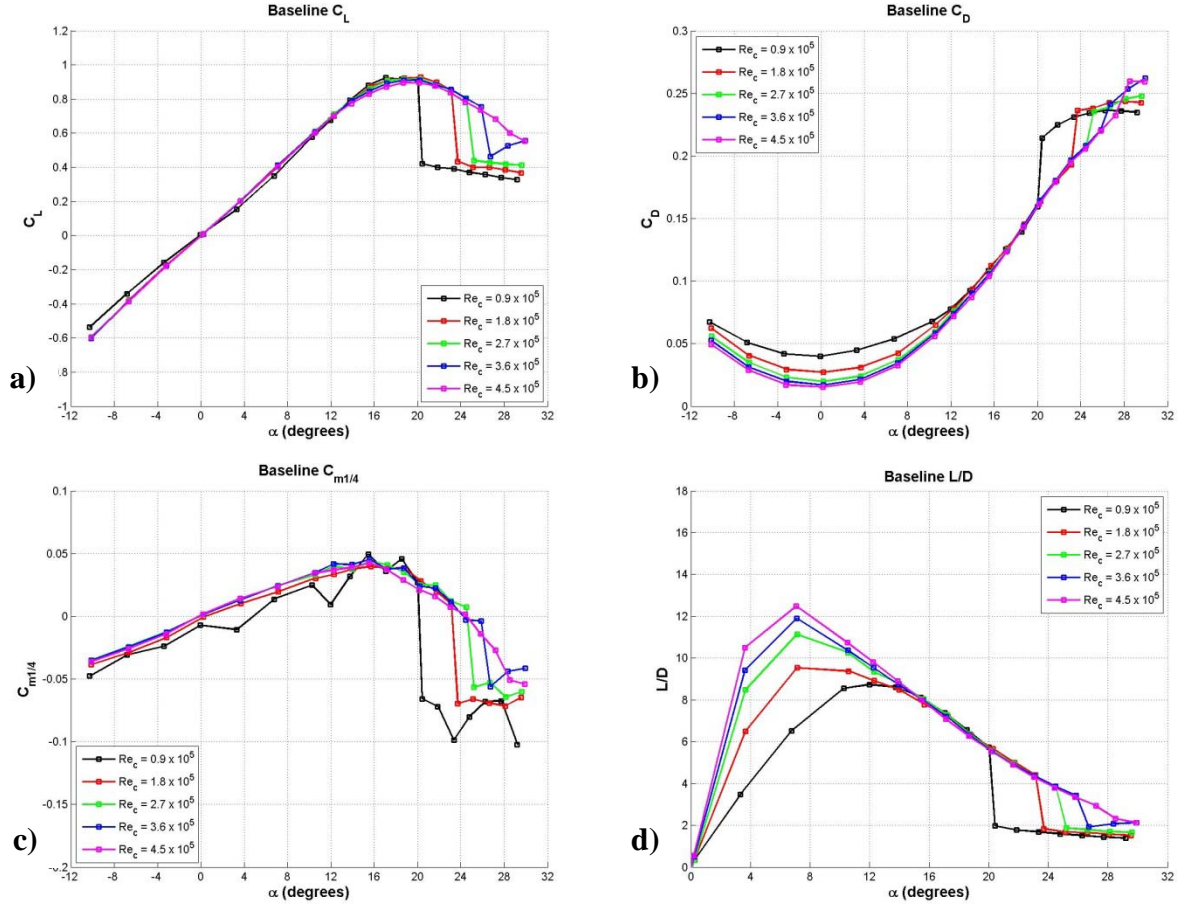

Figure 16. Effect of Reynolds number on the finite-span rectangular planform baseline hydrofoil load characteristics: a) lift coefficient, b) drag coefficient, c) moment coefficient, d) *L/D* ratio.

Table 9. Hydrodynamic characteristics of finite-span rectangular planform baseline hydrofoil.

	$Re_c = 9.0 \times 10^4$	$Re_c = 1.8 \times 10^5$	$Re_c = 2.7 \times 10^5$	$Re_c = 3.6 \times 10^5$	$Re_c = 4.5 \times 10^5$
$\frac{dC_L}{d\alpha}$ [deg^{-1}]	0.047	0.055	0.056	0.055	0.056
C_{Lmax}	0.93	0.93	0.92	0.91	0.90
α @ C_{Lmax} [deg]	17.1	20.3	20.3	20.2	18.7
C_{Dmin}	0.04	0.03	0.02	0.02	0.02
L/D_{max}	8.7	9.5	11.1	11.9	12.5
α @ L/D_{max} [deg]	12.0	7.1	7.1	7.1	7.1
α_{stall} [deg]	20.0	23.1	24.5	25.9	N/A

Modified hydrofoil

Effect of Reynolds number

The effect of Reynolds number on the load characteristics of finite-span rectangular modified hydrofoils is shown in Figs. 17 - 20. Up to $Re_c \approx 3.6 \times 10^5$ and with the exception of the pre-stall regime, all hydrofoils examined show a minor dependence on Reynolds number. As the Reynolds number increases, the maximum lift increases along with the stall angle. For any given hydrofoil, this trend remains the same. However, at the Reynolds number of $Re_c \approx 3.6 \times 10^5$ and higher, there is relatively little change in the lift characteristics of the hydrofoils. This implies that as the Reynolds number is increased past this point, there will be little adjustment in the lift characteristics of modified hydrofoils. Reynolds number affects the minimum drag coefficient, reducing it notably with increasing Reynolds number. Reynolds number clearly changes the stall effects in C_D; however at post-stall angles of attack, the drag characteristics of modified hydrofoils are unaffected by the Reynolds number. A similar trend is observed in the quarter-chord pitching moment coefficient and lift-to-drag ratios for all hydrofoils tested; Reynolds number has little effect on $C_{M1/4}$ and *L/D* except at very low Reynolds number. Also, low Reynolds number effects tend to dominate most significantly on hydrofoils with smaller amplitude protuberances. Table 10 - Table 15 show several important hydrodynamic characteristics of the modified finite-span hydrofoils.

Table 10. Hydrodynamic characteristics of finite-span rectangular planform 4S foil.

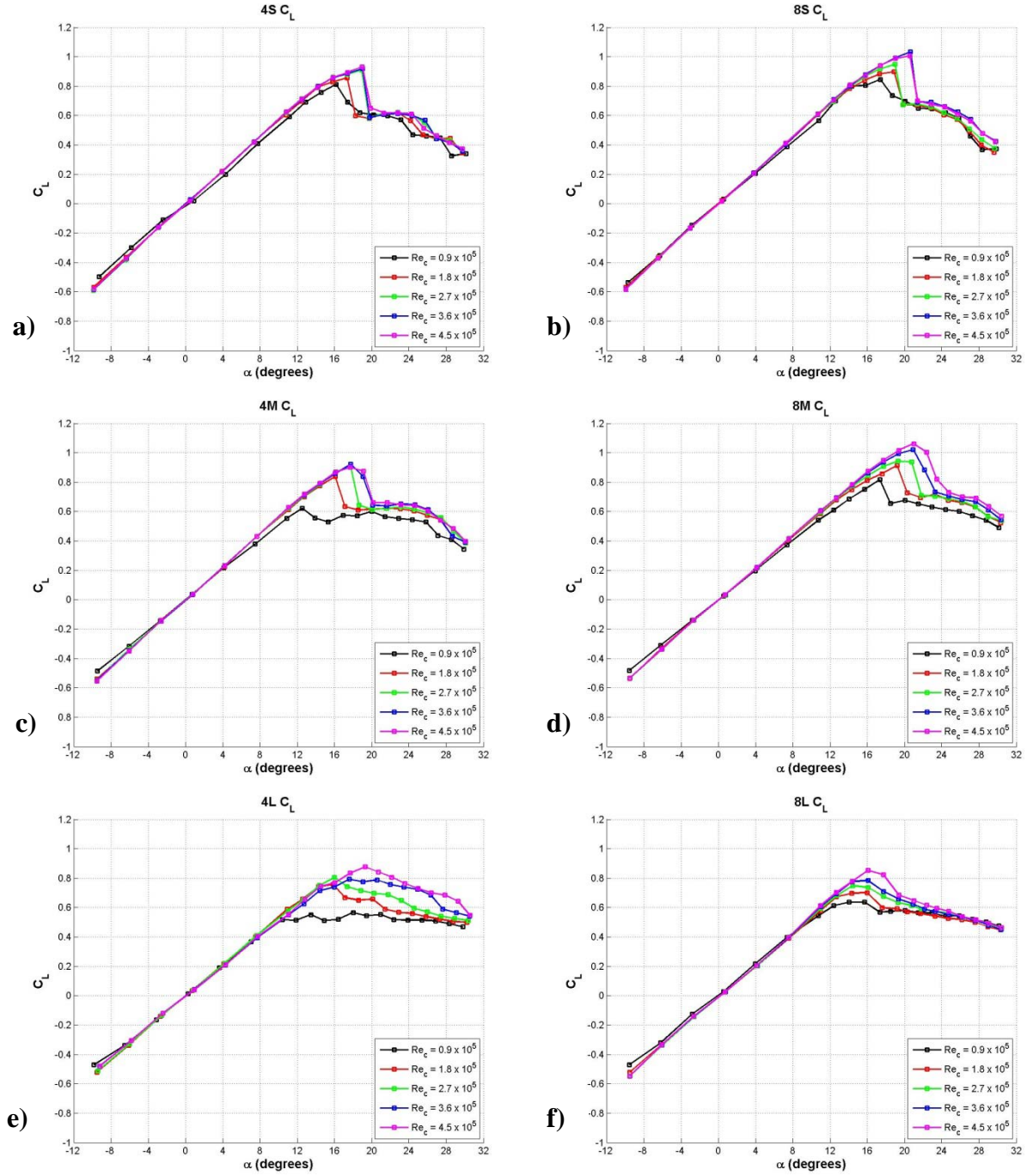|	$Re_c = 9.0 \times 10^4$	$Re_c = 1.8 \times 10^5$	$Re_c = 2.7 \times 10^5$	$Re_c = 3.6 \times 10^5$	$Re_c = 4.5 \times 10^5$
$\frac{dC_L}{d\alpha}$ [deg^{-1}]	0.046	0.056	0.055	0.055	0.055
C_{Lmax}	0.81	0.86	0.91	0.92	0.93
α @ C_{Lmax} [deg]	16.2	17.3	18.9	19.0	19.0
C_{Dmin}	0.04	0.03	0.02	0.02	0.02
L/D_{max}	6.6	9.5	10.3	11.9	11.0
α @ L/D_{max} [deg]	14.6	10.8	7.3	7.4	7.4
α_{stall} [deg]	16.2	17.3	18.9	19.0	19.0

Figure 17. Effect of Reynolds number on the lift coefficient of finite-span rectangular planform
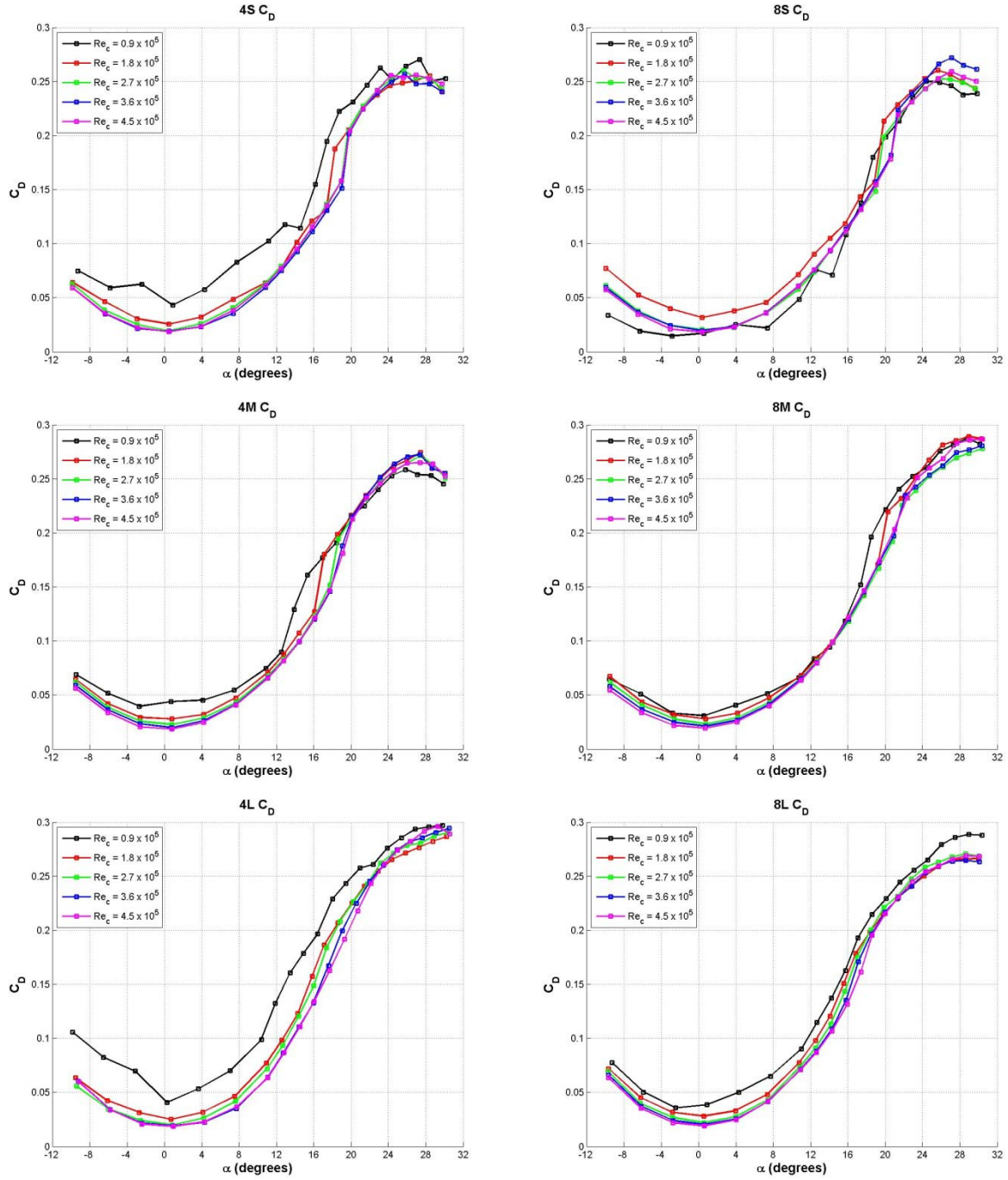modified hydrofoils: a) 4S, b) 8S, c) 4M, d) 8M, e) 4L, f) 8L.

Figure 18. Effect of Reynolds number on the drag coefficient of finite-span rectangular planform modified hydrofoils: a) 4S, b) 8S, c) 4M, d) 8M, e) 4L, f) 8L.
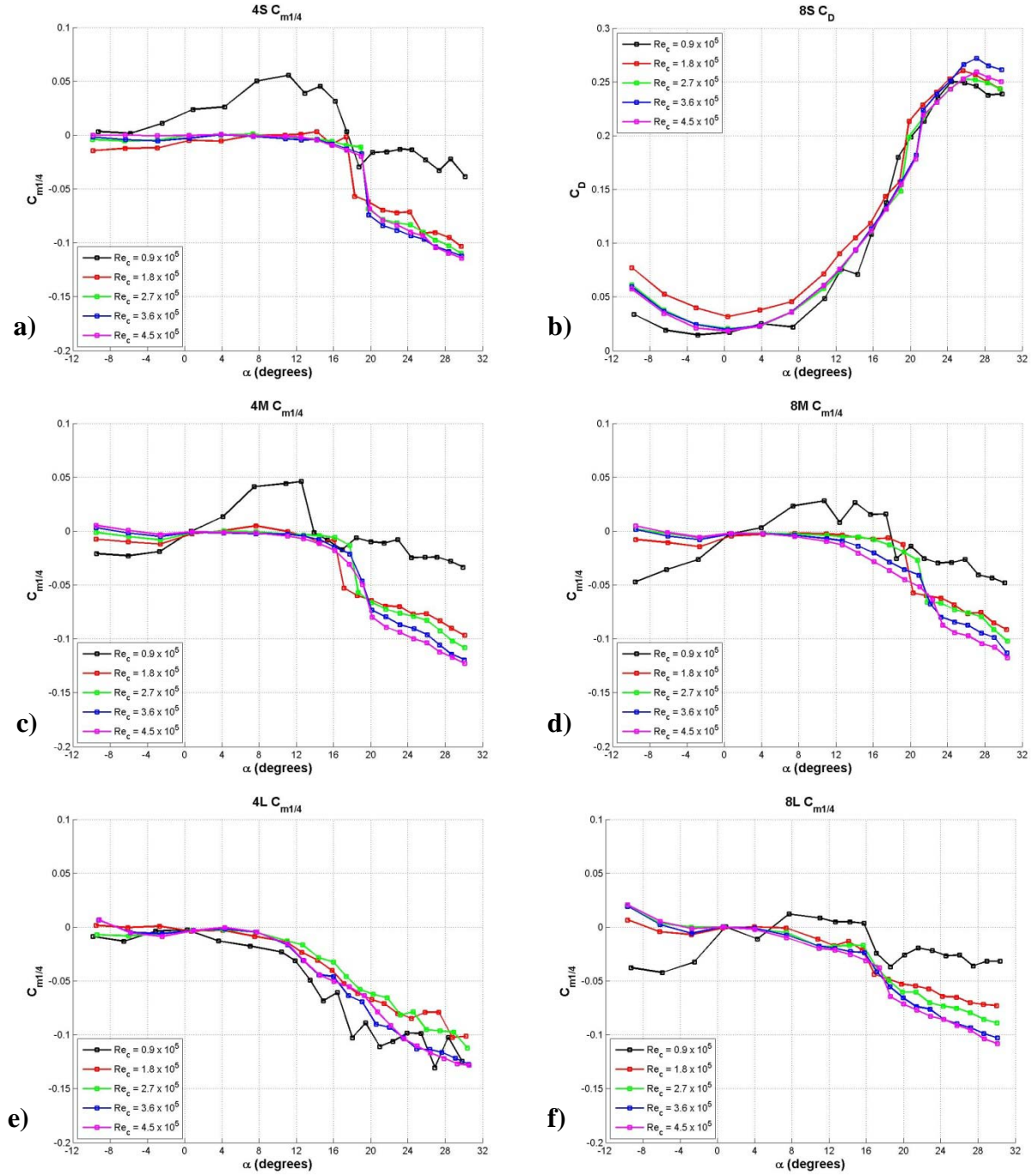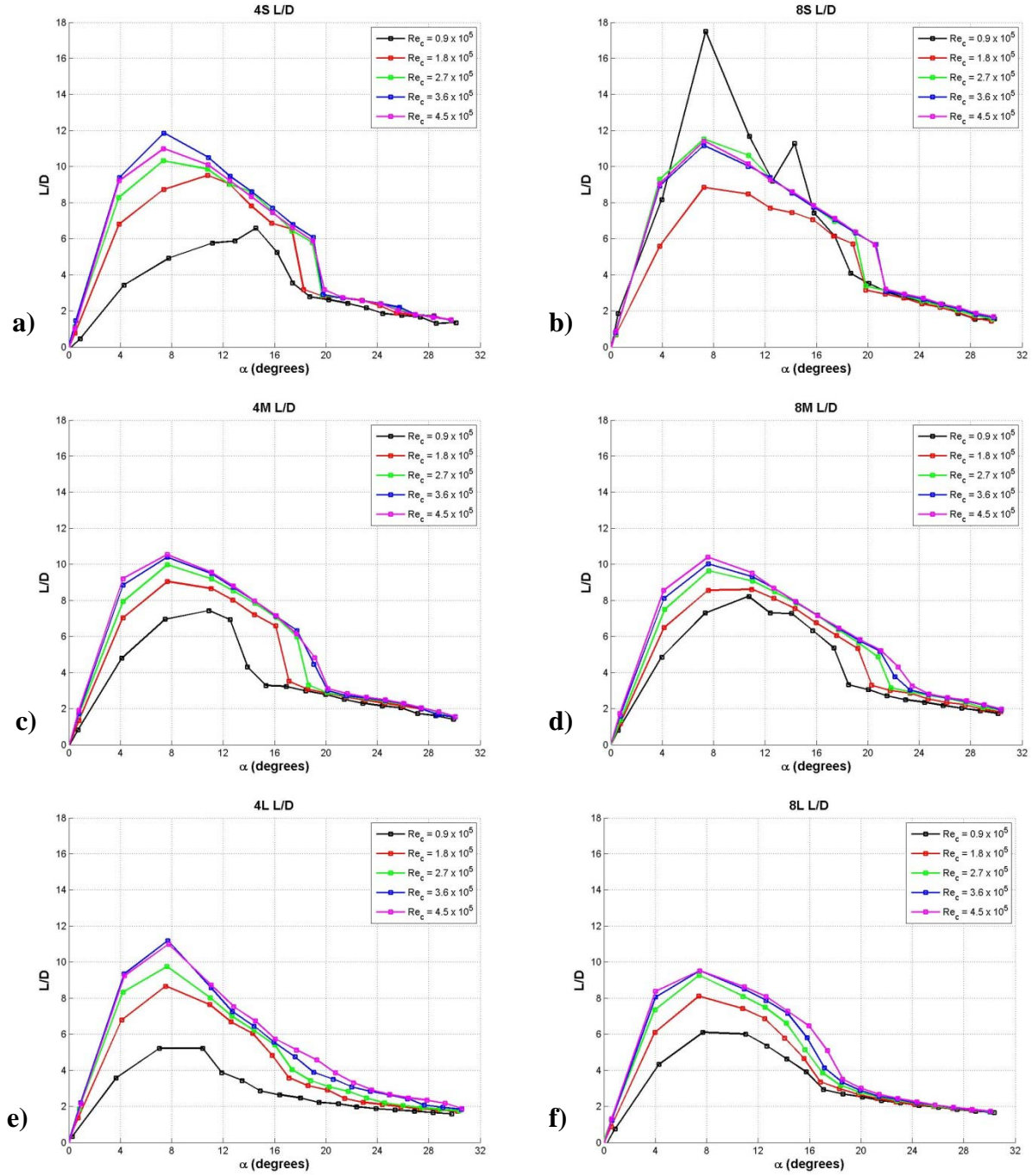
Figure 19. Effect of Reynolds number on the pitching moment coefficient of finite-span rectangular planform modified hydrofoils: a) 4S, b) 8S, c) 4M, d) 8M, e) 4L, f) 8L.

Figure 20. Effect of Reynolds number on the lift-to-drag ratio of finite-span rectangular planform modified hydrofoils: a) 4S, b) 8S, c) 4M, d) 8M, e) 4L, f) 8L.

Table 11. Hydrodynamic characteristics of finite-span rectangular planform 4M foil.

	$Re_c = 9.0 \times 10^4$	$Re_c = 1.8 \times 10^5$	$Re_c = 2.7 \times 10^5$	$Re_c = 3.6 \times 10^5$	$Re_c = 4.5 \times 10^5$
$\frac{dC_L}{d\alpha}$[deg$^-$1]	0.053	0.054	0.055	0.055	0.054
C_{Lmax}	0.62	0.84	0.91	0.92	0.90
α @ C_{Lmax} [deg]	12.5	16.1	17.7	17.7	17.7
C_{Dmin}	0.04	0.03	0.02	0.02	0.02
L/D_{max}	7.44	9.05	9.98	10.4	10.6
α @ L/D_{max} [deg]	10.9	7.66	7.7	7.7	7.7
α_{stall} [deg]	20.0	16.1	17.7	17.7	17.7

Table 12: Hydrodynamic characteristics of finite-span rectangular planform 4L foil.

	$Re_c = 9.0 \times 10^4$	$Re_c = 1.8 \times 10^5$	$Re_c = 2.7 \times 10^5$	$Re_c = 3.6 \times 10^5$	$Re_c = 4.5 \times 10^5$
$\frac{dC_L}{d\alpha}$[deg$^-$1]	0.052	0.052	0.052	0.049	0.049
C_{Lmax}	0.57	0.76	0.80	0.79	0.88
α @ C_{Lmax} [deg]	18.0	15.8	16.0	17.6	19.3
C_{Dmin}	0.04	0.03	0.02	0.02	0.02
L/D_{max}	5.2	8.7	9.8	11.2	11.0
α @ L/D_{max} [deg]	10.40	7.53	7.6	7.7	7.8
α_{stall} [deg]	N/A	N/A	N/A	N/A	N/A

Table 13: Hydrodynamic characteristics of finite-span rectangular planform 8S foil.

	$Re_c = 9.0 \times 10^4$	$Re_c = 1.8 \times 10^5$	$Re_c = 2.7 \times 10^5$	$Re_c = 3.6 \times 10^5$	$Re_c = 4.5 \times 10^5$
$\frac{dC_L}{d\alpha}$[deg$^-$1]	0.052	0.056	0.055	0.055	0.054
C_{Lmax}	0.85	0.90	0.95	1.03	1.01
α @ C_{Lmax} [deg]	17.4	18.9	19.0	20.6	20.6
C_{Dmin}	0.02	0.03	0.02	0.02	0.02
L/D_{max}	17.5	8.9	11.5	11.2	11.4
α @ L/D_{max} [deg]	7.4	7.2	7.3	7.2	7.3
α_{stall} [deg]	17.4	18.9	19.0	20.6	20.6

Table 14: Hydrodynamic characteristics of finite-span rectangular planform 8M foil.

	$Re_c = 9.0 \times 10^4$	$Re_c = 1.8 \times 10^5$	$Re_c = 2.7 \times 10^5$	$Re_c = 3.6 \times 10^5$	$Re_c = 4.5 \times 10^5$
$\frac{dC_L}{d\alpha}[\deg^{-}1]$	0.050	0.052	0.052	0.053	0.053
C_{Lmax}	0.82	0.91	0.95	1.02	1.06
α @ C_{Lmax} [deg]	17.4	19.2	19.3	20.9	21.0
C_{Dmin}	0.03	0.03	0.02	0.02	0.02
L/D_{max}	8.2	8.6	9.7	10.0	10.4
α @ L/D_{max} [deg]	10.7	11.0	7.63	7.6	7.6
α_{stall} [deg]	17.4	19.2	20.8	20.9	22.1

Table 15: Hydrodynamic characteristics of finite-span rectangular planform 8L foil.

	$Re_c = 9.0 \times 10^4$	$Re_c = 1.8 \times 10^5$	$Re_c = 2.7 \times 10^5$	$Re_c = 3.6 \times 10^5$	$Re_c = 4.5 \times 10^5$
$\frac{dC_L}{d\alpha}[\deg^{-}1]$	0.051	0.051	0.051	0.051	0.051
C_{Lmax}	0.64	0.70	0.75	0.79	0.85
α @ C_{Lmax} [deg]	14.2	15.6	14.2	15.8	15.95
C_{Dmin}	0.04	0.03	0.02	0.02	0.02
L/D_{max}	6.1	8.1	9.3	9.5	9.5
α @ L/D_{max} [deg]	7.7	7.4	7.4	7.4	7.4
α_{stall} [deg]	N/A	N/A	N/A	N/A	17.4

Effect of protuberance amplitude

The effect of protuberance amplitude on the load characteristics of modified, finite-span hydrofoils is presented in Figs. 21 – 28 for the two different wavelengths.

Longer wavelength λ = 0.50c

The effect of leading edge protuberance amplitude on the lift coefficient of modified hydrofoils with a wavelength $λ = 0.50c$ is presented in Fig. 21. In the linear regime up to $α = 9°$, hydrofoils have lift curve slopes that range from $0.056 \leq \frac{dC_L}{dα} \leq 0.068$, with a slight dependence on Reynolds number. Past 9° however, there were nontrivial variations with Reynolds number. At the lower freestream velocities within the range of $0.9 \leq U_\infty \leq 2.7$ m/s, the trends in lift coefficient are generally the same. At angles of attack past the linear regime, all hydrofoils showed indications of separation, with the lift coefficient becoming nearly constant with angle of attack. In the pre-stall regime, the maximum lift coefficient was either very close to or less than the baseline for all modified hydrofoils with a wavelength of $0.50c$. As the protuberance amplitude decreases, the maximum lift coefficient increases. Also, in the pre-stall regime, the 4S and 4M hydrofoils showed signs of stall while the 4L showed no signs of sudden stall throughout the range of angles of attack tested. All modified hydrofoils produced more lift in the early post-stall regime of the baseline hydrofoil, producing as much as 50% more lift than the baseline hydrofoil. However, at the highest angles of attack examined, the 4S and 4M performed equivalently to the baseline whereas the 4L hydrofoil continued to generate nearly 40% more lift than the baseline hydrofoil for the lowest freestream velocity tested.

At freestream velocities of $U_\infty = 3.6$ and 4.5 m/s, the lift characteristics of the 4S and 4M hydrofoils are nearly identical (to within experimental uncertainty), with lift coefficients that are very close to the baseline up to the stall angle, at which point the 4S and 4M hydrofoils had lower lift. However, the lift of the 4L hydrofoil was very similar to that of the baseline at the highest freestream velocities tested, with no dramatic stall and a maximum lift coefficient that is essentially the same as the baseline.

The drag of hydrofoils with a protuberance wavelength of $λ = 0.50c$ in Fig. 22 showed little dependence on Reynolds number. C_D for all hydrofoils was similar at a range of angles of attack $0 \leq α \leq 9°$, with the rate of increase of drag past $α = 9°$ becoming greater with protuberance amplitude. In the pre-stall regime, all modified hydrofoils have higher drag than the baseline

hydrofoil. As the protuberance amplitude increases, the drag in the pre-stall regime increases as well. In the post-stall regime of the baseline hydrofoil, the drag of all modified hydrofoils was either equal to (to within experimental uncertainty) or greater than the baseline hydrofoil.

The pitching moment coefficient about the quarter-chord point is shown in Fig. 23. For all positive angles of attack tested, $C_{M1/4}$ for the modified hydrofoils is significantly less than the baseline. With the exception of the lowest freestream velocity tested, in which low Reynolds number effects dominate, $C_{M1/4}$ at mid-range angles decreases with amplitude and remain similar for all other angles tested. Whereas there are clear signs of stall on hydrofoils with protuberance amplitudes of $A = 0.025c$ and $0.05c$, with dramatic drops in moment at high angles, the 4L model, which has the largest protuberances, $A = 0.12c$, showed little sign of a dramatic stall.

The lift-to-drag ratios, shown in Fig. 24, reveal that hydrofoils with protuberances have L/D values either less than or nearly equal to the baseline model. In general, at pre-stall angles of attack, hydrofoils with smaller protuberances outperform the hydrofoil with the largest protuberance amplitude. All hydrofoils perform similarly at post-stall angles of attack.
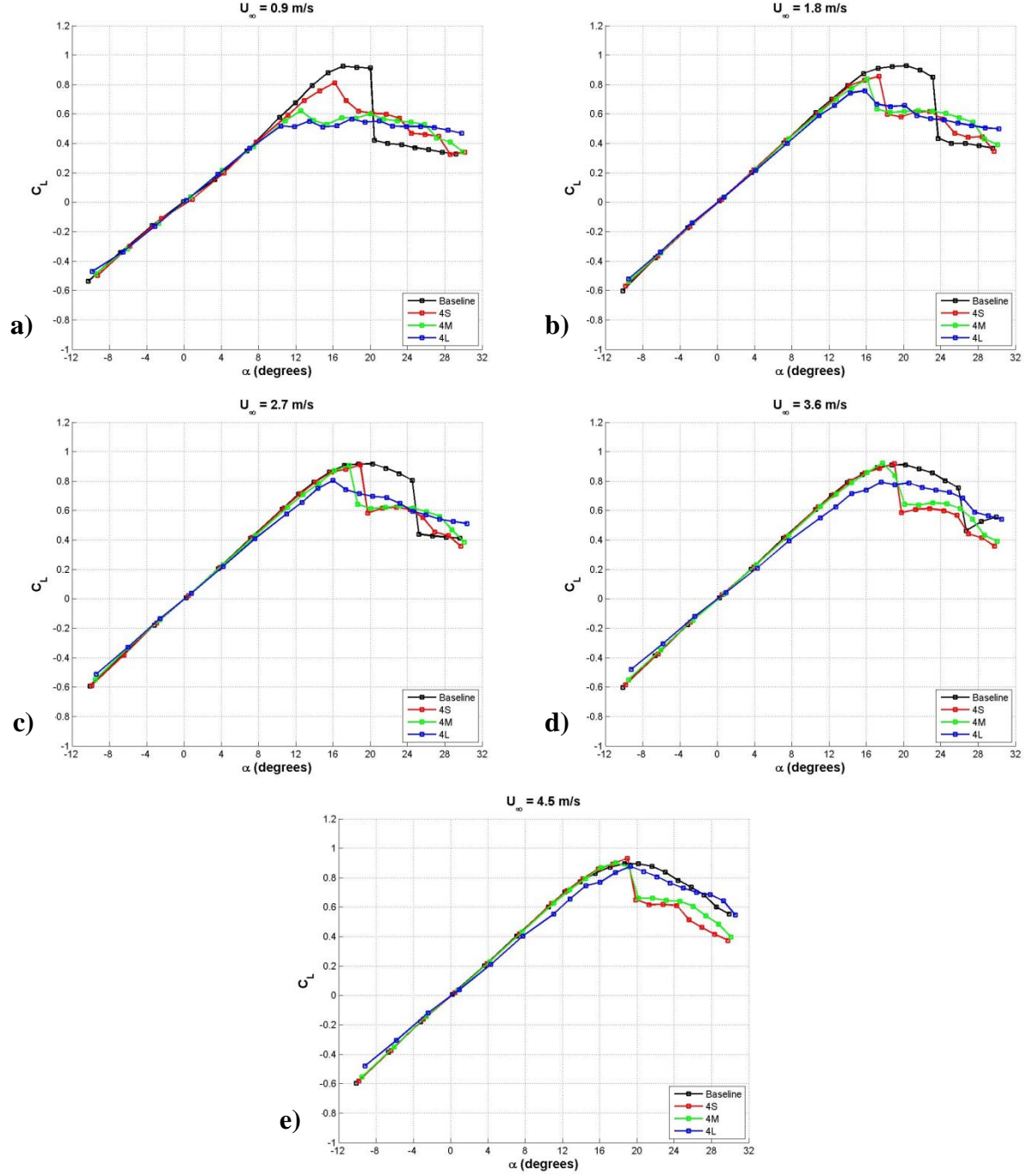
Figure 21. Effect of protuberance amplitude on the lift coefficient of finite-span rectangular planform hydrofoils, $\lambda = 0.50c$. a) $Re_c = 9.0 \times 10^4$, b) $Re_c = 1.8 \times 10^5$, c) $Re_c = 2.7 \times 10^5$, d) $Re_c = 3.6 \times 10^5$, e) $Re_c = 4.5 \times 10^5$.
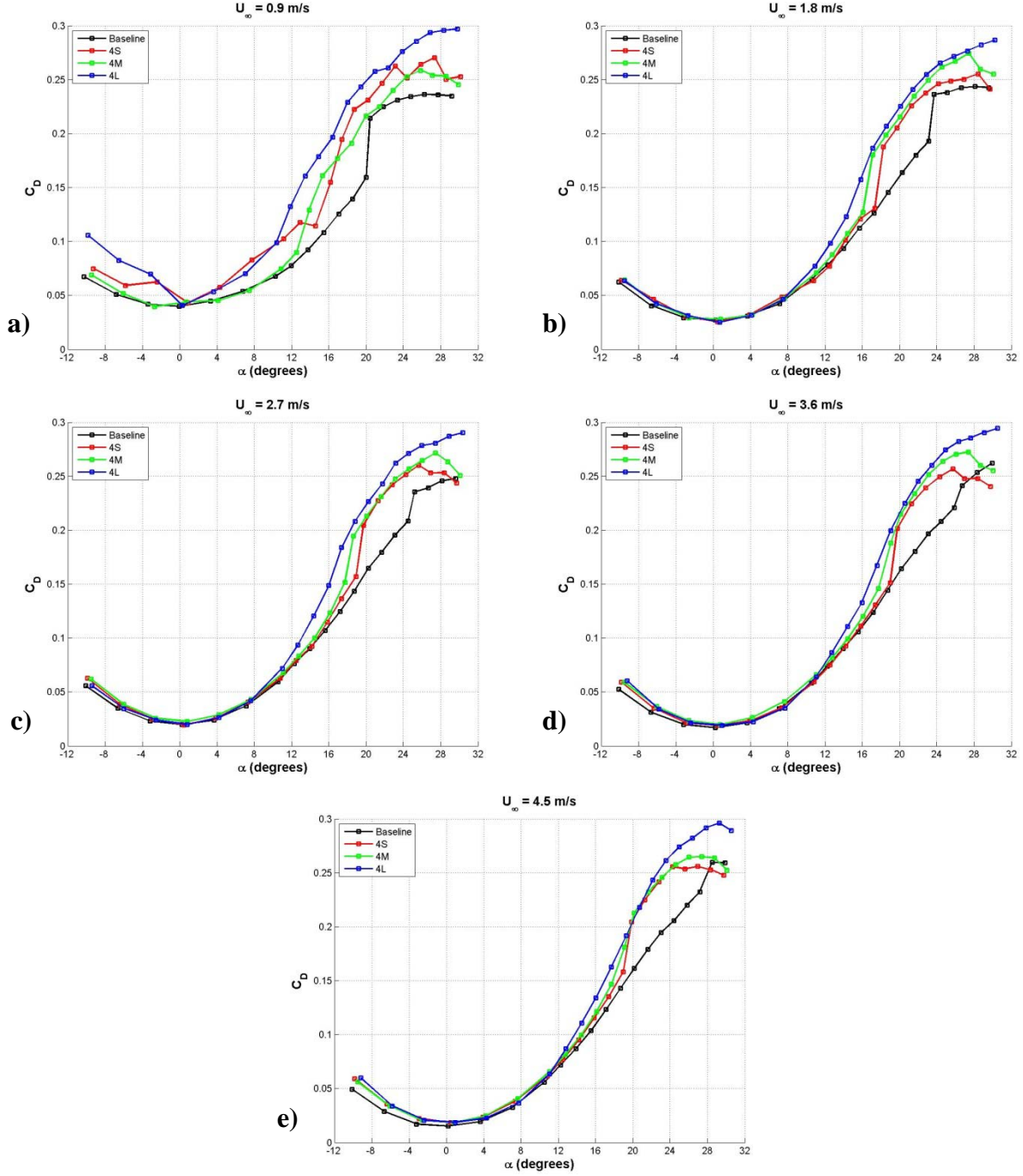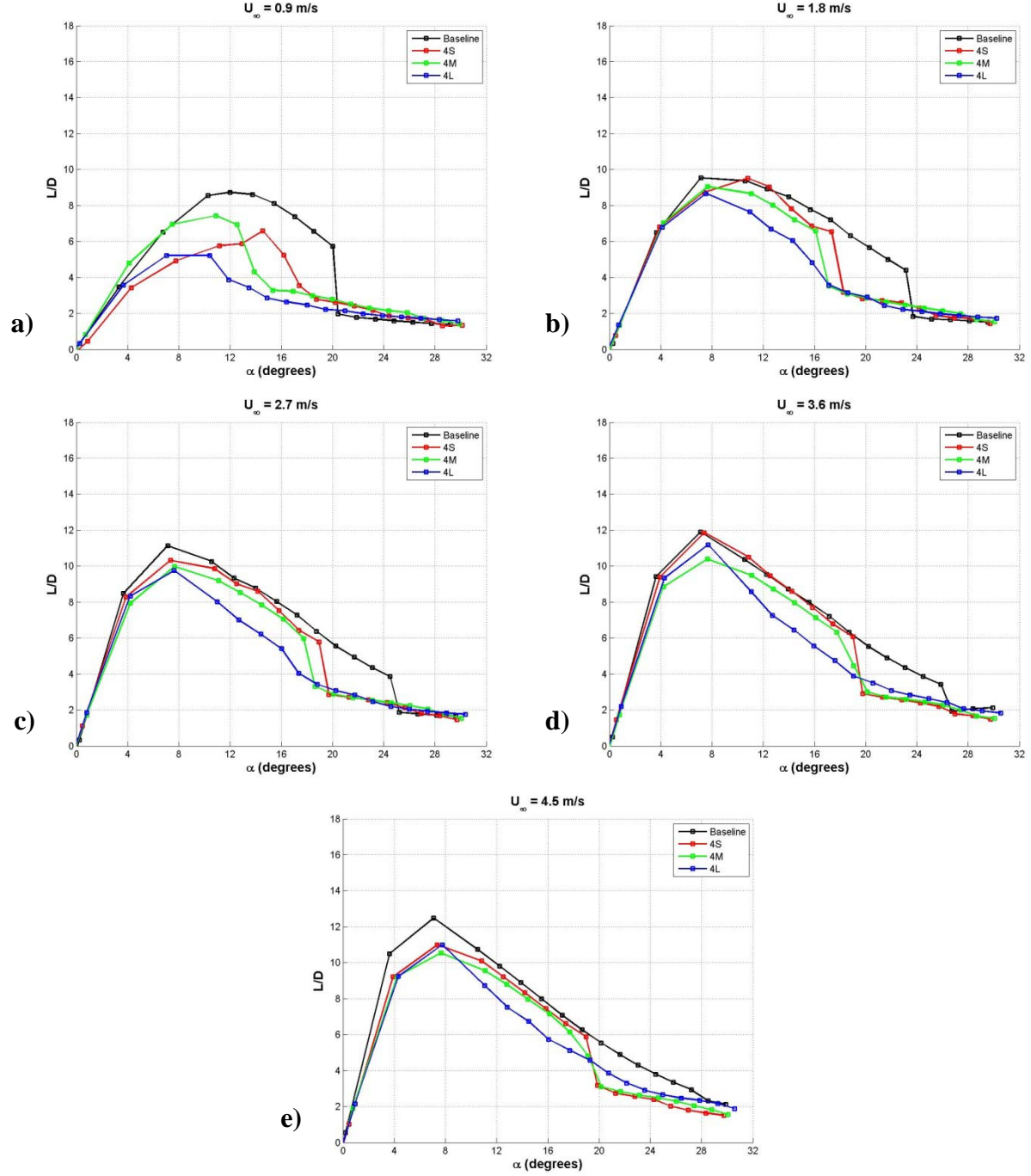
Figure 22. Effect of protuberance amplitude on the drag coefficient of finite-span rectangular planform hydrofoils, $\lambda = 0.50c$. a) $Re_c = 9.0 \times 10^4$, b) $Re_c = 1.8 \times 10^5$, c) $Re_c = 2.7 \times 10^5$, d) $Re_c = 3.6 \times 10^5$, e) $Re_c = 4.5 \times 10^5$.
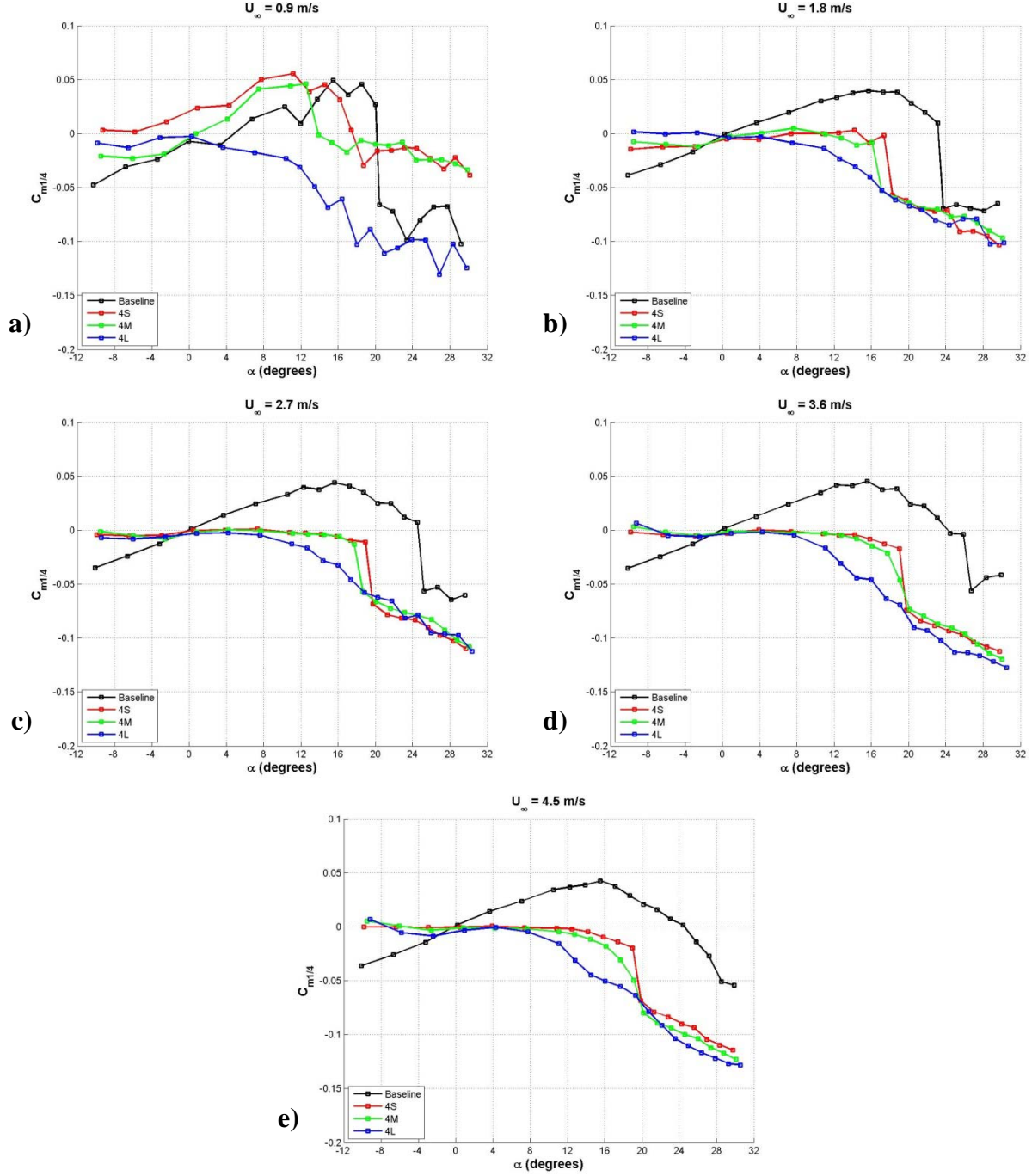
Figure 23. Effect of protuberance amplitude on the pitching moment coefficient of finite-span rectangular planform hydrofoils, $\lambda = 0.50c$. a) $Re_c = 9.0 \times 10^4$, b) $Re_c = 1.8 \times 10^5$, c) $Re_c = 2.7 \times 10^5$, d) $Re_c = 3.6 \times 10^5$, e) $Re_c = 4.5 \times 10^5$.
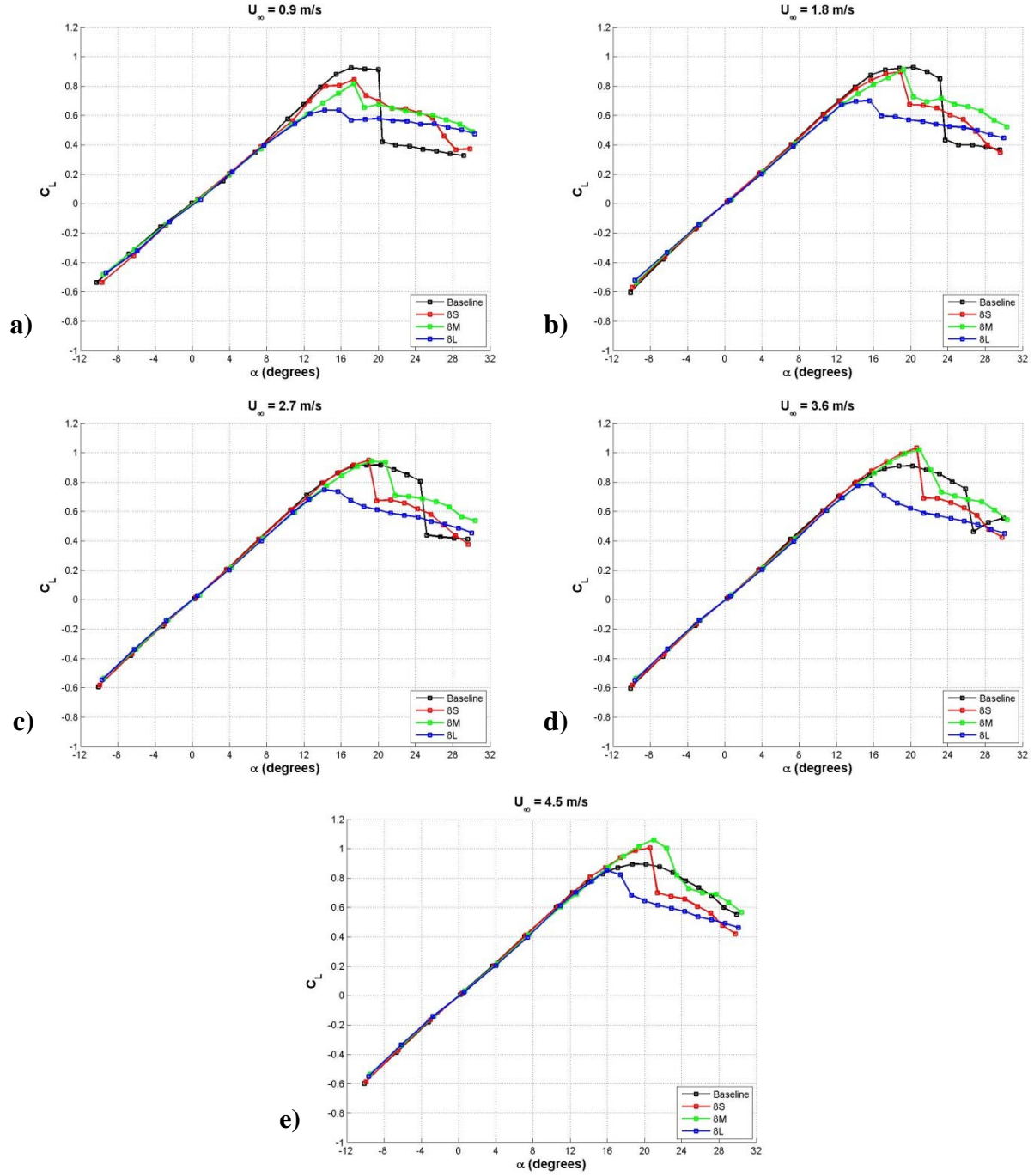
Figure 24. Effect of protuberance amplitude on the lift-to-drag ratio of finite-span rectangular planform hydrofoils, $\lambda = 0.50c$. a) $Re_c = 9.0 \times 10^4$, b) $Re_c = 1.8 \times 10^5$, c) $Re_c = 2.7 \times 10^5$, d) $Re_c = 3.6 \times 10^5$, e) $Re_c = 4.5 \times 10^5$.

Shorter wavelength λ = 0.25c

The effect of protuberance amplitude on the lift of modified hydrofoils with a wavelength of $\lambda = 0.25c$ is presented in Fig. 25. At lower freestream velocities, in the range of $0.9 \leq U_\infty \leq 2.7$ m/s, the trends in lift coefficient are very similar to those observed in Figure 21 for hydrofoils with wavelength $\lambda = 0.50c$, with maximum lift coefficients either nearly equal to or less than the baseline lift coefficient. All modified hydrofoils produced more lift in the early post-stall regime, generating as much as 65% more lift than the baseline hydrofoil. However, contrary to hydrofoils with longer protuberance wavelength, the lift coefficient of the 8S hydrofoil is typically greater in the post-stall regime.

At freestream velocities of $3.6 \leq U_\infty \leq 4.5$ m/s, the 8S and 8M hydrofoils had greater maximum lift than the baseline hydrofoil, with the 8S hydrofoil generating nearly 13% more lift at a freestream velocity of 3.6 m/s and the 8M hydrofoil generating 18% more lift at 4.5 m/s. The baseline hydrofoil generally had a larger lift coefficient in the post-stall regime than the 8M and 8L hydrofoils, while the 8S hydrofoil typically produced nearly equal or greater lift than the baseline hydrofoil.

The drag coefficients of modified hydrofoils with $\lambda = 0.25c$ are compared in Figure 26. Similar to the modified hydrofoils with a protuberance wavelength of $\lambda = 0.50c$, the drag coefficient is either nearly equal to or greater than the baseline model at both intermediate and higher angles of attack.

The pitching moment coefficient about the quarter-chord point and the lift-to-drag ratio of hydrofoils with a protuberance wavelength of $\lambda = 0.25c$, shown in Figs. 27 and 28, exhibit similar performance characteristics to those described in the previous section for the modified hydrofoils with a protuberance wavelength of $\lambda = 0.50c$.

Figure 25. Effect of protuberance amplitude on the lift coefficient of finite-span rectangular planform hydrofoils, $\lambda = 0.25c$. a) $Re_c = 9.0 \times 10^4$, b) $Re_c = 1.8 \times 10^5$, c) $Re_c = 2.7 \times 10^5$, d) $Re_c = 3.6 \times 10^5$, e) $Re_c = 4.5 \times 10^5$.
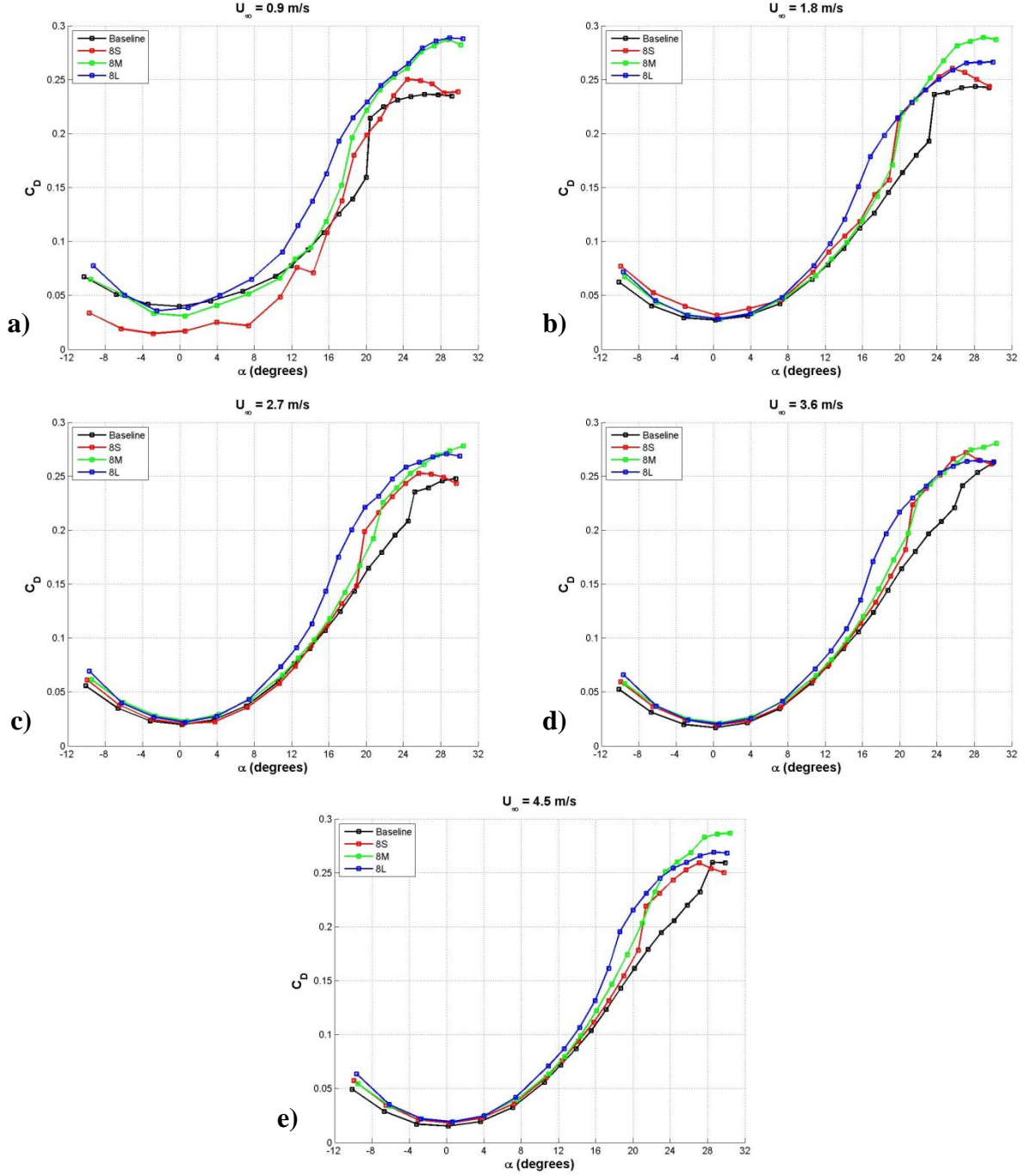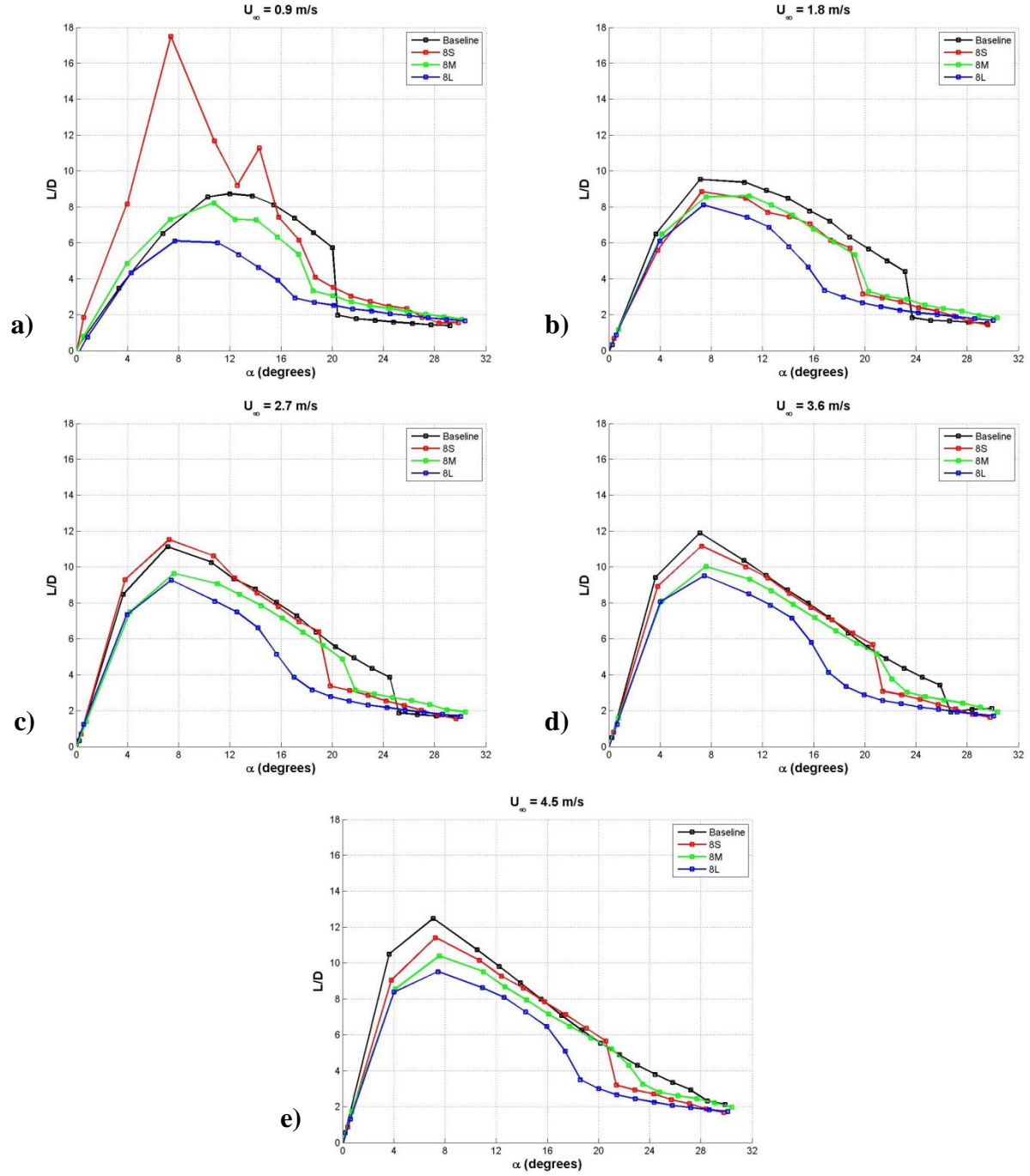
Figure 26. Effect of protuberance amplitude on the drag coefficient of finite-span rectangular planform hydrofoils, $\lambda = 0.25c$. a) $Re_c = 9.0 \times 10^4$, b) $Re_c = 1.8 \times 10^5$, c) $Re_c = 2.7 \times 10^5$, d) $Re_c = 3.6 \times 10^5$, e) $Re_c = 4.5 \times 10^5$.
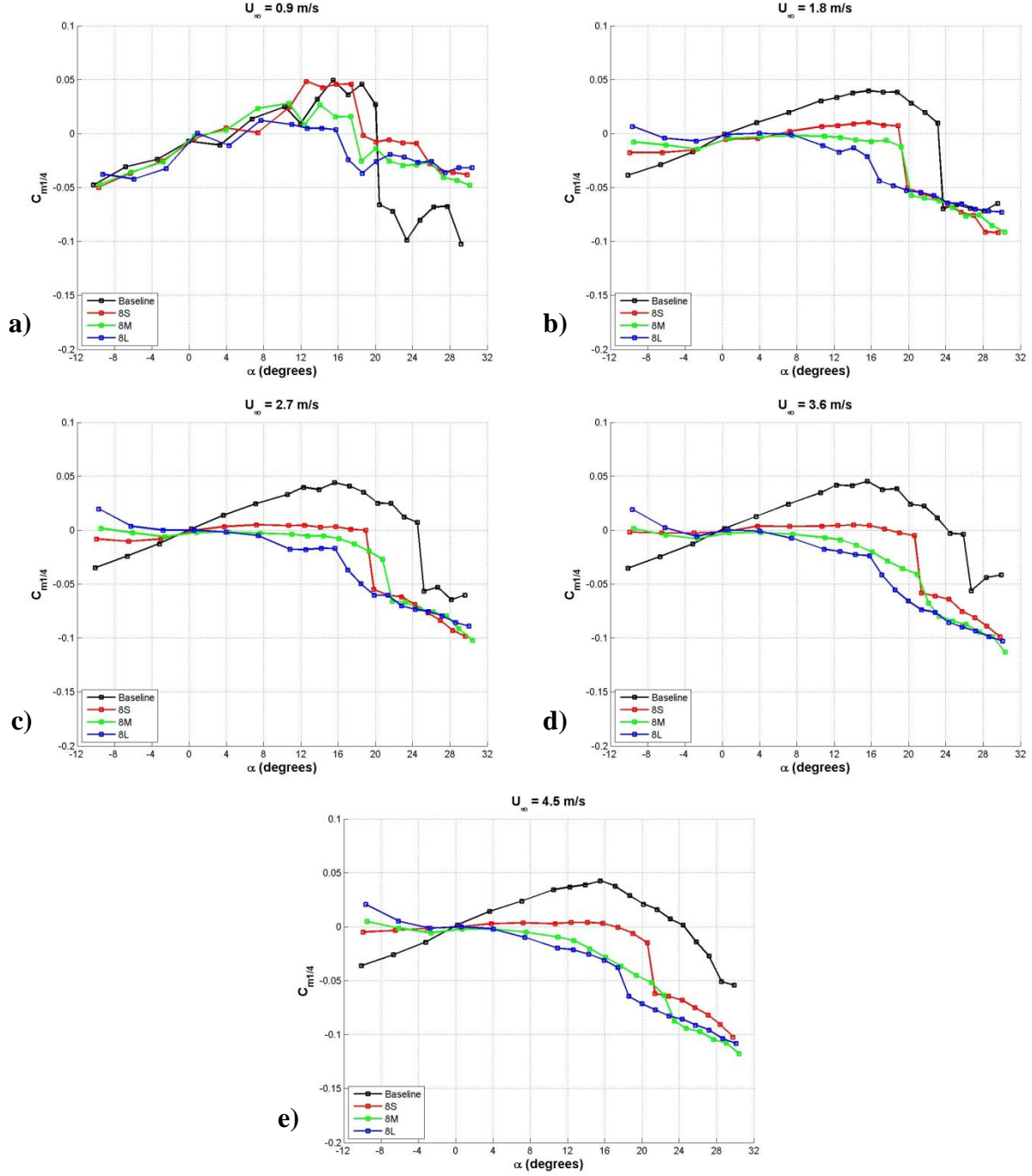
Figure 27. Effect of protuberance amplitude on the pitching moment coefficient of finite-span rectangular planform hydrofoils, $\lambda = 0.25c$. a) $Re_c = 9.0 \times 10^4$, b) $Re_c = 1.8 \times 10^5$, c) $Re_c = 2.7 \times 10^5$, d) $Re_c = 3.6 \times 10^5$, e) $Re_c = 4.5 \times 10^5$.

Figure 28. Effect of protuberance amplitude on the lift-to-drag ratio of finite-span rectangular planform hydrofoils, $\lambda = 0.25c$. a) $Re_c = 9.0 \times 10^4$, b) $Re_c = 1.8 \times 10^5$, c) $Re_c = 2.7 \times 10^5$, d) $Re_c = 3.6 \times 10^5$, e) $Re_c = 4.5 \times 10^5$.

Effect of protuberance wavelength

The data presented in the previous section are re-plotted in this section to examine the effect of protuberance wavelength on the hydrodynamic characteristics of finite-span rectangular planform hydrofoils at fixed amplitude.

Small amplitude A = 0.025c

The effect of wavelength on the lift characteristics of modified hydrofoils with protuberance amplitude of $A = 0.025c$ is presented in Fig. 29. For all Reynolds numbers examined, C_L of the shorter wavelength 8S hydrofoil was either equal to greater than (to within experimental uncertainty) the longer wavelength 4S hydrofoil. At freestream velocities of $0.9 \leq U_\infty \leq 2.7$ m/s, the lift characteristics of modified hydrofoils with protuberance amplitudes of $0.025c$ are very similar throughout the range of angles of attack examined. However, as freestream velocity is increased, the lift performance of the 8S hydrofoil at angles of attack from $15° \leq \alpha \leq 22°$ is slightly enhanced, with an increase in maximum C_L of 13% and 12% over the baseline and 4S hydrofoils at freestream velocities of 3.6 and 4.5 m/s, respectively. While the trends in the lift coefficient of the 4S and 8S hydrofoils differ significantly from the baseline hydrofoil, the lift coefficients of the two modified hydrofoils are similar throughout the range of angles of attack.

The effect of wavelength on the drag characteristics of modified hydrofoils with protuberance amplitude of $0.025c$ is shown in Fig. 30. The drag characteristics of the modified hydrofoils at the lowest protuberance amplitude are very similar over the range of angles and Reynolds numbers tested.

With the exception of the lowest freestream velocity tested, in which low Reynolds number effects dominate, wavelength affects the pitching moment coefficient in such a way that with decreasing wavelength, $C_{M1/4}$ increases. At post-stall angles of attack, the hydrofoil with smaller protuberance wavelength has a slightly increased moment coefficient. The effect of protuberance wavelength on the moment coefficient quarter chord is shown in Fig. 31.

At freestream velocities greater than $U_\infty = 0.9$ m/s, the lift-to-drag ratio is largely unaffected by protuberance wavelength. Both modified hydrofoils have L/D values equal or smaller than the baseline hydrofoil. The hydrofoil with the smaller protuberance wavelength consistently has a slightly greater stall angle than that of the hydrofoil with the larger wavelength. The dependence of lift-to-drag ratio on the protuberance wavelength of modified hydrofoils is shown in Fig. 32.
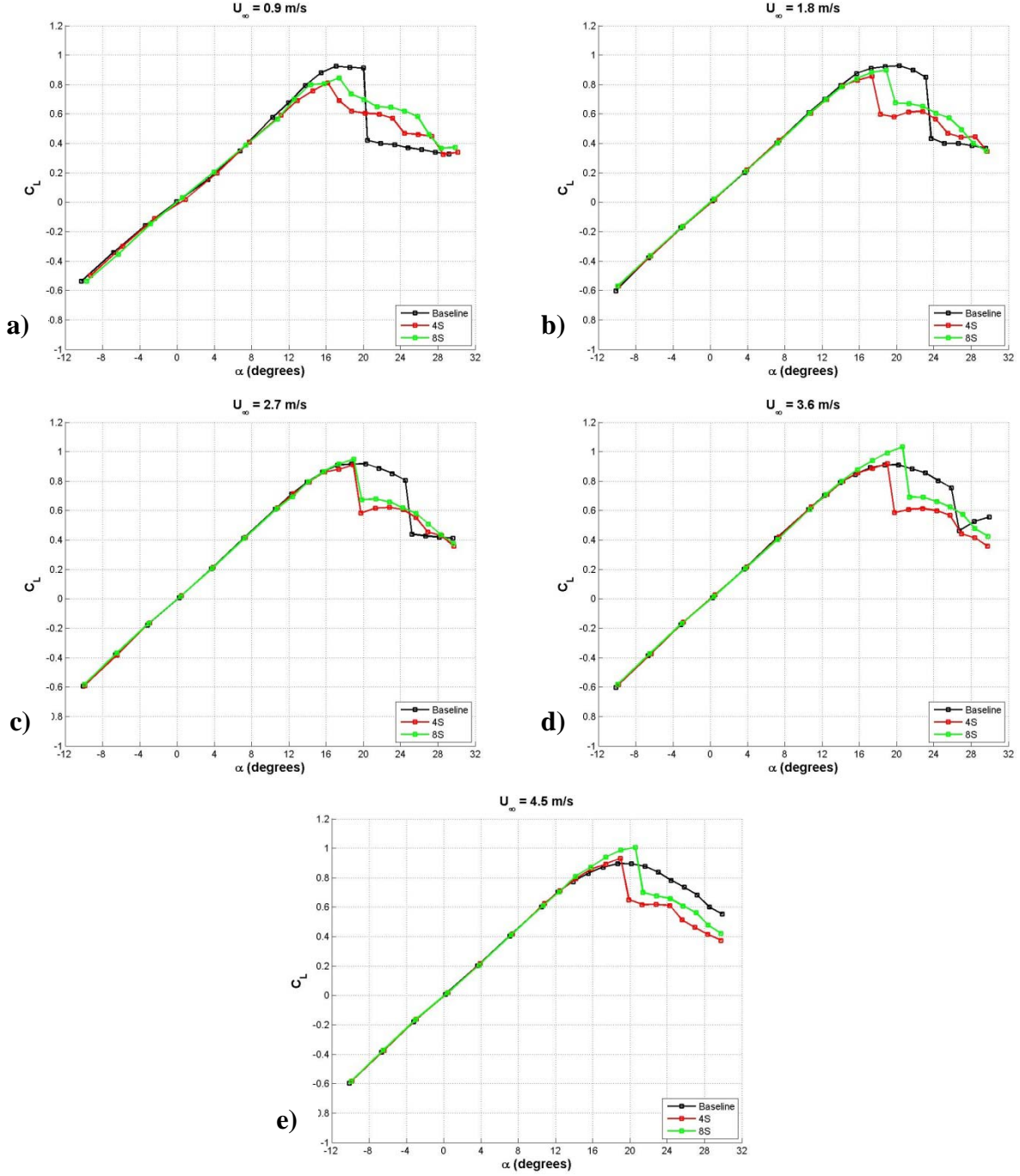
Figure 29. Effect of protuberance wavelength on the lift coefficient of finite-span rectangular planform hydrofoils, $A = 0.025c$. a) $Re_c = 9.0 \times 10^4$, b) $Re_c = 1.8 \times 10^5$, c) $Re_c = 2.7 \times 10^5$, d) $Re_c = 3.6 \times 10^5$, e) $Re_c = 4.5 \times 10^5$.
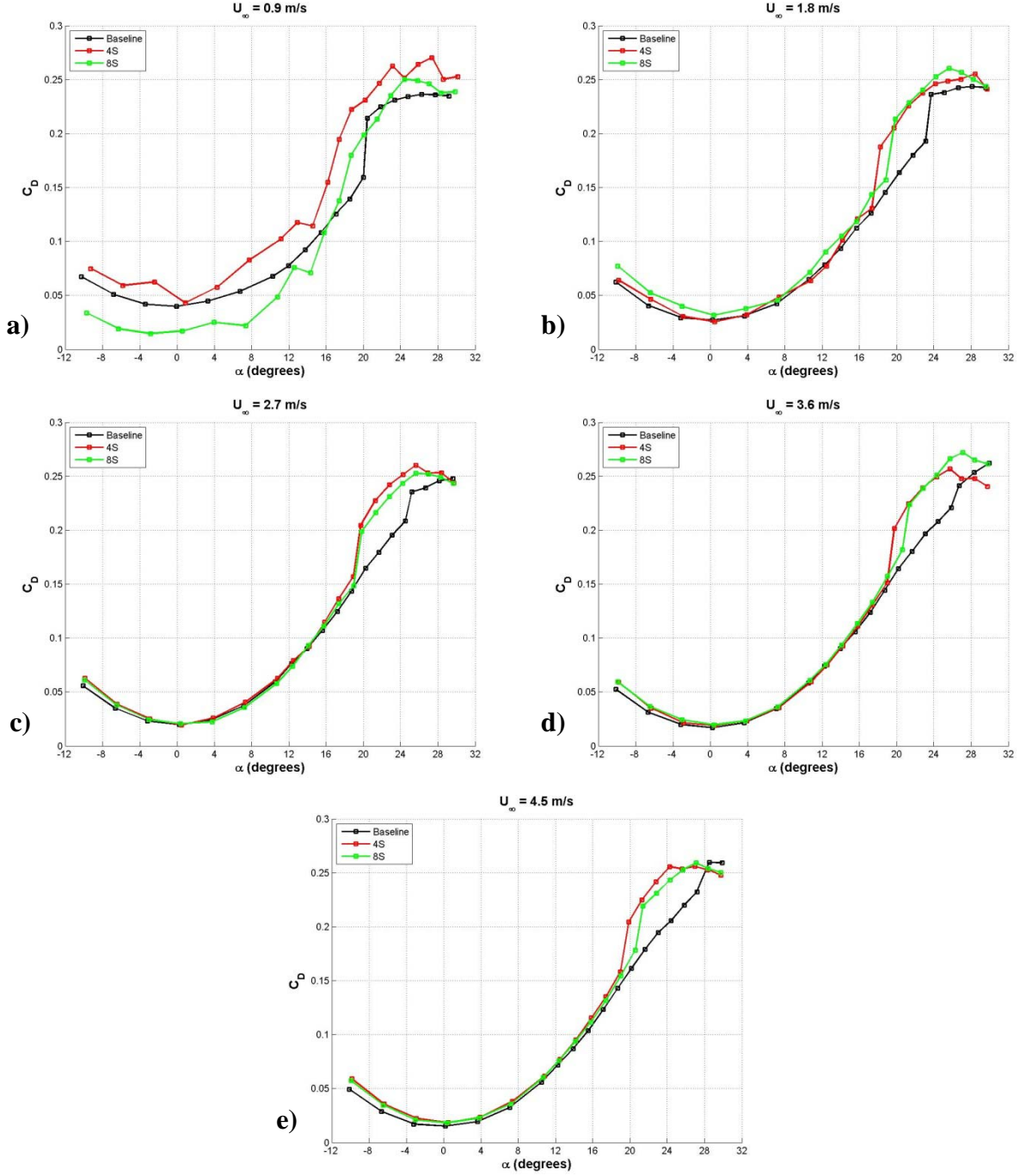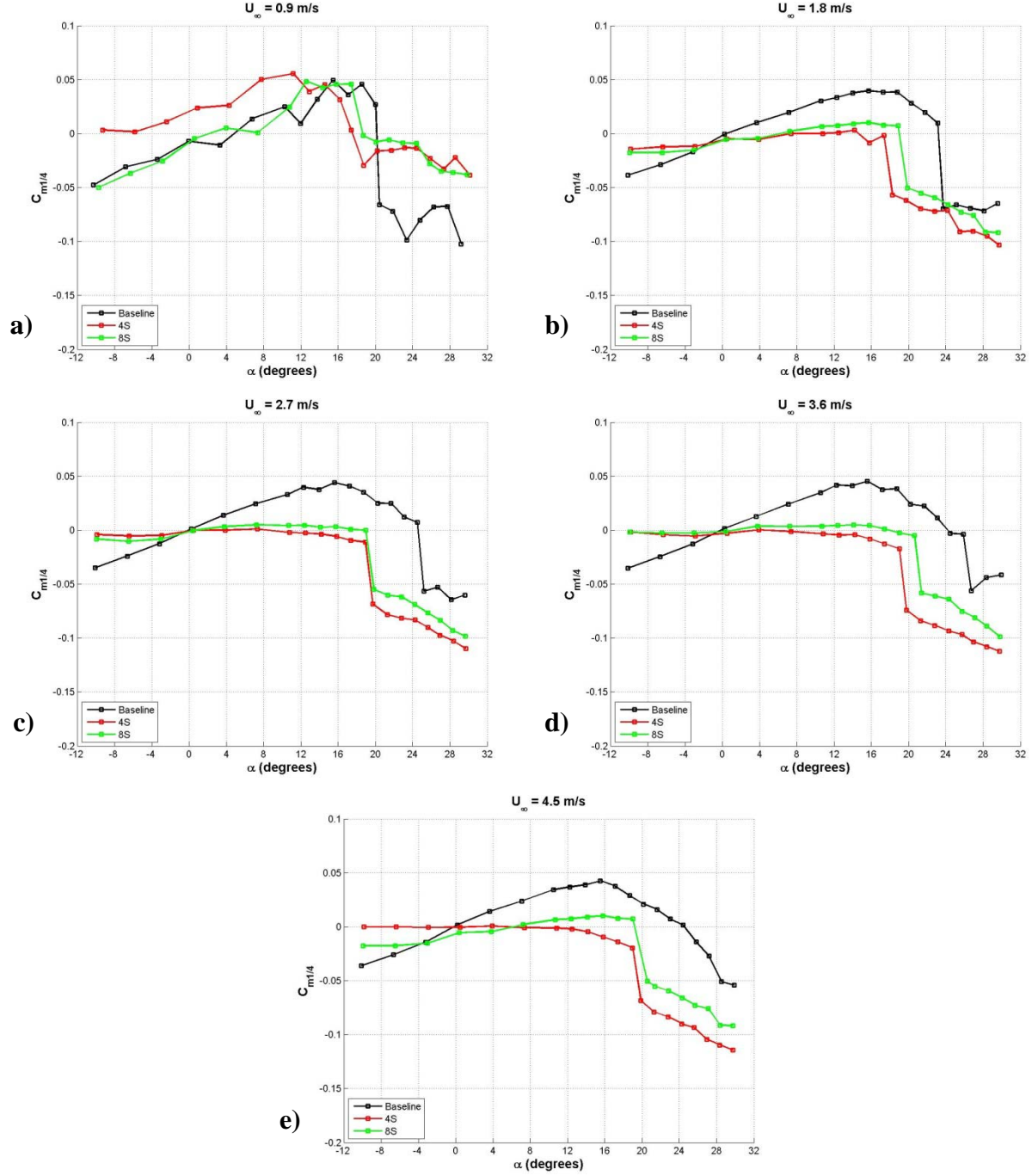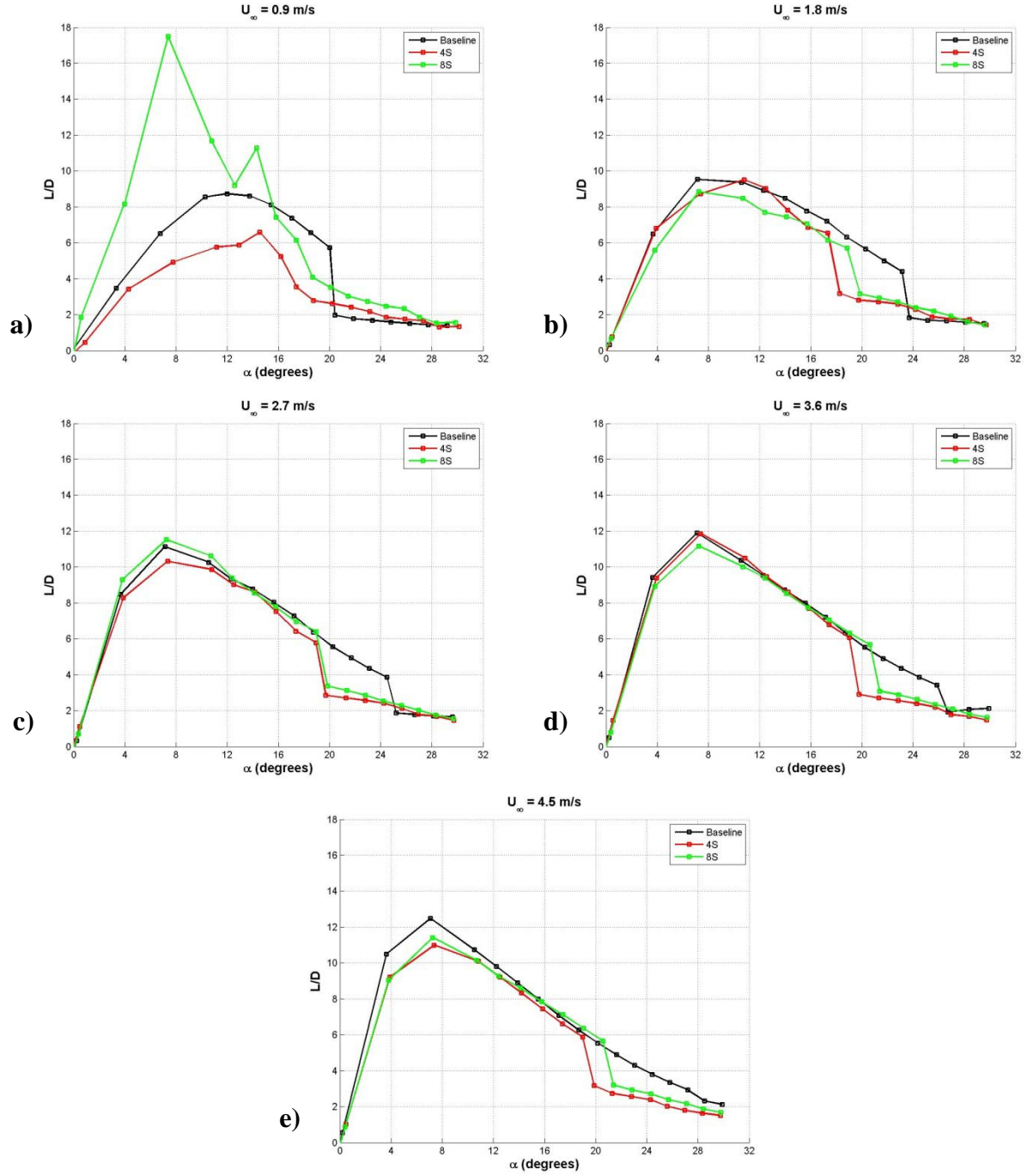
Figure 30. Effect of protuberance wavelength on the drag coefficient of finite-span rectangular planform hydrofoils, $A = 0.025c$. a) $Re_c = 9.0 \times 10^4$, b) $Re_c = 1.8 \times 10^5$, c) $Re_c = 2.7 \times 10^5$, d) $Re_c = 3.6 \times 10^5$, e) $Re_c = 4.5 \times 10^5$.

Figure 31. Effect of protuberance wavelength on the pitching moment coefficient of finite-span rectangular planform hydrofoils, $A = 0.025c$. a) $Re_c = 9.0 \times 10^4$, b) $Re_c = 1.8 \times 10^5$, c) $Re_c = 2.7 \times 10^5$, d) $Re_c = 3.6 \times 10^5$, e) $Re_c = 4.5 \times 10^5$.

50

Figure 32. Effect of protuberance wavelength on the lift-to-drag ratio of finite-span rectangular planform hydrofoils, $A = 0.025c$. a) $Re_c = 9.0 \times 10^4$, b) $Re_c = 1.8 \times 10^5$, c) $Re_c = 2.7 \times 10^5$, d) $Re_c = 3.6 \times 10^5$, e) $Re_c = 4.5 \times 10^5$.

Medium amplitude A = 0.050c

The effect of wavelength on the lift characteristics of modified hydrofoils with the medium protuberance amplitude of $A = 0.05c$ is presented in Fig. 33. For all Reynolds numbers tested, the shorter wavelength 8M hydrofoil consistently generated a similar or greater lift coefficient than the 4M hydrofoil over the range of angles examined, with a maximum difference between modified hydrofoils of nearly 60% at Reynolds numbers of $U_\infty = 3.6$ and 4.5 m/s. Both modified hydrofoils showed signs of stall, with the 8M hydrofoil consistently stalling at a higher angle of attack than the 4M hydrofoil. At freestream velocities of 3.6 and 4.5 m/s, the 8M had a lift coefficient that is nearly equal to or greater than the baseline hydrofoil throughout the range of angles attack examined. Over the range of angle of attack $15° \leq \alpha \leq 22°$, the 8M hydrofoil produced as much as 18% more lift than the baseline hydrofoil at an angle of attack of 21°.

The effect of wavelength on the drag characteristics of modified hydrofoils with protuberance amplitudes of $0.50c$ is shown in Fig. 34. At freestream velocities of $0.9 \leq U_\infty \leq 2.7$ m/s, C_D of the longer wavelength 4M hydrofoil was as much as 36% greater than the 8M hydrofoil over the range of angles of attack of $15° \leq \alpha \leq 21°$. However, at freestream velocities of 2.7 and 3.6 m/s, C_D of the 4M and 8M hydrofoils were quite similar, to within experimental uncertainty. The likely cause of this phenomenon was the existence of stall at the lower Reynolds numbers.

With the exception of post-stall angles of attack, in which both modified hydrofoils show similar $C_{M1/4}$, the general trends of both $C_{M1/4}$ and L/D on hydrofoils with a protuberance amplitude of $A = 0.05c$ show performance characteristics that are very similar to those observed in the previous section for the smaller protuberance amplitude of $A = 0.025c$. The pitching moment coefficient at the quarter-chord position and the lift-to-drag ratio of the modified foils with a protuberance amplitude of $A = 0.05c$ are presented in Figs. 35 and 36.
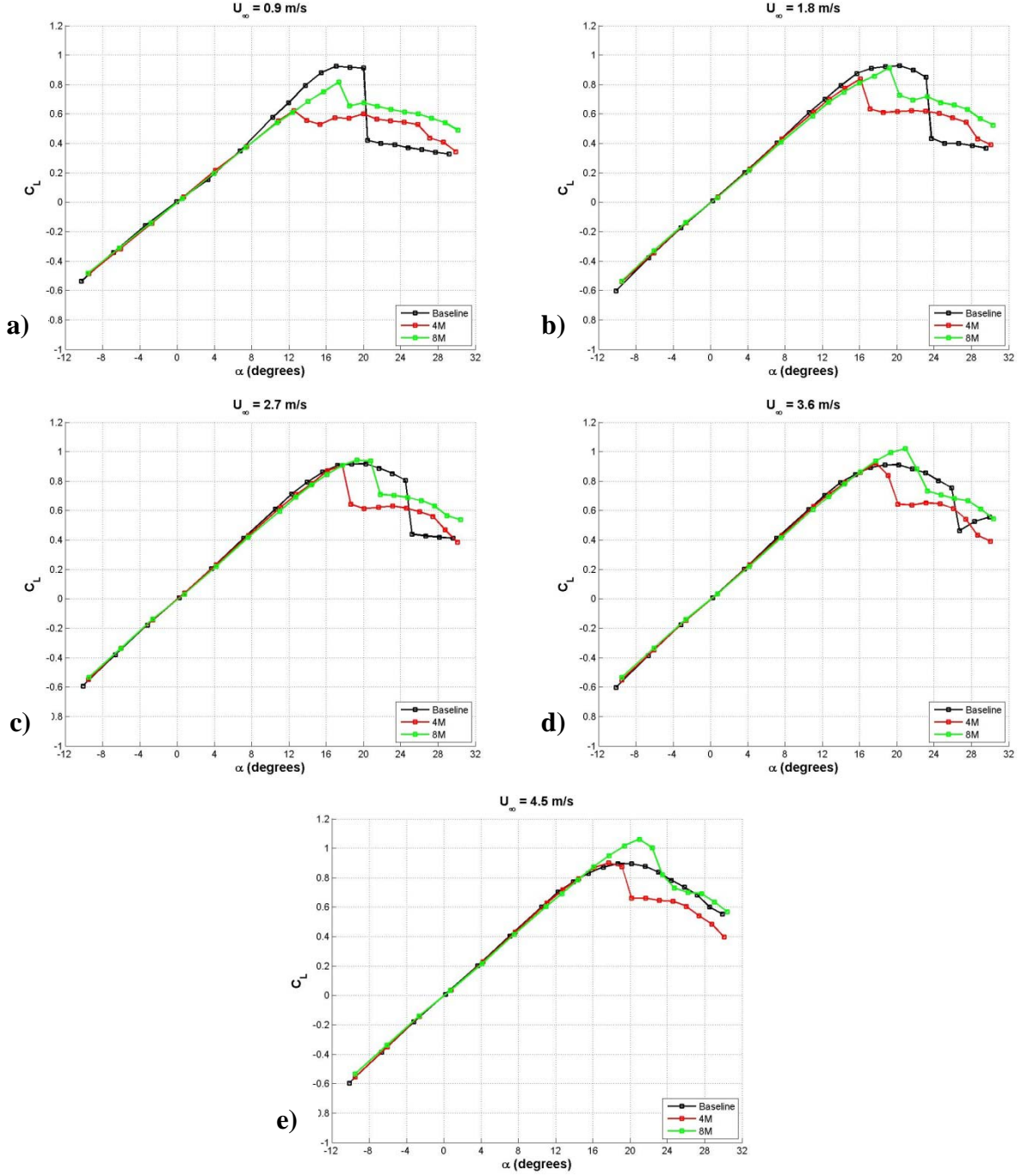
Figure 33. Effect of protuberance wavelength on the lift coefficient of finite-span rectangular planform hydrofoils, $A = 0.050c$. a) $Re_c = 9.0 \times 10^4$, b) $Re_c = 1.8 \times 10^5$, c) $Re_c = 2.7 \times 10^5$, d) $Re_c = 3.6 \times 10^5$, e) $Re_c = 4.5 \times 10^5$.
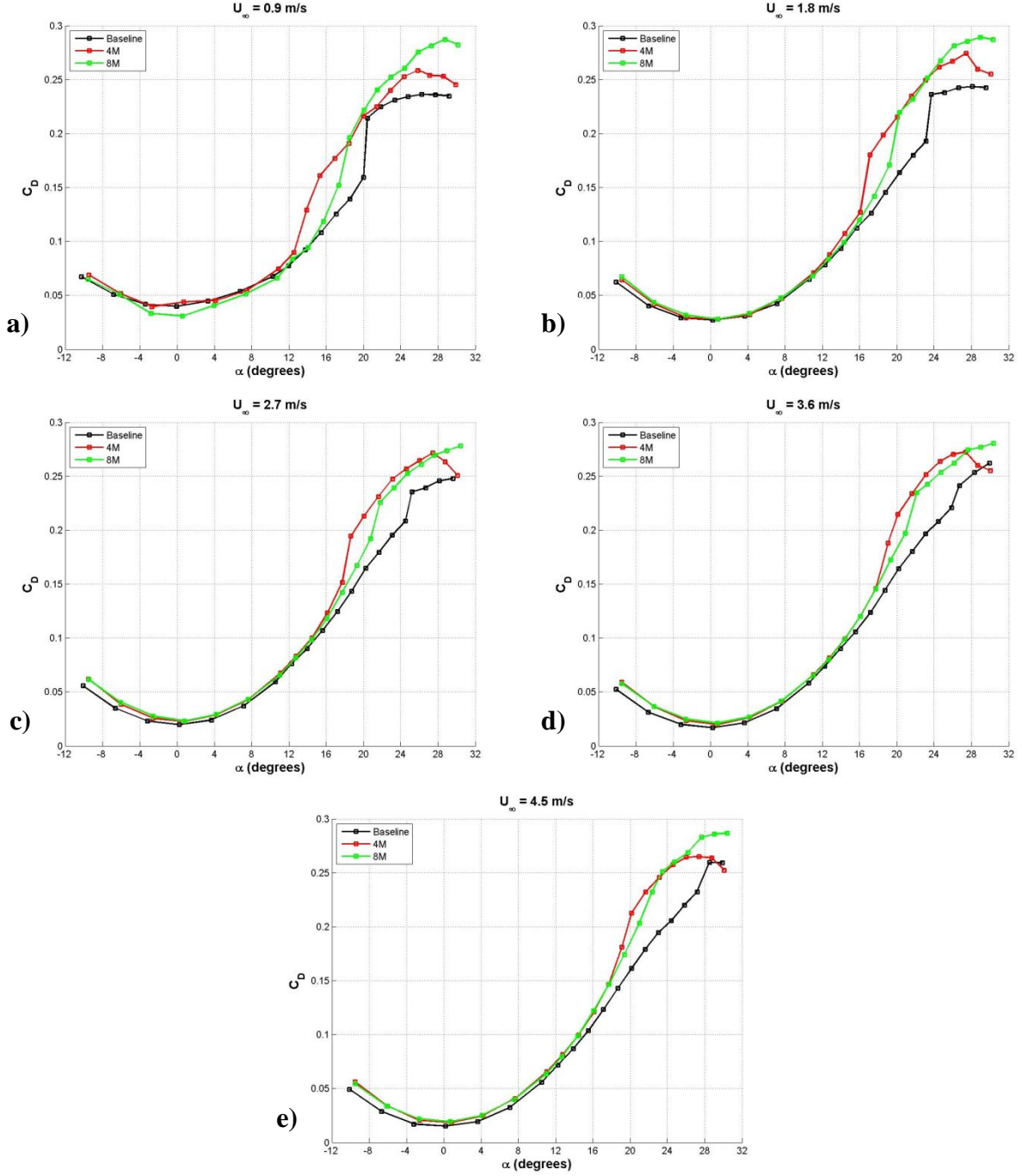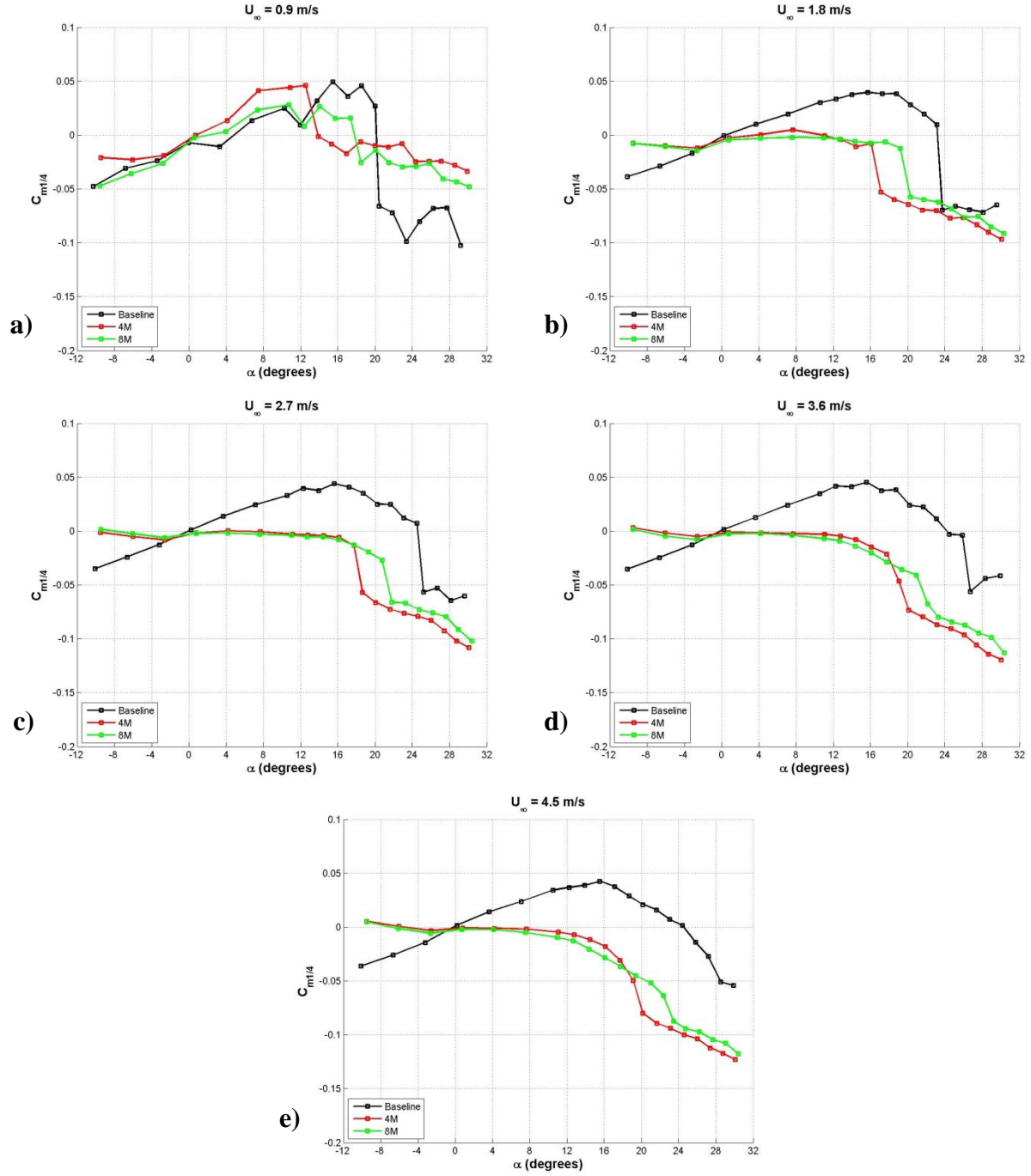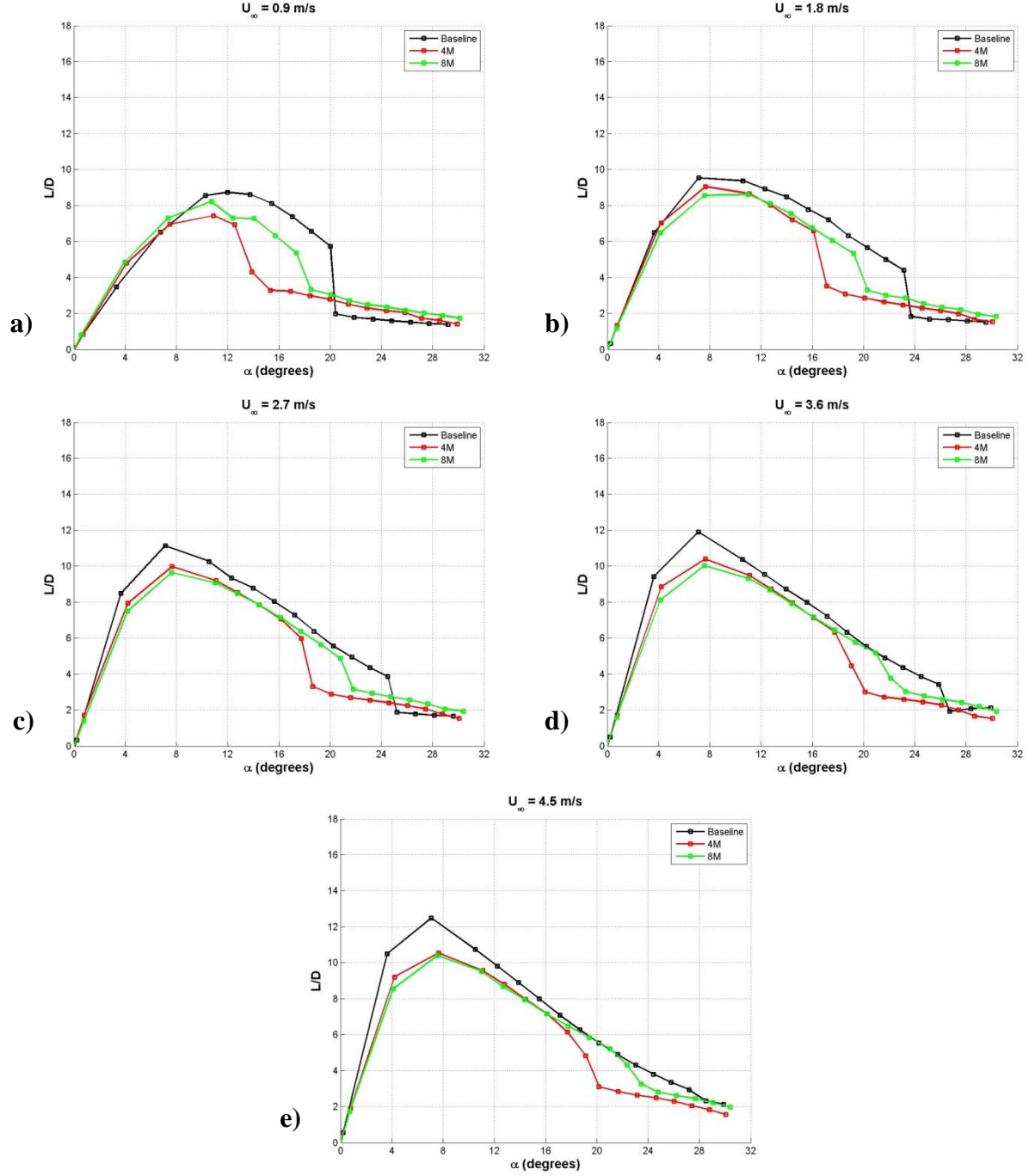
Figure 34. Effect of protuberance wavelength on the drag coefficient of finite-span rectangular planform hydrofoils, $A = 0.050c$. a) $Re_c = 9.0 \times 10^4$, b) $Re_c = 1.8 \times 10^5$, c) $Re_c = 2.7 \times 10^5$, d) $Re_c = 3.6 \times 10^5$, e) $Re_c = 4.5 \times 10^5$.

Figure 35. Effect of protuberance wavelength on the pitching moment coefficient of finite-span rectangular planform hydrofoils, $A = 0.050c$. a) $Re_c = 9.0 \times 10^4$, b) $Re_c = 1.8 \times 10^5$, c) $Re_c = 2.7 \times 10^5$, d) $Re_c = 3.6 \times 10^5$, e) $Re_c = 4.5 \times 10^5$.

Figure 36. Effect of protuberance wavelength on the lift-to-drag ratio of finite-span rectangular planform hydrofoils, $A = 0.050c$. a) $Re_c = 9.0 \times 10^4$, b) $Re_c = 1.8 \times 10^5$, c) $Re_c = 2.7 \times 10^5$, d) $Re_c = 3.6 \times 10^5$, e) $Re_c = 4.5 \times 10^5$.

Large amplitude A = 0.12 c

The effect of wavelength on the lift characteristics of modified hydrofoils with the largest protuberance amplitude of $A = 0.12c$ is shown in Figure 37. The lift coefficient trends of hydrofoils with the large amplitude leading edge protuberances differ considerably from those of hydrofoils with the two smaller amplitudes. Whereas the lift coefficient of hydrofoils with a shorter protuberance wavelength typically produced a higher C_L than hydrofoils with a longer protuberance wavelength at the smaller amplitudes, this trend is reversed on hydrofoils with protuberance amplitudes of $0.12c$. At the lowest freestream velocity examined, $U_\infty = 0.90$ m/s, the C_L curves for the 4L and 8L hydrofoils are very similar. As the freestream velocity is increased, the difference in C_L between the 4L and 8L hydrofoils becomes more pronounced. The 4L hydrofoil creates more lift than the 8L hydrofoil at all freestream velocities greater than 0.90 m/s, generating as much as 32% more lift than the 8L hydrofoil at $U_\infty = 4.5$ m/s. As freestream velocity is increased, the trends seen in the lift coefficient of both 4L and 8L hydrofoils become increasingly similar to the baseline hydrofoil, with C_L of the 4L hydrofoil always being less than the baseline hydrofoil at 4.5 m/s.

The dependence of drag characteristics of modified hydrofoils on protuberance wavelength at the amplitude of $0.12c$ is shown in Figure 38. Protuberance wavelength plays only a minor role in establishing the drag characteristics of modified hydrofoils at the largest amplitude. For all freestream velocities, C_D curves are very similar for both wavelengths examined. However, at freestream velocities ranging from $1.8 \leq U_\infty \leq 4.5$ m/s, C_D of the 4L was generally greater at angles of attack ranging from $21° \leq \alpha \leq 30°$, with a maximum difference of 15% between the two hydrofoil models.

With the exception of very low freestream velocity, both $C_{M1/4}$ and *L/D* for the hydrofoils with a protuberance amplitude of $A = 0.12c$ are very similar with only minor differences throughout the range of angles of attack tested. The pitching moment coefficient at the quarter-chord point and the lift-to-drag ratio of the modified hydrofoils with a protuberance amplitude of $A = 0.12c$ are shown in Figs. 39 and 40.
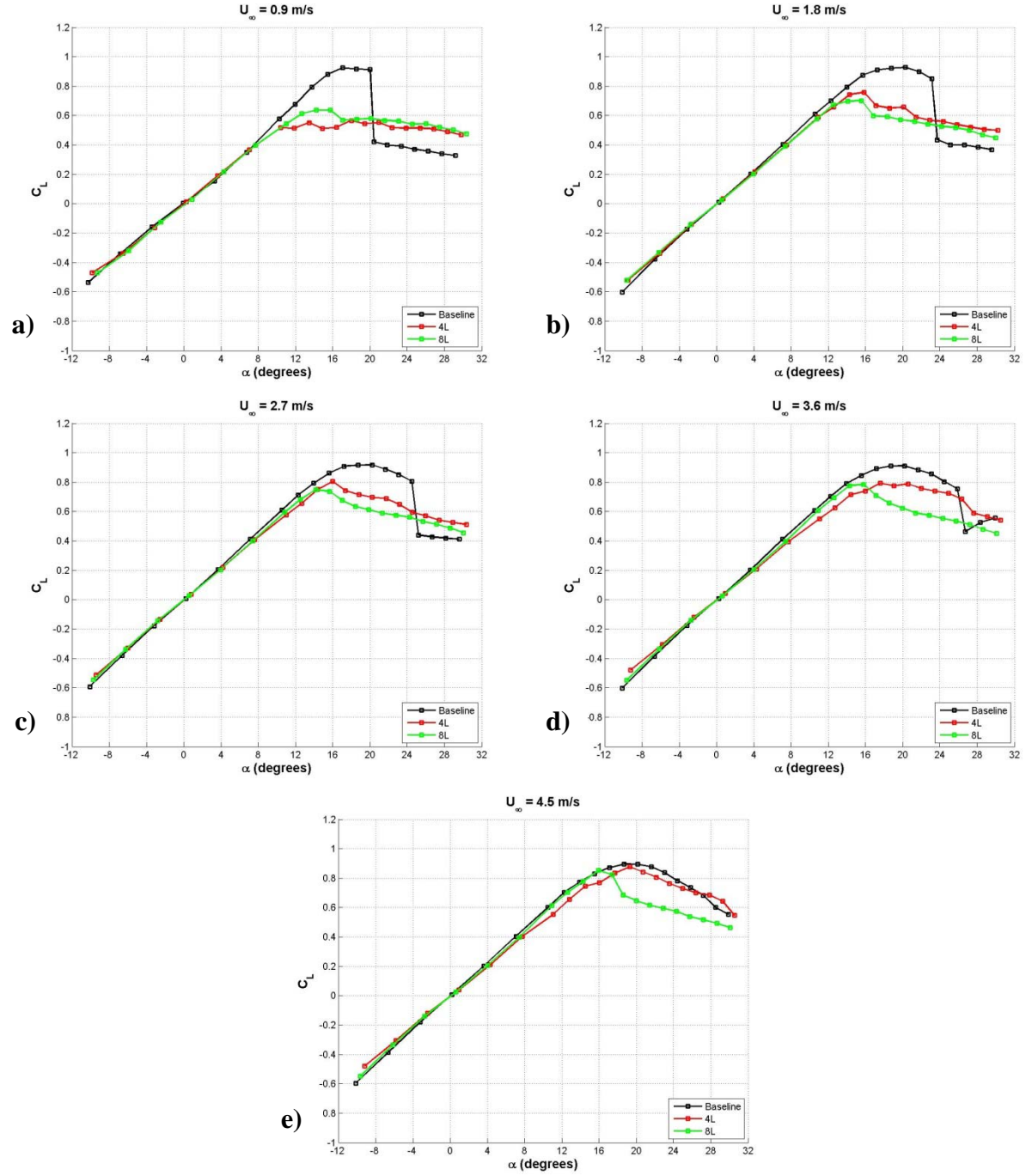
Figure 37. Effect of protuberance wavelength on the lift coefficient of finite-span rectangular planform hydrofoils, $A = 0.120c$. a) $Re_c = 9.0 \times 10^4$, b) $Re_c = 1.8 \times 10^5$, c) $Re_c = 2.7 \times 10^5$, d) $Re_c = 3.6 \times 10^5$, e) $Re_c = 4.5 \times 10^5$.
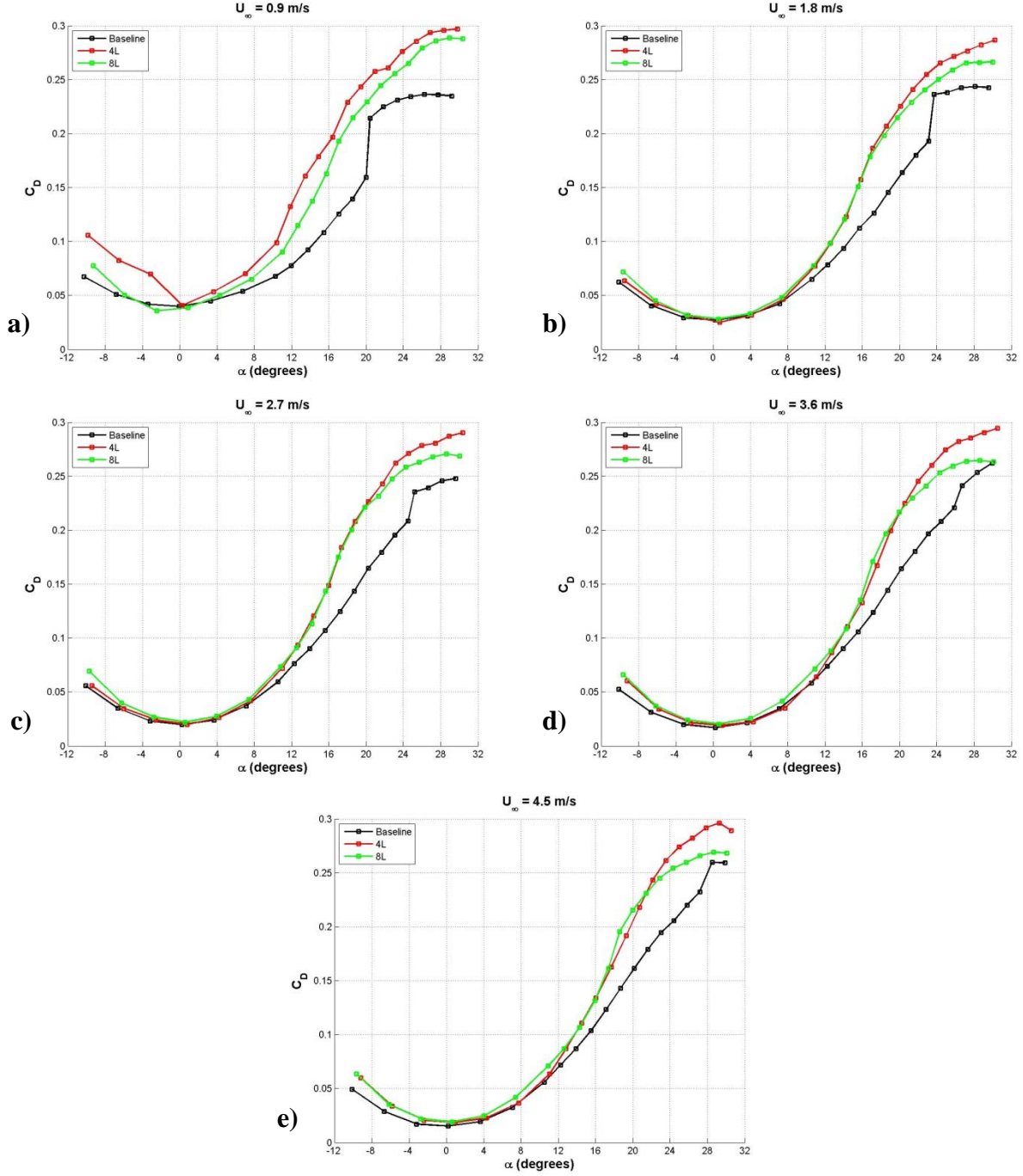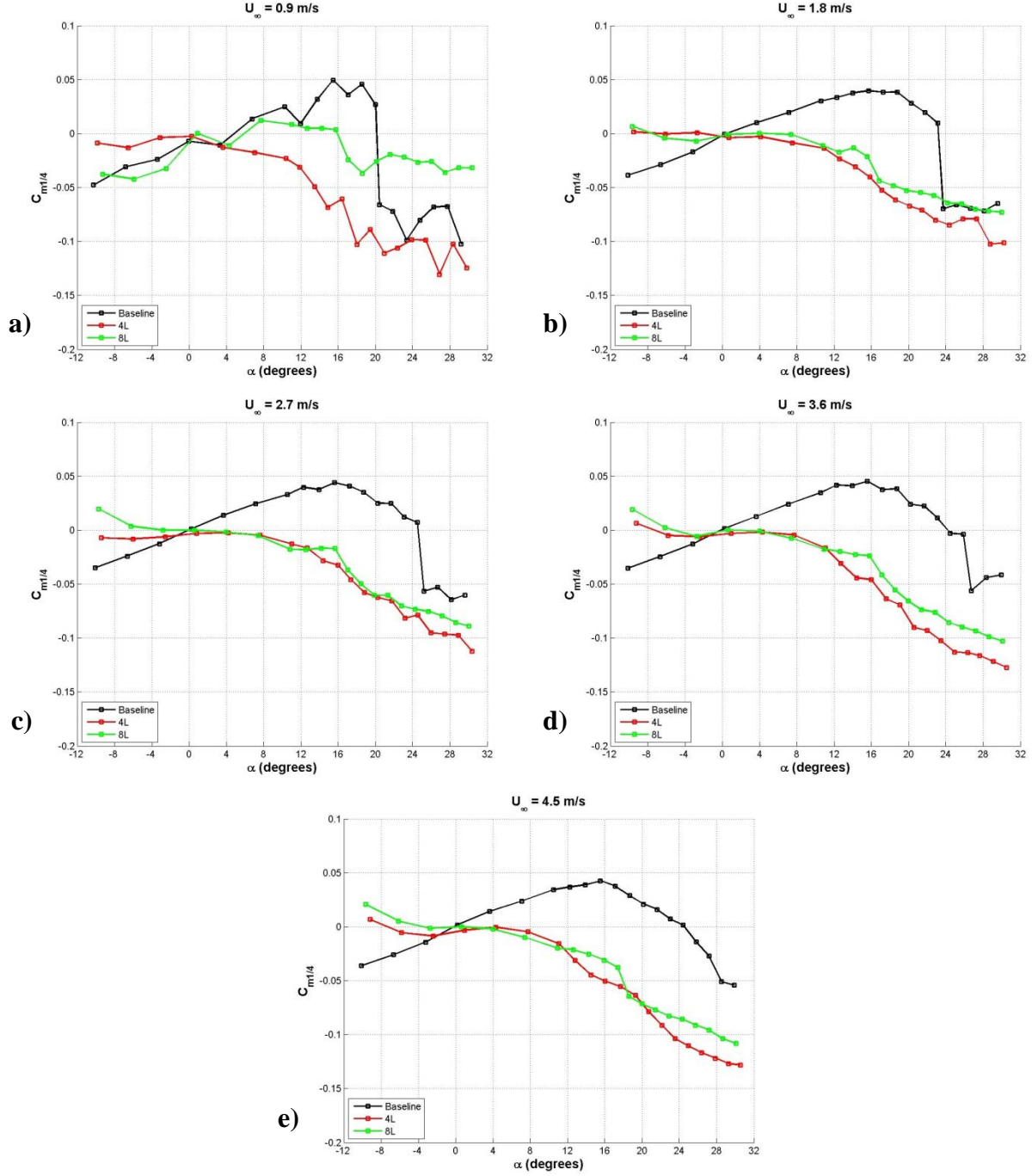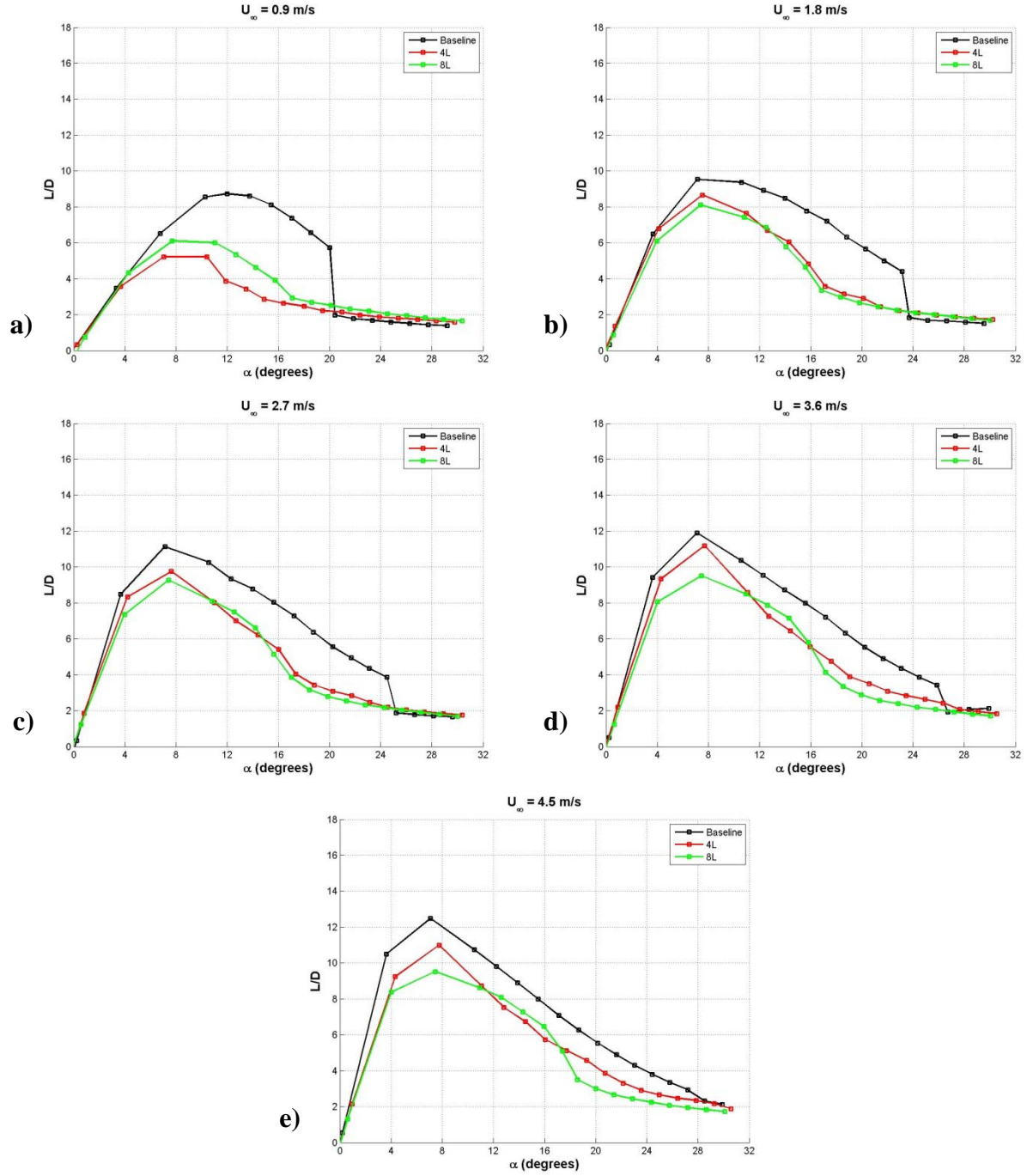
Figure 38. Effect of protuberance wavelength on the drag coefficient of finite-span rectangular planform hydrofoils, $A = 0.120c$. a) $Re_c = 9.0 \times 10^4$, b) $Re_c = 1.8 \times 10^5$, c) $Re_c = 2.7 \times 10^5$, d) $Re_c = 3.6 \times 10^5$, e) $Re_c = 4.5 \times 10^5$.

Figure 39. Effect of protuberance wavelength on the pitching moment coefficient of finite-span rectangular planform hydrofoils, $A = 0.120c$. a) $Re_c = 9.0 \times 10^4$, b) $Re_c = 1.8 \times 10^5$, c) $Re_c = 2.7 \times 10^5$, d) $Re_c = 3.6 \times 10^5$, e) $Re_c = 4.5 \times 10^5$.

Figure 40. Effect of protuberance wavelength on the lift-to-drag ratio of finite-span rectangular planform hydrofoils, $A = 0.120c$. a) $Re_c = 9.0 \times 10^4$, b) $Re_c = 1.8 \times 10^5$, c) $Re_c = 2.7 \times 10^5$, d) $Re_c = 3.6 \times 10^5$, e) $Re_c = 4.5 \times 10^5$.

Swept Planform Hydrofoils

Baseline model

The lift coefficient data for the swept planform, baseline hydrofoil in Fig. 41 reveal that there are two distinct Reynolds number regimes as far as C_L is concerned. These regimes correspond to freestream velocity ranges of $0.9 \leq U_\infty \leq 1.8$ m/s and $2.7 \leq U_\infty \leq 4.5$ m/s. At the lower freestream velocities, C_L increases linearly with angle of attack over the range of $0 \leq \alpha \leq 6°$ angles of attack. Past $\alpha = 6°$, flow separation is indicated by a leveling off of C_L. At higher angles of attack, C_L decreases at low rate, without any sign of abrupt stall. On the other hand, for freestream velocities greater than $U_\infty = 1.8$ m/s, the linear regime of the lift coefficient is extended to significantly higher angles than for lower velocities, with the linear regime of C_L lying in the range of angles of attack $0 \leq \alpha \leq 20°$. Past the linear regime, C_L curves once again show leveling off of C_L, though only over a limited range of angles $21° \leq \alpha \leq 26°$. Stall is also apparent at the higher Reynolds number, with a dramatic decrease in C_L for freestream velocities greater than $U_\infty = 1.8$ m/s. The stall angle increases with Reynolds number. With the exception of stall angle, C_L is similar for all freestream velocities above 1.8 m/s, to within experimental uncertainty.

The drag coefficient characteristics also reveal dependence on Reynolds number with the two distinct regimes once again being present, see Fig. 41b. While values for C_D are similar in either regime separately, the two regimes differ significantly, with as much as 32% higher C_D in the pre-stall regime. However, at very high and very low angles of attack, C_D is only a weak function of Reynolds number.

With the exception of slightly increasing stall angle, at Reynolds numbers greater than 1.8×10^5, $C_{M1/4}$ and L/D are largely unaffected by Reynolds number. However, at low Reynolds numbers, a larger variance in the trends can be seen. This is likely due to low Reynolds number effects in which flow is transitioning from laminar to turbulent, generating differences between the higher and lower Reynolds number regimes. The effect of Reynolds number on $C_{M1/4}$ and L/D, is shown in Fig. 41c and d. Table 16 shows the corresponding hydrodynamic characteristics of the swept baseline hydrofoil.
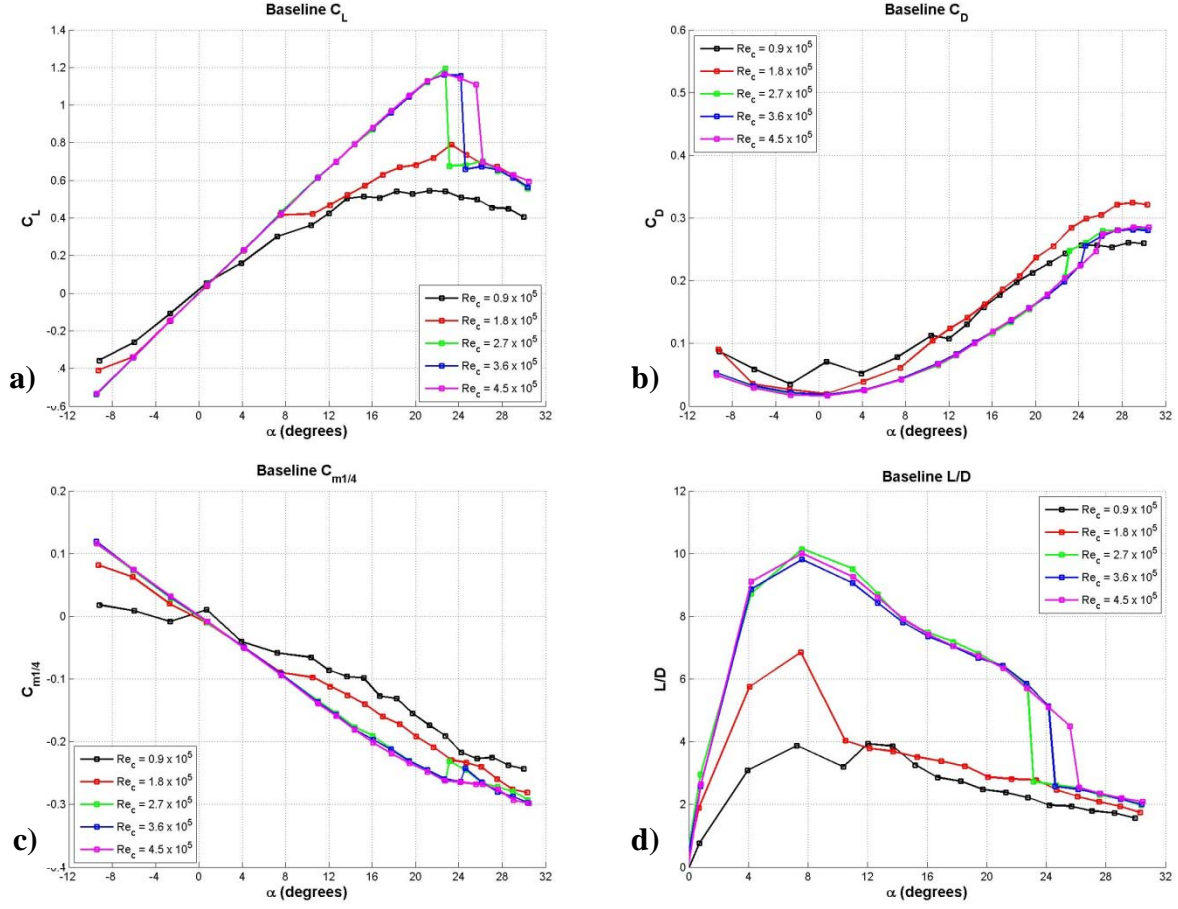
Figure 41. Effect of Reynolds number on the swept planform baseline hydrofoil characteristics: a) lift coefficient, b) drag coefficient, c) pitching moment coefficient, d) *L/D* ratio.

Table 16: Hydrodynamic characteristics of swept planform baseline hydrofoil.

	$Re_c = 9.0 \times 10^4$	$Re_c = 1.8 \times 10^5$	$Re_c = 2.7 \times 10^5$	$Re_c = 3.6 \times 10^5$	$Re_c = 4.5 \times 10^5$
$\frac{dC_L}{d\alpha}$ [deg^{-1}]	0.041	0.055	0.055	0.055	0.055
C_{Lmax}	0.54	0.79	1.19	1.16	1.17
$\alpha @ C_{Lmax}$ [deg]	21.3	23.3	22.7	22.7	22.7
C_{Dmin}	0.04	0.02	0.02	0.02	0.02
L/D_{max}	3.9	6.8	10.2	9.8	10.0
$\alpha @ L/D_{max}$ [deg]	12.0	7.5	7.6	7.6	7.6
α_{stall} [deg]	N/A	23.3	22.7	24.2	25.6

Modified model

The effects of Reynolds number on the modified swept planform hydrofoil are presented in Figure 42. As with the baseline hydrofoil, there are two Reynolds number regimes in which the lift coefficient curves are distinct, corresponding to freestream velocity ranges of $0.9 \leq U_\infty \leq 2.7$ m/s and $3.6 \leq U_\infty \leq 4.5$ m/s. Within each regime, the lift curves are quite similar. At angles of attack greater than $\alpha = 10°$, C_L at the higher Reynolds numbers is greater than the lower Reynolds numbers, with as much as 25% more lift generated at the highest freestream velocities tested. The drag coefficient of the modified hydrofoil was relatively unaffected by Reynolds number. The pitching moment coefficient at the quarter-chord point of the modified swept hydrofoil is also nearly unaffected by Reynolds number. However, similar distinction to those seen in the lift coefficient can be seen in L/D due to transition effects being present in the lift coefficient while drag is left unaffected. The effects of Reynolds number on $C_{M1/4}$ and L/D are presented in Figure 42.c and d.

The effect of leading edge protuberances on the load characteristics of the swept planform hydrofoil is shown in Figs. 43 – 46 where the data for the baseline is compared with the same for the modified hydrofoil. At freestream velocities of $0.9 \leq U_\infty \leq 1.8$ m/s, C_L for both the baseline and modified hydrofoils increases nearly linearly at lower angles of attack with the linear regime extending as the freestream velocity is increased. However, at low freestream velocities, the baseline C_L becomes level and reaches the stall angle prior to the modified hydrofoil. At higher angles of attack, C_L of the modified hydrofoil shows very little indication of stall, and generates as much as 150% more lift than the baseline hydrofoil. At freestream velocities greater than 1.8 m/s, both the baseline and modified hydrofoils show a linear increase in C_L with angle of attack at low angles. The baseline hydrofoil has a dramatic stall, as described above. For all freestream velocities above 1.8 m/s, the modified hydrofoil has smaller C_L than the baseline hydrofoil at pre-stall angles of attack. However, in the post-stall regime, the swept hydrofoil generates much higher lift for all freestream velocities above 1.8 m/s, producing as much as 100% greater lift at the freestream velocity of $U_\infty = 4.5$ m/s. At freestream velocities of 3.6 and 4.5 m/s, the maximum lift as well as angle of attack is increased, with 11% and 7% greater maximum lift generated on the modified hydrofoil than the baseline at 3.6 m/s and 4.5 m/s, respectively. Also, the lift curve slope is slightly different between the baseline and modified case, with values of $\frac{dC_{LBase}}{d\alpha} = 0.054$ and $\frac{dC_{LMod}}{d\alpha} = 0.048$ and 0.049 corresponding to freestream velocities of $U_\infty = 3.6$

and 4.5 m/s, respectively. There are two distinct Reynolds number regimes apparent in the lift data in which the lift coefficient at the lower Reynolds number of $0.9 \times 10^4 \leq Re_c \leq 2.7 \times 10^5$ are very similar, while the lift data at the higher Reynolds numbers of $3.6 \times 10^4 \leq Re_c \leq 4.5 \times 10^5$ are also very similar. This implies that there is a transition region in between the two Reynolds number regimes.

With the exception of very low angle of attack at the highest freestream velocities, the drag of the modified swept hydrofoil is significantly higher than the baseline for all angles of attack examined, see Fig. 44. Although the general trend of a quadratically increasing drag curve could be found at low angles in either the baseline or modified case, the value of C_D on the modified hydrofoil was either equal to, to within experimental uncertainty, or higher than the baseline for all freestream velocities examined, with as much as 100% higher drag at $U_\infty = 3.6$ m/s.

For all freestream velocities tested, $C_{M1/4}$ of the swept modified hydrofoil, shown in Fig. 45, is always similar to the baseline with the differences being within the measurement uncertainty. The lift-to-drag ratio of the swept planform hydrofoils shows that for all freestream velocities and angles of attack tested, L/D is either nearly equal to or less than the baseline case. The effect of protuberances on the lift-to-drag ratio of the swept planform hydrofoil is shown in Figure 46. Table 17 lists the hydrodynamic characteristics of the modified swept planform hydrofoil.
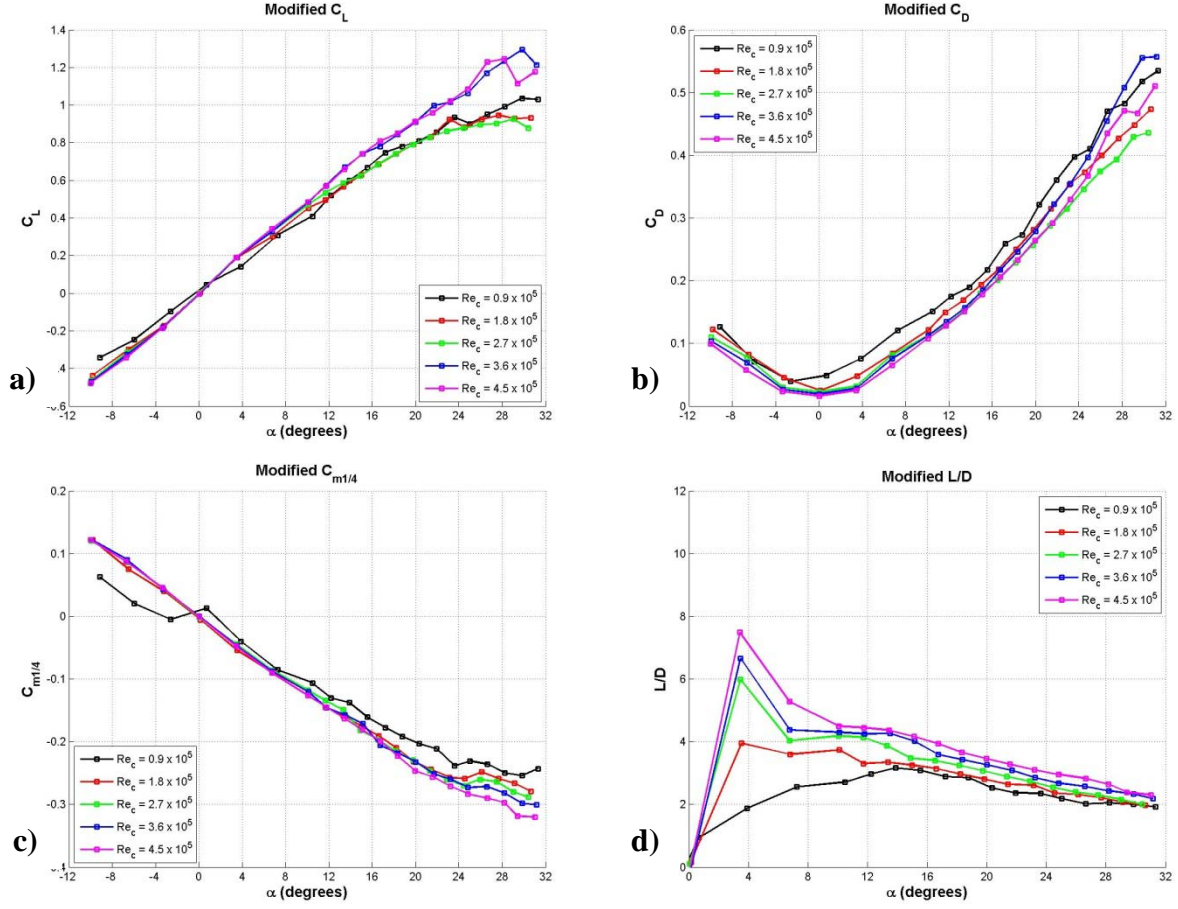
Figure 42. Effect of Reynolds number on the swept planform modified hydrofoil characteristics: a) lift coefficient, b) drag coefficient, c) pitching moment coefficient, d) *L/D* ratio.

Table 17: Hydrodynamic characteristics of swept planform modified hydrofoil.

	$Re_c = 9.0 \times 10^4$	$Re_c = 1.8 \times 10^5$	$Re_c = 2.7 \times 10^5$	$Re_c = 3.6 \times 10^5$	$Re_c = 4.5 \times 10^5$
$\frac{dC_L}{d\alpha}\,[\deg^{-1}]$	0.037	0.053	0.055	0.055	0.055
C_{Lmax}	1.04	0.95	0.93	1.29	1.25
$\alpha\ @\ C_{Lmax}\,[\deg]$	29.8	27.7	29.0	29.8	28.2
C_{Dmin}	0.04	0.03	0.02	0.02	0.02
L/D_{max}	3.2	3.9	6.0	6.7	7.5
$\alpha\ @\ L/D_{max}\,[\deg]$	13.9	3.5	3.5	3.5	3.4
$\alpha_{stall}\,[\deg]$	N/A	N/A	N/A	N/A	N/A
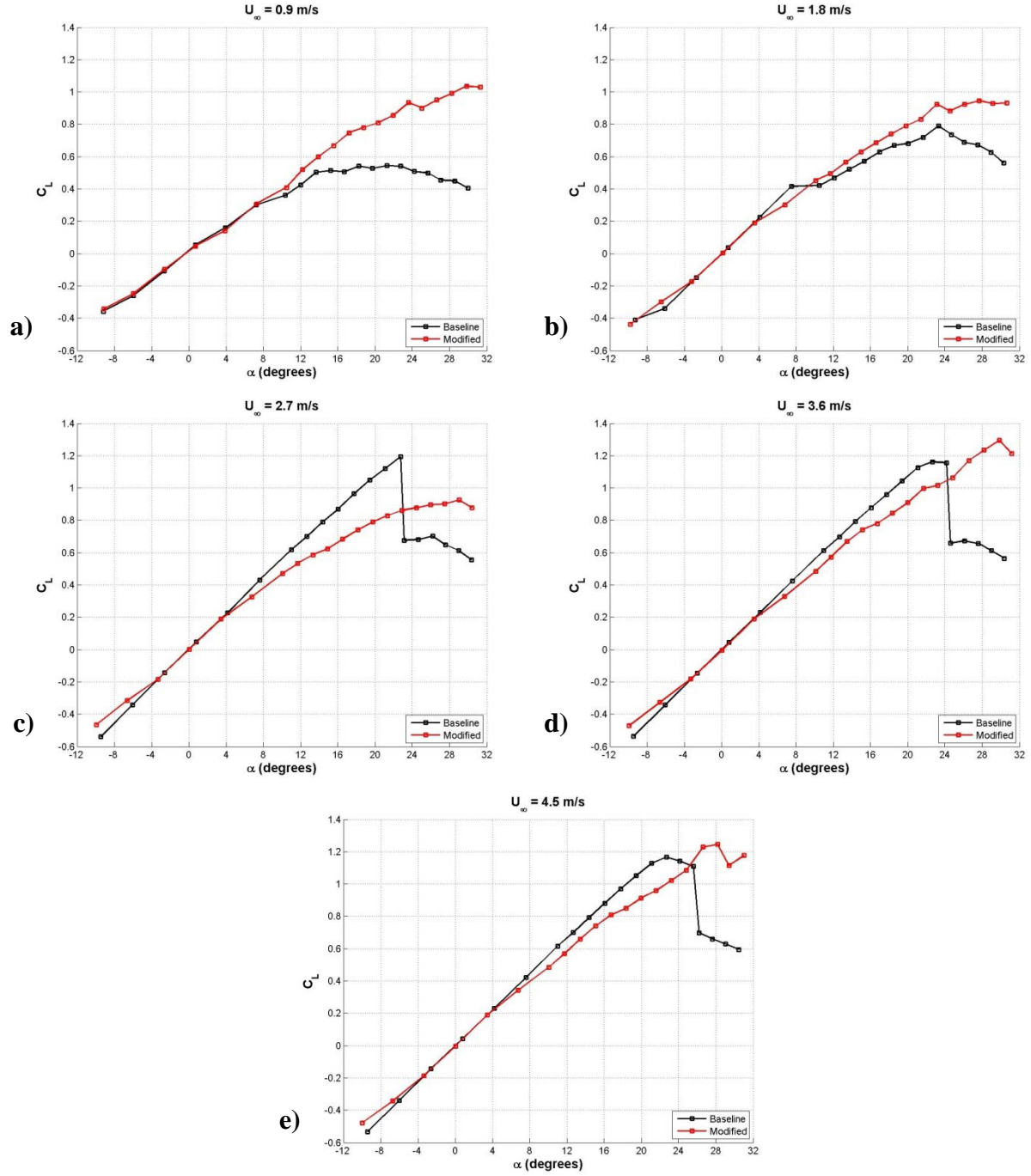
Figure 43. Lift coefficient of swept planform hydrofoils: a) $Re_c = 9.0 \times 10^4$, b) $Re_c = 1.8 \times 10^5$, c) $Re_c = 2.7 \times 10^5$, d) $Re_c = 3.6 \times 10^5$, e) $Re_c = 4.5 \times 10^5$.
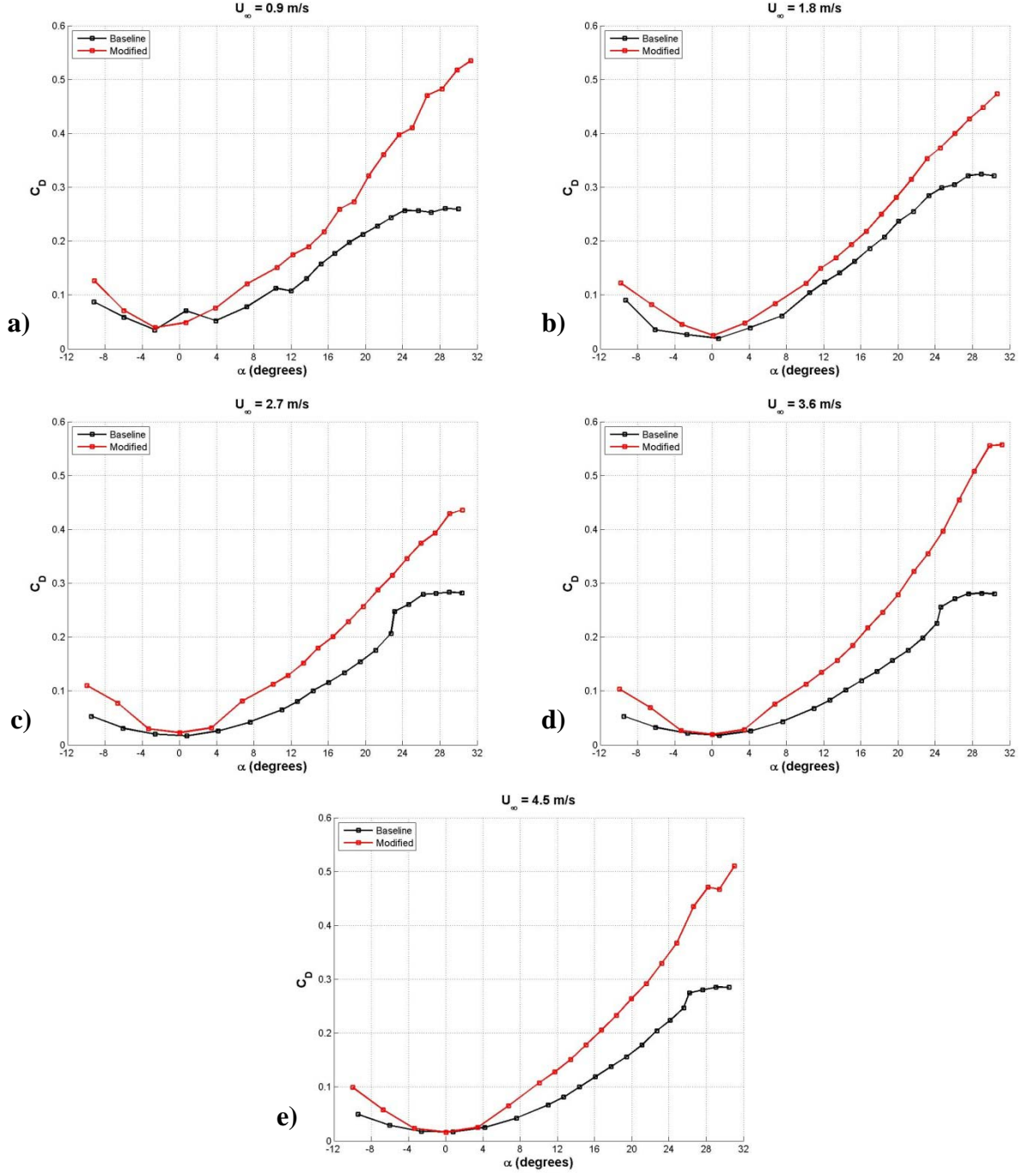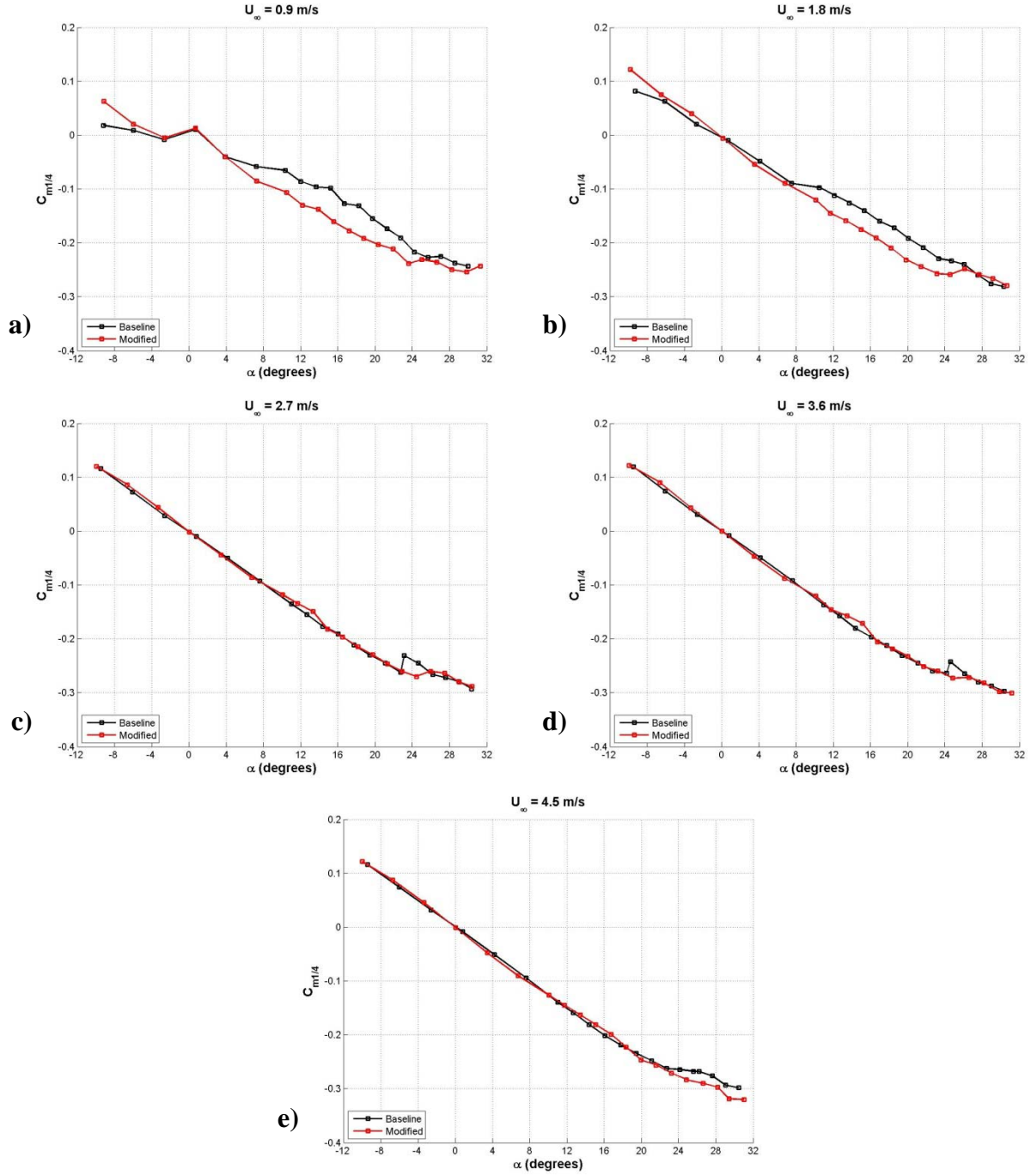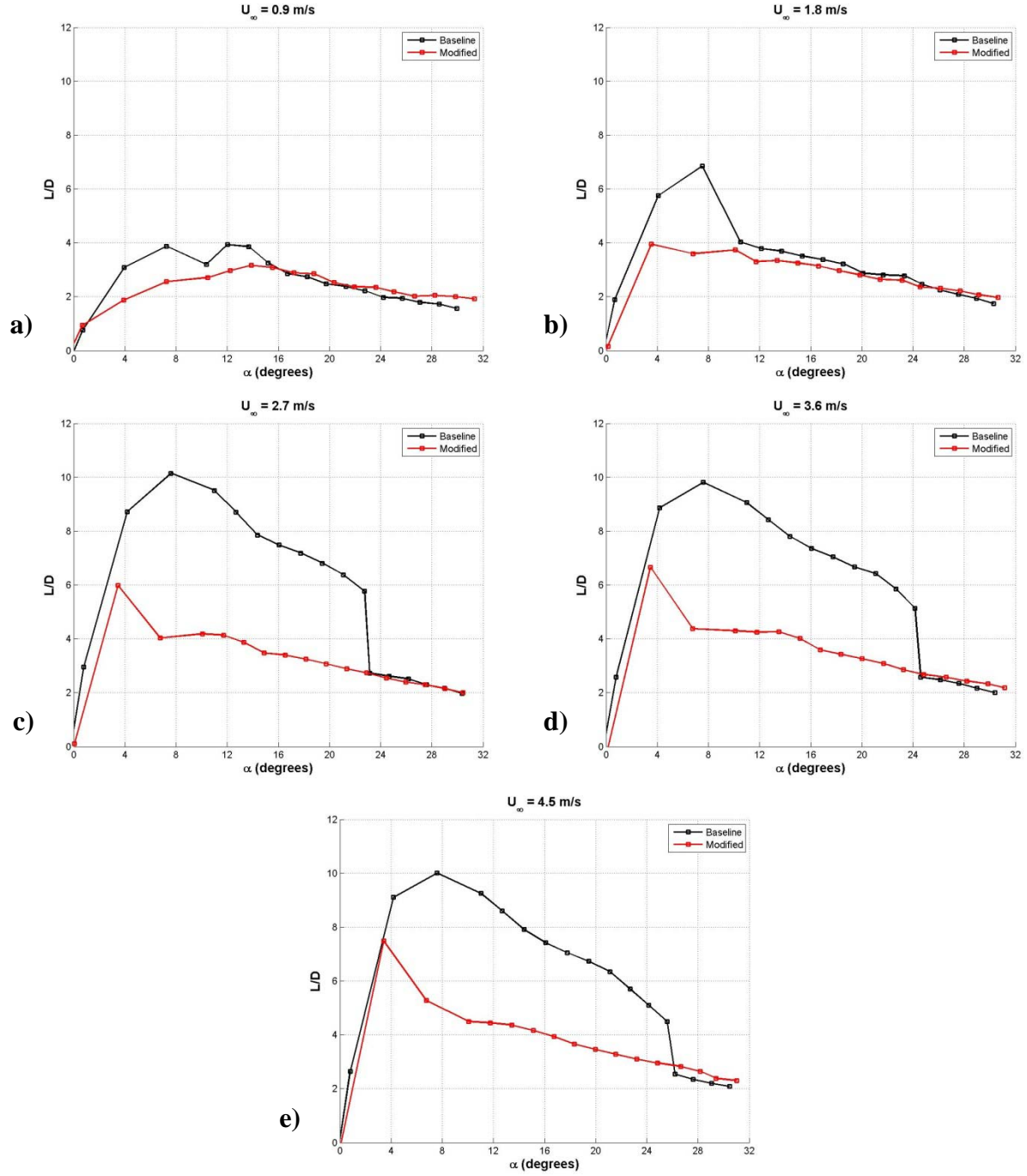
Figure 44. Drag coefficient of swept planform hydrofoils: a) $Re_c = 9.0 \times 10^4$, b) $Re_c = 1.8 \times 10^5$, c) $Re_c = 2.7 \times 10^5$, d) $Re_c = 3.6 \times 10^5$, e) $Re_c = 4.5 \times 10^5$.

Figure 45. Pitching moment coefficient of swept planform hydrofoils: a) $Re_c = 9.0 \times 10^4$, b) $Re_c = 1.8 \times 10^5$, c) $Re_c = 2.7 \times 10^5$, d) $Re_c = 3.6 \times 10^5$, e) $Re_c = 4.5 \times 10^5$.

Figure 46. Lift-to-drag ratio of swept planform hydrofoils: a) $Re_c = 9.0 \times 10^4$, b) $Re_c = 1.8 \times 10^5$, c) $Re_c = 2.7 \times 10^5$, d) $Re_c = 3.6 \times 10^5$, e) $Re_c = 4.5 \times 10^5$.

Flipper Planform Hydrofoils

Baseline model

The lift coefficient of the baseline flipper model is presented in Figure 47.a. For all freestream velocities examined, there is a linear increase in C_L at low angles of attack. With the exception of $U_\infty = 0.9$ and 1.8 m/s, C_L increases linearly with angle of attack until close to the stall angle. At freestream velocities of $2.7 \leq U_\infty \leq 4.5$ m/s, Reynolds number plays a minor role in establishing the lift characteristics of the baseline model, with C_L being nearly constant over a limited range of angles $12° \leq \alpha \leq 15°$ indicating flow separation. At angles of attack past $\alpha = 15°$, the model flipper stalls and C_L decreases dramatically. At the freestream velocity of $U_\infty = 1.8$ m/s, C_L continues to increase until the stall angle is reached and then the lift drops abruptly. The C_L at the freestream velocity of $U_\infty = 0.9$ m/s is different than the others as a result of low Reynolds number effects.

The drag coefficient of the baseline flipper model is shown in Figure 47.b. At low angle of attack C_D increases in a quadratic manner, as expected. A dramatic increase in C_D occurs at the stall angle, thereafter C_D increases at a lower rate at post-stall angles of attack. The minimum C_D decreases with Reynolds number for all cases; however, there is little change for the three highest freestream velocities. Examining the drag coefficient over the entire angle of attack range in Fig. 47b indicates that C_D becomes nearly independent of Reynolds number at freestream velocities greater than 2.7 m/s.

Whereas the pitching moment coefficient is largely unaffected by Reynolds number, the lift-to-drag ratio is highly dependent on the Reynolds number, see Figs. 47c and d. *L/D* increases significantly with every Reynolds number at pre-stall angles of attack. However, at post-stall angles of attack, *L/D* dependence on Reynolds number vanishes for values above $Re_c = 3.6 \times 10^5$. The effect of Reynolds number on $C_{M1/4}$ and *L/D* are presented in Figure 47.c and d, respectively. The major significant hydrodynamic characteristics of the baseline flipper model are summarized in Table 18.
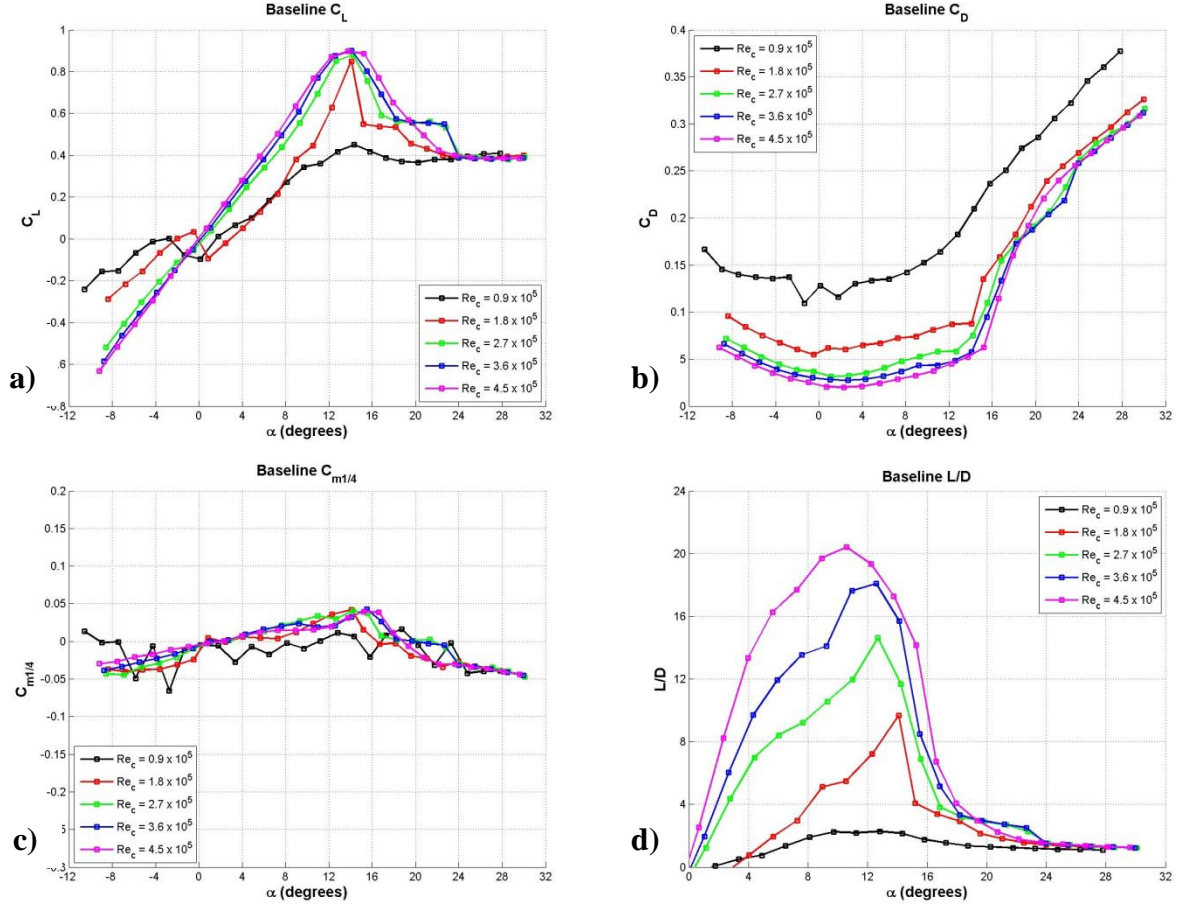
Figure 47. Effect of Reynolds number on the baseline flipper model characteristics: a) lift coefficient, b) drag coefficient, c) pitching moment coefficient, d) *L/D* ratio.

Table 18: Hydrodynamic characteristics of baseline flipper model.

	$Re_c = 9.0 \times 10^4$	$Re_c = 1.8 \times 10^5$	$Re_c = 2.7 \times 10^5$	$Re_c = 3.6 \times 10^5$	$Re_c = 4.5 \times 10^5$
$\frac{dC_L}{d\alpha}$ [deg^{-1}]	0.044	0.049	0.059	0.063	0.070
C_{Lmax}	0.45	0.85	0.88	0.90	0.90
α @ C_{Lmax} [deg]	14.4	14.1	14.2	14.1	13.8
C_{Dmin}	0.11	0.06	0.03	0.03	0.02
L/D_{max}	2.3	9.7	14.6	18.1	20.4
α @ L/D_{max} [deg]	12.8	14.1	12.7	12.6	10.6
α_{stall} [deg]	N/A	14.1	14.2	14.1	15.3

Modified flipper model

The effect of Reynolds number on the lift coefficient of the modified hydrofoils can be seen in Figure 48.a. The lift coefficient corresponding to freestream velocities of $U_\infty = 2.7$ m/s or greater, corresponding to $Re_c \geq 2.7 \times 10^5$ is nearly independent of Reynolds number. Below this Reynolds number, the lift coefficient for the modified flipper model becomes Reynolds number dependent. Low Reynolds number effects are particularly evident at the lowest freestream velocity of $U_\infty = 0.9$ m/s and $Re_c = 9.0 \times 10^4$. The dependence of drag coefficient for the modified flipper model on the Reynolds number is shown in Figure 48.b. With the exception of the freestream velocity of $U_\infty = 0.9$ m/s and at angles of attack below $\alpha = 15°$, C_D is nearly unaffected by the Reynolds number. Furthermore, discounting the lowest freestream velocity of $U_\infty = 0.9$ m/s, the effect of Reynolds number on the pitching moment coefficient $C_{M1/4}$ and the lift-to-drag ratio, shown in Figure 48.c and d respectively, are very similar to those observed for the baseline case. Several important hydrodynamic characteristics of the modified flipper model are listed in Table 19.

The effects of leading edge protuberances on the lift coefficient of flipper models resembling the morphology of the humpback whale flipper are shown in Figure 49. At the lowest freestream velocity examined, $U_\infty = 0.9$ m/s, the lift coefficient of the modified hydrofoil is nearly equal to or greater than the baseline hydrofoil for all angles of attack, to within experimental uncertainty. At freestream velocities equal to or less than 1.8 m/s, low Reynolds number effects are prominent, whereas at velocities greater than 1.8 m/s both the modified and baseline flipper models show similar lift characteristics at angles of attack below the stall angle. The lift coefficient of the modified hydrofoil increases at the same rate as the baseline hydrofoil until just prior to the baseline stall angle, at which point C_L of the modified flipper model is slightly less than that of the baseline. The stall angle is increased by $1° - 3°$ depending on the freestream velocity with a maximum increase of nearly 50% in C_L at $\alpha \approx 18°$ over the baseline hydrofoil at a freestream velocity of $U_\infty = 3.6$ m/s. At $U_\infty = 4.5$ m/s the modified hydrofoil shows an increase in maximum lift of $\approx 53\%$ over the baseline. At the highest angles of attack examined, the modified flipper model and the baseline perform similarly, to within the experimental uncertainties.

The drag coefficient of flipper models with and without leading edge protuberances are compared in Figure 50. At a freestream velocity of $U_\infty = 0.9$ m/s, C_D of the modified hydrofoil is lower than the baseline flipper model, the former has nearly 100% less drag than the baseline

hydrofoil, a consequence of low Reynolds number. At freestream velocities in the range of $0.9 \leq U_\infty \leq 2.7$ m/s, the modified hydrofoil produces less drag in the pre-stall regime of the baseline hydrofoil at angles of attack ranging from $1° \lesssim \alpha \leq 12°$ while at angles of attack greater than $\alpha = 12°$ the drag coefficient of the baseline and modified flipper models are very similar. For freestream velocities of 3.6 and 4.5 m/s, the modified hydrofoil shows slightly higher drag that the baseline hydrofoil in the pre-stall regime over a range of angles of attack $10° \lesssim \alpha \leq 15°$, and nearly equivalent C_D for all other angles of attack examined. At the highest freestream velocity of $U_\infty = 4.5$ m/s, Figure 50.e shows a minute 4% drag reduction over a small range of angles $15° \leq \alpha \leq 22°$.

At the freestream velocity of $U_\infty = 0.9$ m/s, pitching moment coefficient for the modified hydrofoil is significantly different from the baseline case, see Fig. 51. This is likely due to the limitations of the measurement technique as well as low Reynolds number effects. With the exception of the lowest freestream velocity tested, $C_{M1/4}$ of the baseline and modified cases are very similar.

The lift-to-drag ratio for the flipper models with and without the leading edge protuberances is shown in Figure 52. At a freestream velocity of $U_\infty = 0.9$ m/s, L/D is either greater than or equal (to within experimental uncertainty) to the baseline case. However, for freestream velocities ranging from $1.8 \leq U_\infty \leq 3.6$ m/s, the modified case has a greater L/D at low angle of attack as well as over a limited range of angles in the post-stall regime of the baseline hydrofoil. For the highest freestream velocity of $U_\infty = 4.5$ m/s, an increased lift-to-drag ratio is only seen over a range of angles of $16° \lesssim \alpha \leq 22°$. Throughout the remaining angles of attack, L/D for the modified flipper model is similar to or less than the baseline model.
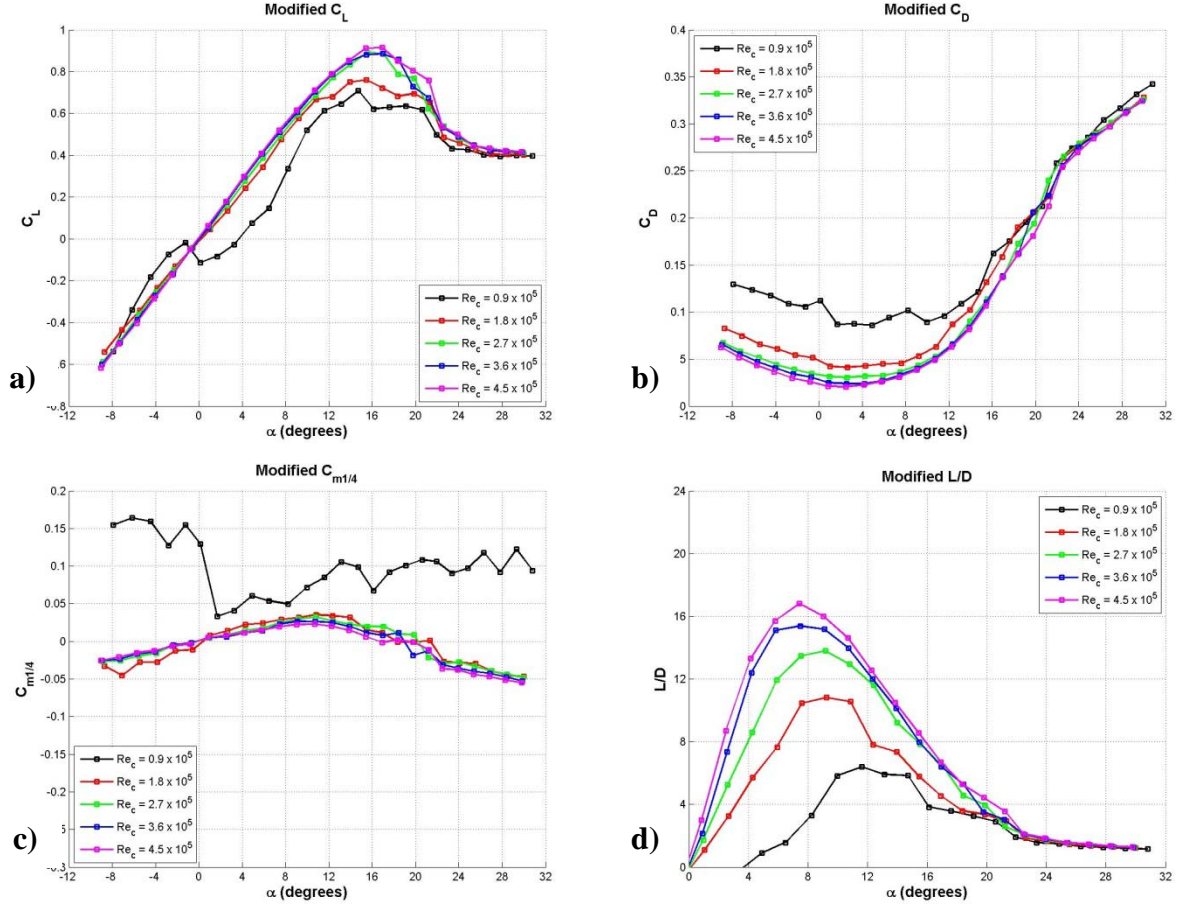
Figure 48. Effect of Reynolds number on the modified flipper model characteristics: a) lift coefficient, b) drag coefficient, c) pitching moment coefficient, d) *L/D* ratio.

Table 19: Hydrodynamic characteristics of the modified flipper model.

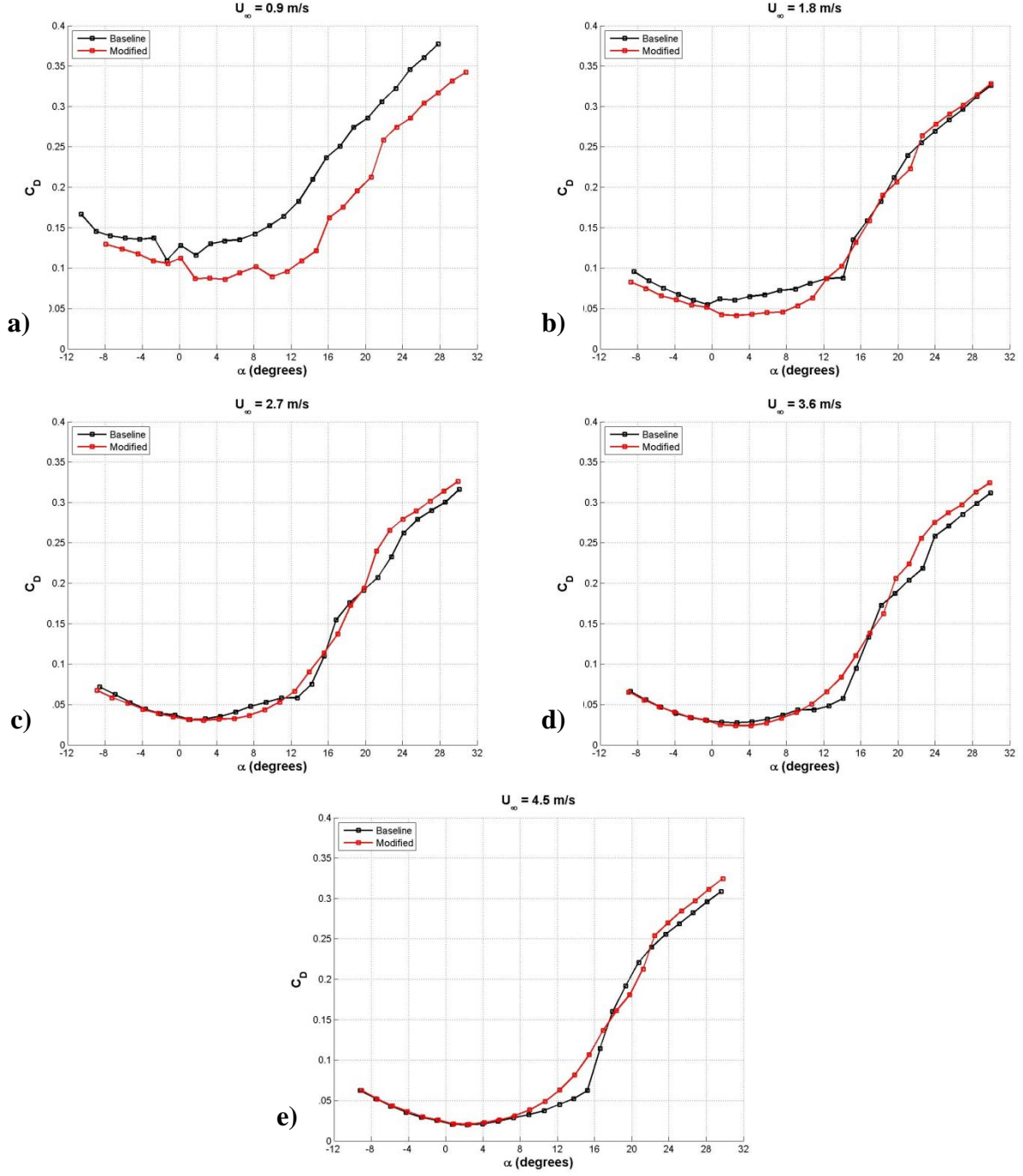|	$Re_c = 9.0 \times 10^4$	$Re_c = 1.8 \times 10^5$	$Re_c = 2.7 \times 10^5$	$Re_c = 3.6 \times 10^5$	$Re_c = 4.5 \times 10^5$
$\frac{dC_L}{d\alpha}[\text{deg}^{-1}]$	0.051	0.064	0.066	0.067	0.070
C_{Lmax}	0.71	0.76	0.89	0.89	0.91
$\alpha @ C_{Lmax}$ [deg]	14.7	15.5	15.5	17.0	16.9
C_{Dmin}	0.09	0.04	0.03	0.02	0.02
L/D_{max}	6.39	10.82	13.8	15.39	16.8
$\alpha @ L/D_{max}$ [deg]	11.6	9.2	9.2	7.5	7.4
α_{stall} [deg]	14.7	15.5	17.0	18.4	21.2
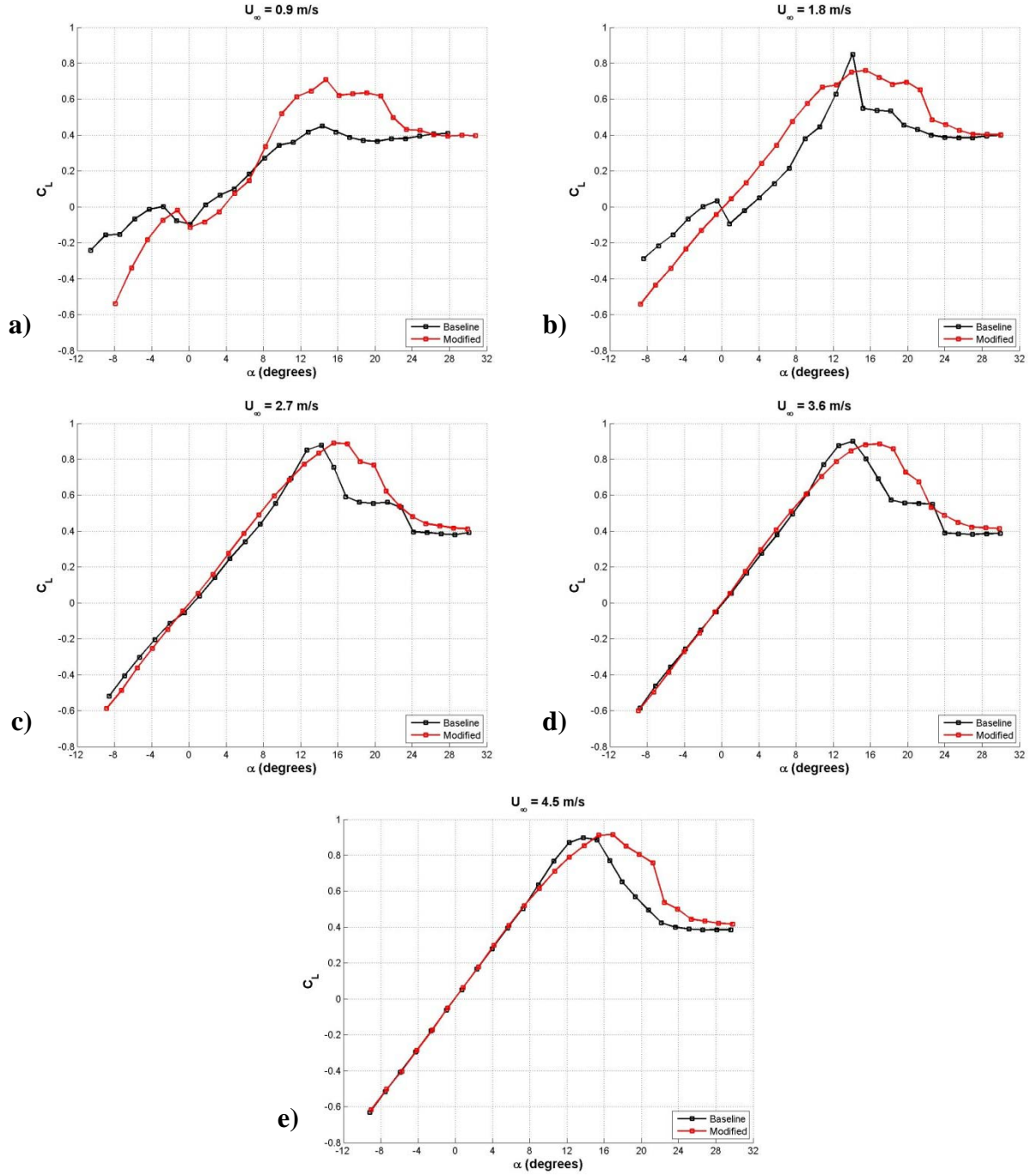
Figure 49. Lift coefficient of flipper model hydrofoils: a) $Re_c = 9.0 \times 10^4$, b) $Re_c = 1.8 \times 10^5$, c) $Re_c = 2.7 \times 10^5$, d) $Re_c = 3.6 \times 10^5$, e) $Re_c = 4.5 \times 10^5$.
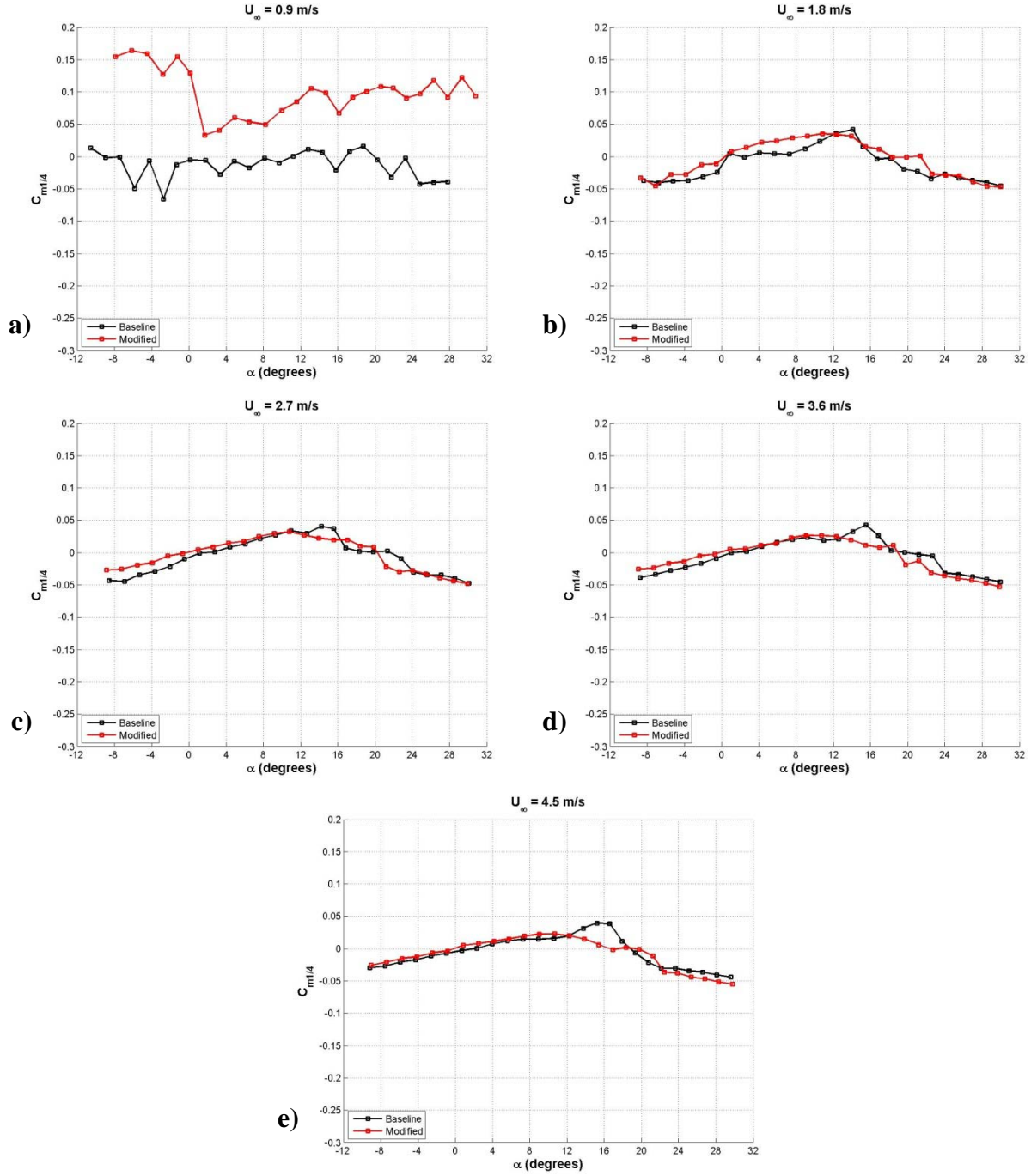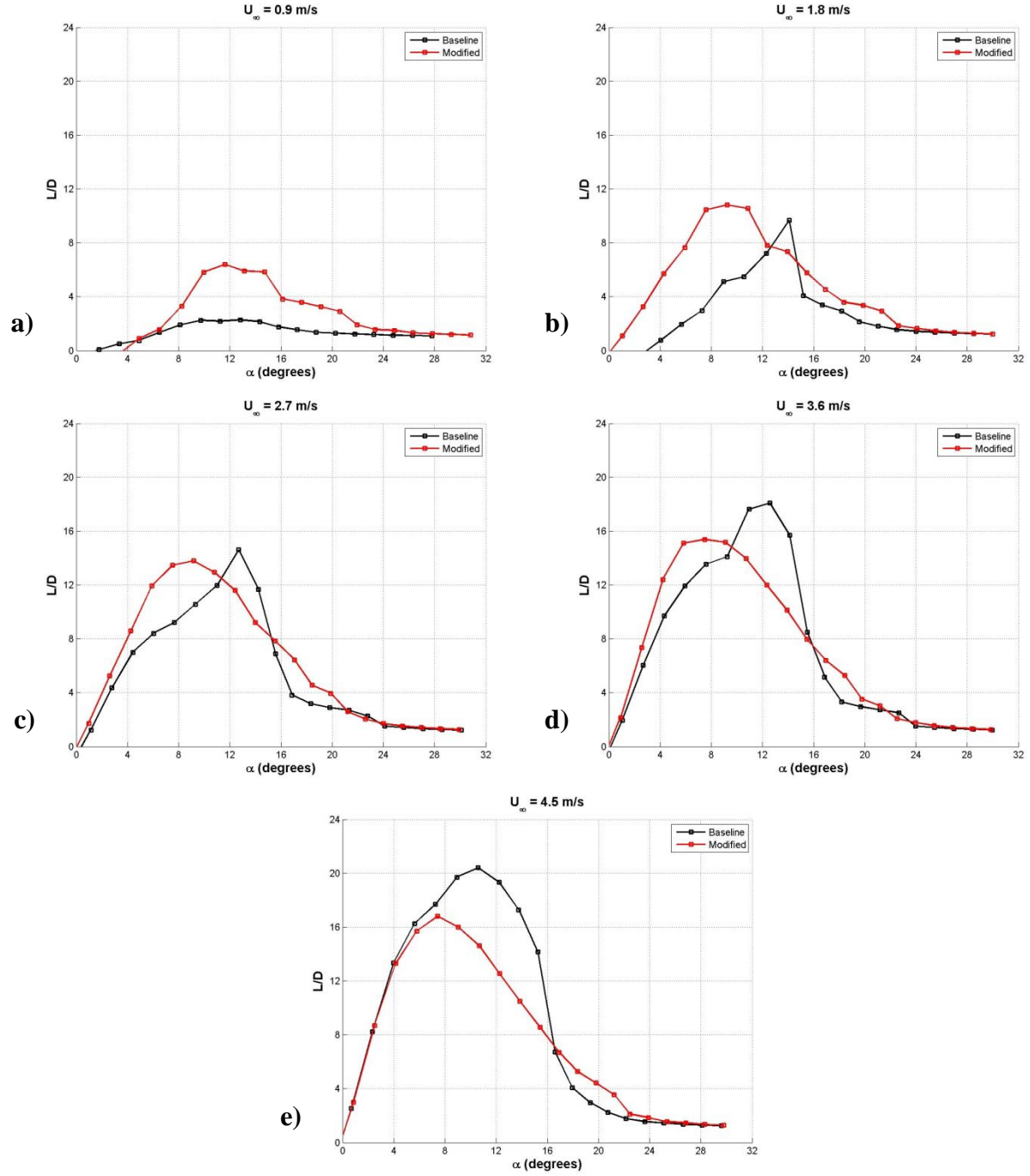
Figure 50. Drag coefficient of flipper model hydrofoils: a) $Re_c = 9.0 \times 10^4$, b) $Re_c = 1.8 \times 10^5$, c) $Re_c = 2.7 \times 10^5$, d) $Re_c = 3.6 \times 10^5$, e) $Re_c = 4.5 \times 10^5$.

Figure 51. Pitching moment coefficient of flipper model hydrofoils: a) $Re_c = 9.0 \times 10^4$, b) $Re_c = 1.8 \times 10^5$, c) $Re_c = 2.7 \times 10^5$, d) $Re_c = 3.6 \times 10^5$, e) $Re_c = 4.5 \times 10^5$.

Figure 52. Lift-to-drag ratio of flipper model hydrofoils: a) $Re_c = 9.0 \times 10^4$, b) $Re_c = 1.8 \times 10^5$, c) $Re_c = 2.7 \times 10^5$, d) $Re_c = 3.6 \times 10^5$, e) $Re_c = 4.5 \times 10^5$.

Full-Span Flow Field Measurements

To examine the flow features in transverse planes and to extract the streamwise vorticity field of the full-span leading edge modified hydrofoil, a set of 2D Particle Image Velocimetry (PIV) measurements was carried on the 305-mm 4L hydrofoil. The flow field measurements on several planes over the suction side of the 4L hydrofoil and at eight angles of attack were conducted at a low speed of $U_\infty = 0.15$ m/s; higher speed measurements at $U_\infty = 1.8$ m/s and 4.5 m/s were also performed at a single plane on this hydrofoil for comparison to the low speed case.

Low-speed measurements

The effect of angle of attack on the development of the streamwise vorticity field, ω, of the 4L hydrofoil at several spatial locations of $x/c = 0$, 0.12, 0.25, and 0.36 are shown in Figs. 53 - 56. These locations correspond to the mean leading edge, bottom of the trough, quarter-chord, and the point where the profile merges into the baseline, respectively. The planes are perpendicular to the freestream and are located on the suction side of the hydrofoil looking upstream. Therefore, the direction of positive vorticity is perpendicular outward from the image plane, while negative vorticity is perpendicular inward. The diagram of the sinusoidal leading edge to the left of the images is to be used as a reference for determining the position of the vortices relative to the protuberances and is not drawn to mimic the proper direction of the leading edge. Streamwise vorticity stemming from protuberance shoulders can be seen as counter-rotating vortex pairs even though the contours are not circular. Vorticity on the uppermost and lowermost inflection points in Figs. 53 - 56 is not seen in the vorticity contours due to experimental limitations on the edges of the area of interest.

Generally, vorticity in the core of the vortices tends to increase with angle of attack due to spanwise pressure gradients generated by the difference in leading edge radius from peak to trough. At spatial locations ranging from $0\,c$ to $0.12\,c$ the shape and size of the spanwise distribution of vortices tends to remain consistent and symmetric as the angle of attack is increased. However, at spatial locations greater than $0.12\,c$, the symmetry breaks down. As the strength of vortices increases, interactions among neighboring vortices generate asymmetry in the vorticity distribution. Streamwise vorticity on modified hydrofoils is affected by the spatial location. As the vortices move along the hydrofoil, the proximity of both the hydrofoil surface as well as the neighboring vortices induce spanwise velocities. The induced spanwise velocity causes neighboring vortices to interact, resulting in asymmetry in the vorticity distribution. The

height of the vortices above the hydrofoil surface changes with angle of attack as well, with vortices showing signs of lifting off above the surface at higher angles. At spatial locations greater than 0.12 c, the distribution of vorticity in neighboring vortices changes in extent and shape. Vortex interactions lead to the stretching and dissipation of vortices.

The direction of vorticity with respect to the leading edge protuberances on the hydrofoil corresponds to that of a delta wing. On a delta wing, positive vorticity develops on the starboard side while negative vorticity develops on the port side. The vortices on a delta wing are capable of increasing stall angle of attack and softening stall, both of which are similar characteristics to those seen on hydrofoils with protuberances. Therefore, the protuberances can be considered somewhat analogous to a series of spanwise delta wings along the leading edge of the hydrofoil.

High-speed measurements

The streamwise vorticity distribution at chordwise location of $x/c = 0.36\ c$ at freestream velocities of $U_\infty = 1.8$ and 4.5 m/s is compared with the same at the 0.15 m/s velocity in Figure . As expected, the values of vorticity in the core of vortices at the two higher velocities differ significantly from the lower velocity case; however, the overall trend of asymmetric vortices developing as a function of attack angle does not. Vorticity once again increases with the angle of attack. As was observed at the lower velocity, the vortex distribution becomes asymmetric at the higher angles of attack. This is primarily due to interactions between neighboring vortices. In all cases tested, depending on the spanwise location and angle of attack, vortex interactions may lead to neighboring vortices moving toward one another, creating a convergence pattern, or away from one another, creating a divergence pattern. A merging of neighboring vortices leads to the stretching of vorticity in the spanwise direction as well as lifting-off from the hydrofoil surface.

The pattern of vorticity in the higher freestream velocity data differs, somewhat, from that in the low-speed case. At first glance, it appears as though the pattern changes with the freestream velocity. On the contrary, the pattern remains the same; however, the area of investigation on the hydrofoil surface is slightly different between the high- and low-speed cases. The pattern of vorticity distribution is bi-periodic, and therefore, since the area of investigation considered only contains two periods at the leading edge, there is visually a difference in the pattern. Had the lower-speed data been shifted by one period, the patterns would like much closer. Of course, vorticity diffuses more at the lower-speed. Given the overall patterns, it was determined that the streamwise vorticity distribution is only a weak function of freestream velocity.
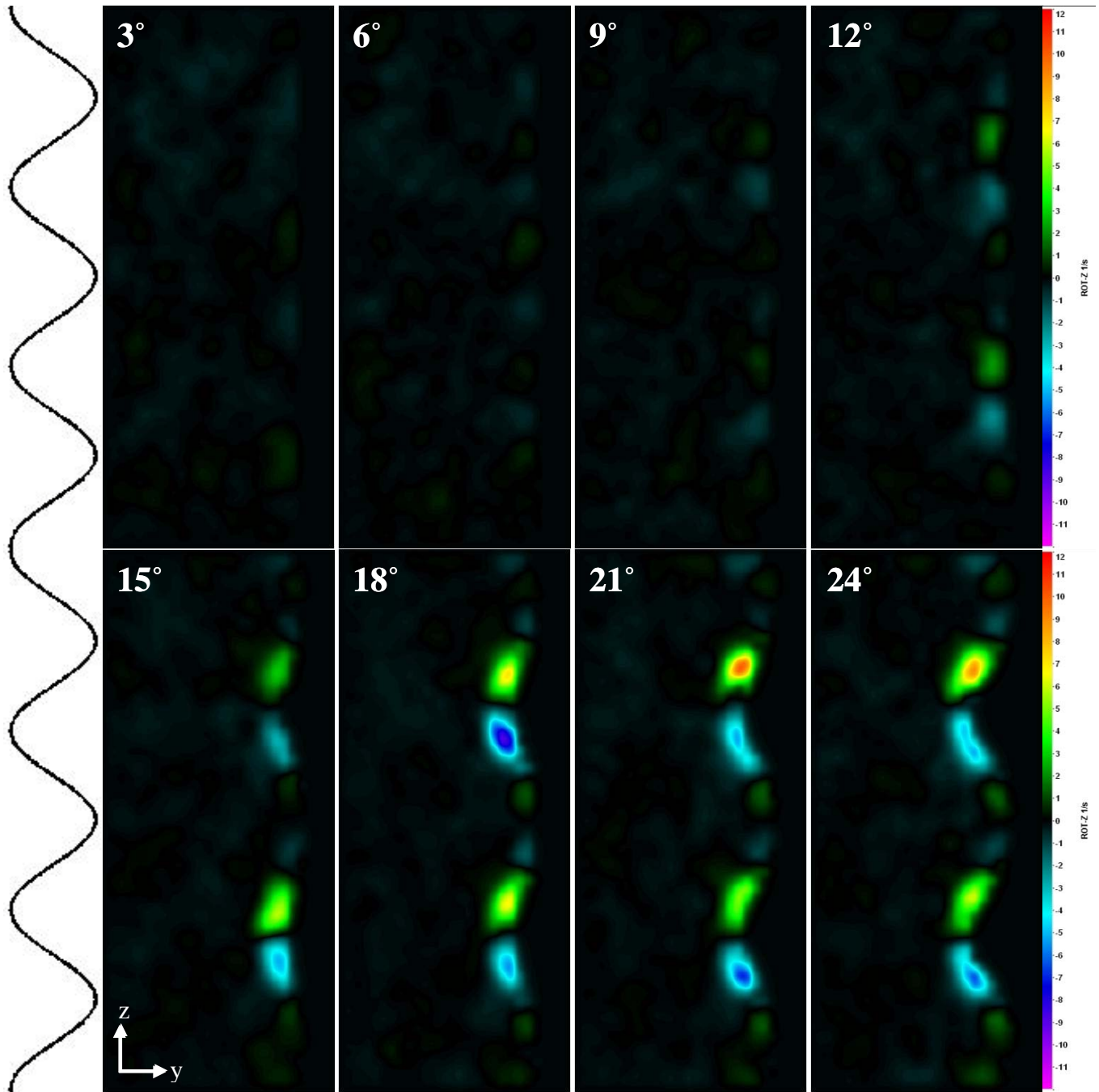
Figure 53. Streamwise vorticity, ω, contours on the 4L hydrofoil as a function of angle of attack at the chordwise location of 0 c corresponding to the mean leading edge location.
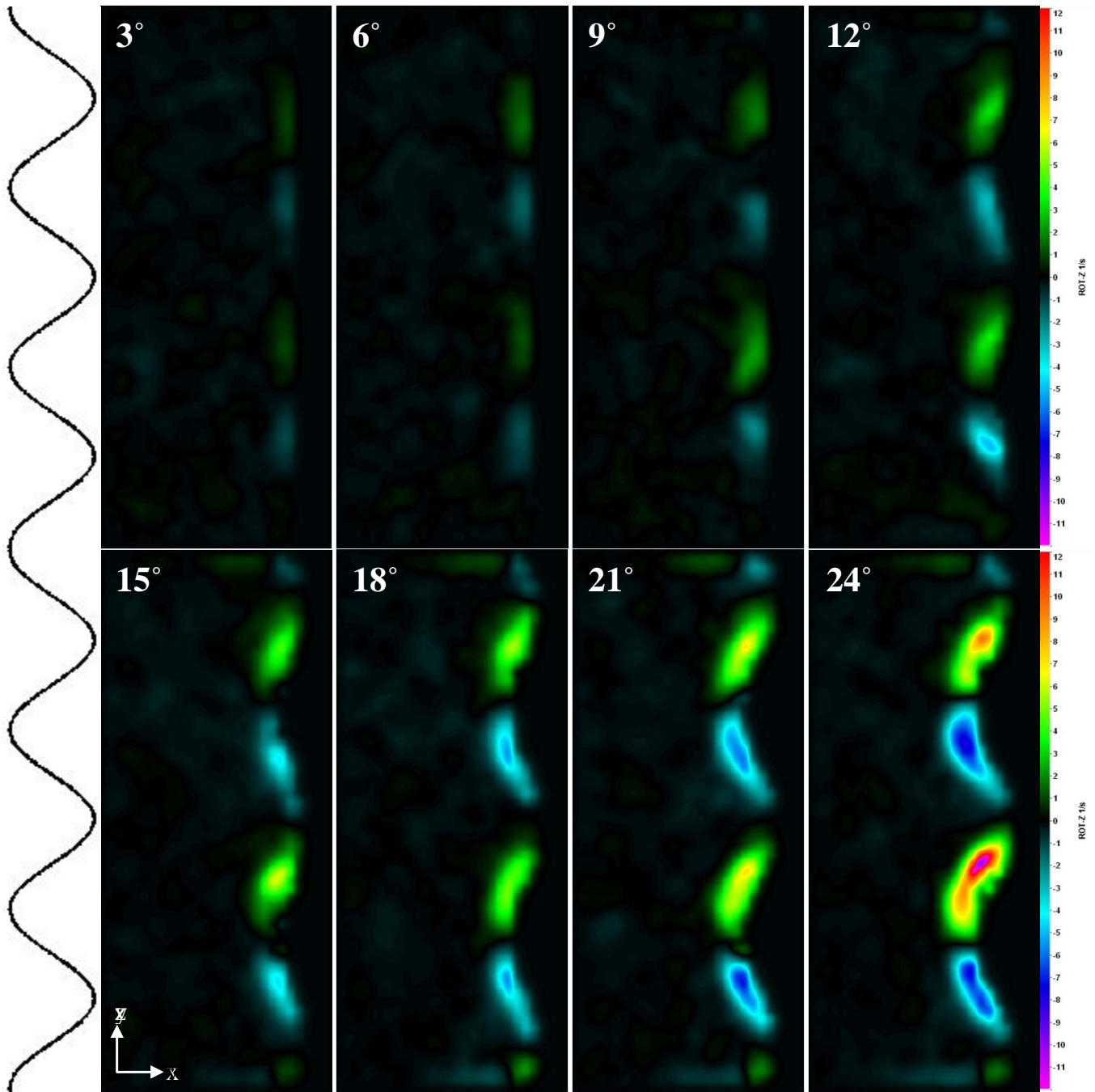
Figure 54. Streamwise vorticity, ω, contours on the 4L hydrofoil as a function of angle of attack at a chordwise location of 0.12 c downstream of the mean leading edge.
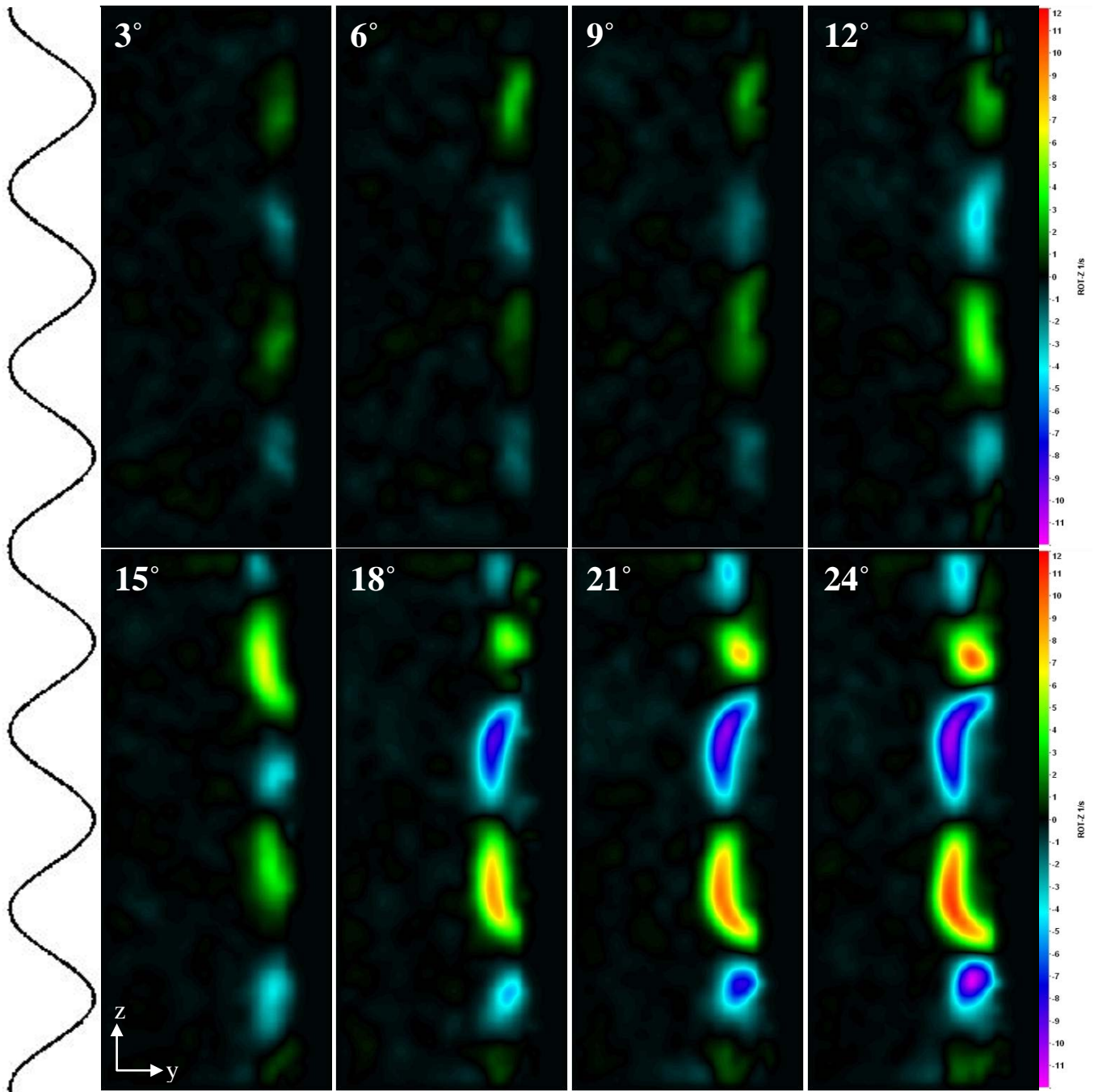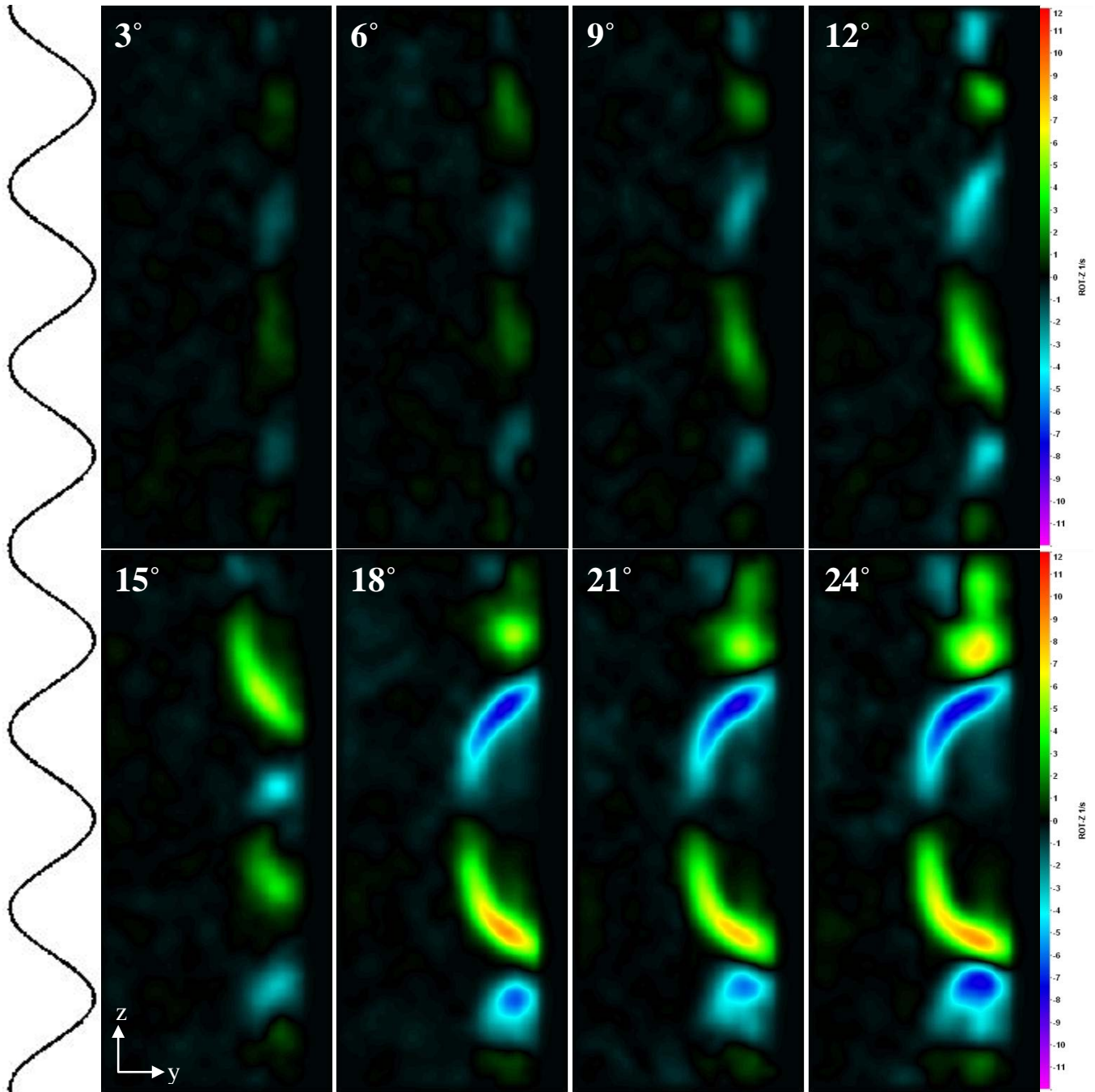
Figure 55. Streamwise vorticity, ω, contours on the 4L hydrofoil as a function of angle of attack at the chordwise location of 0.25 c downstream of the mean leading edge.

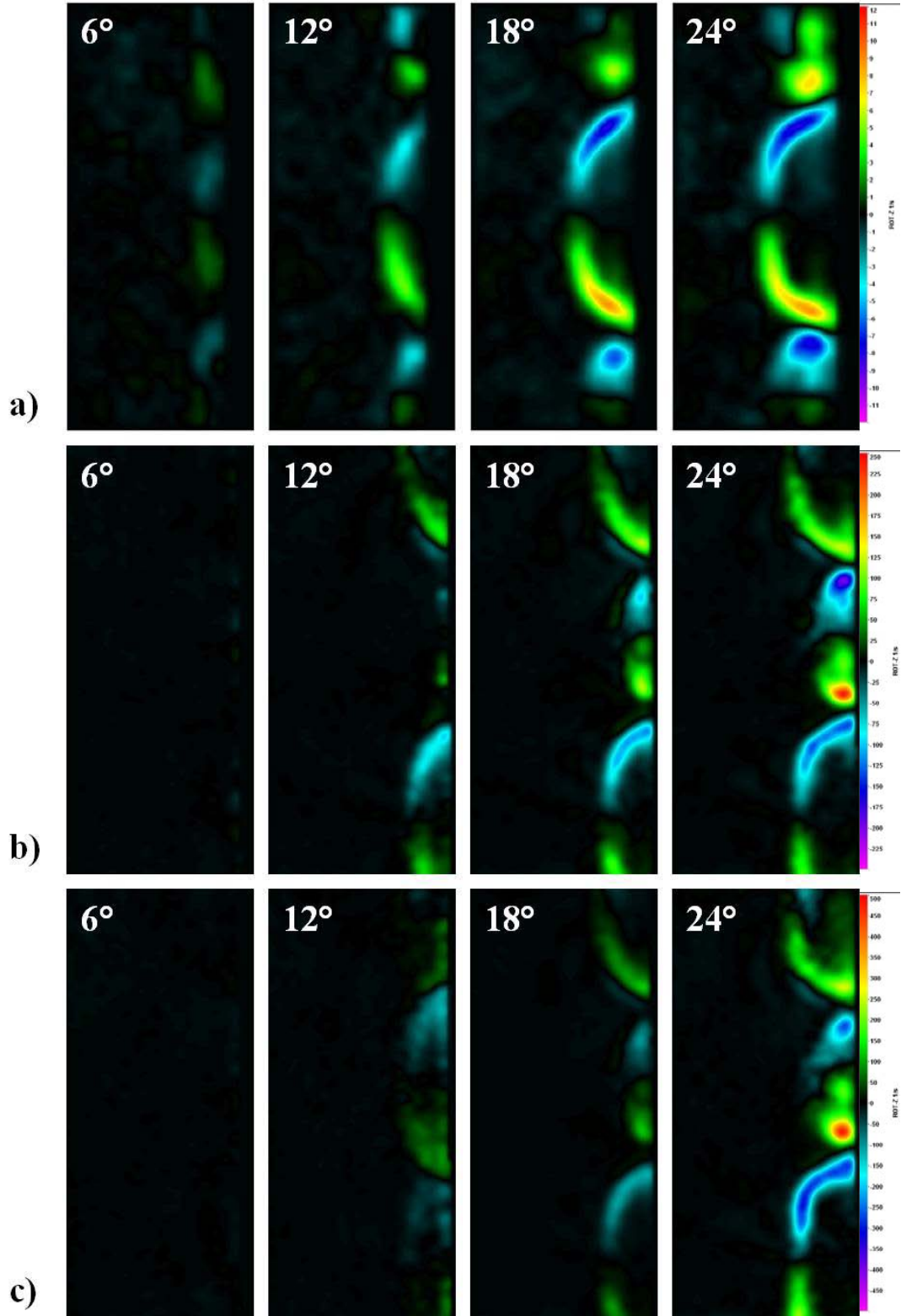Figure 56. Streamwise vorticity, ω, contours on the 4L hydrofoil as a function of angle of attack at the chordwise location of 0.36 c downstream of the mean leading edge.

Figure 57. Streamwise vorticity, ω, contours on the 4L hydrofoil as a function of angle of attack at the spatial location of 0.36 c. a) $U_\infty = 0.15$ m/s, b) $U_\infty = 1.80$ m/s, c) $U_\infty = 4.50$ m/s.

Vortex circulation

The circulation, Γ, of the vortices in Figs. 53 - 57 were calculated as a function of angle of attack and chordwise location. The vortices examined in the PIV experiments are numbered sequentially (1, 2, 3, and 4) according to their position as in Fig. 58. Figures 59 - 62 present the effect of angle of attack on the circulation of the vortices on the 4L full-span hydrofoil at spatial locations of $0 \leq x/c \leq 0.36$, with $0\ c$ referring to the mean leading position which is aligned with the protuberance inflection points, and $0.36\ c$ referring to the chordwise location aft of which the baseline and modified profiles are identical. The data presented in these plots refer only to the freestream velocity of $U_\infty = 0.15$ m/s. Figures 63 and 64, on the other hand, show the variation of circulation with the angle of attack at the two higher freestream velocities of $U_\infty = 1.8$ and 4.5 m/s, respectively. The data in these plots can be directly compared with those in Fig. 62 for the lower velocity case so that dependence of circulation values on the Reynolds number could be assessed.

Figure 59 shows that scaled circulation increases monotonically for all observable vortices at the spatial location of $x = 0\ c$. This implies that the vortex strength increases with the angle of attack and there are minimal vortex interactions at this spatial location. At the next chordwise location of $x = 0.12\ c$, shown in Fig. 60, the monotonic increase in circulation with angle of attack is still apparent; however, the maximum values for scaled Γ have increased significantly. This is due to the large leading edge radius in the troughs of the protuberances. Because the trough of the protuberances is the spanwise location at which the leading edge radius in greatest, it is this location that will have the largest spanwise pressure gradient, which in turn will produce the strongest vorticity. Scaled circulation at the quarter-chord location, $x = 0.25\ c$, is presented in Fig. 61. At this location, signs of vortex interactions begin to appear. At low angles of attack, scaled circulation has similar values for all of the vortices examined; however as the angle of attack is increased, asymmetry appears where vortices 2 and 3 have similar circulation values while the values for vortices 1 and 4 differ significantly in comparison. Also, at intermediate angles, a transition region can be seen in which the circulation of certain vortices changes dramatically over a small range of angles. The reason for the dramatic change in circulation lies in the development of an asymmetric vorticity distribution along the leading edge. At low angles, vorticity is for the most part distributed symmetrically among the vortices. On the other hand, at high angles vorticity distribution is highly asymmetric. At the intermediate angles of attack,

vortex merging results in one pair of vortices to gain strength while the neighboring ones lose strength. Similar trends can be observed at the chordwise location of $x = 0.36\,c$ in Fig. 62.

Scaled circulation dependence on the angle of attack for the two freestream velocities of 1.8 and 4.5 m/s at the chordwise location of $x = 0.36\,c$ is presented in Figs. 63 and 64. Comparing the data in these two plots with the ones in Fig. 62 reveals that Reynolds number has only a minor effect on the general trend of circulation growth with angle of attack. Uniform values of circulation as a result of symmetry in vorticity distribution appear at the lower angles of attack while at intermediate angles asymmetry of the vorticity distribution leads to the variations in circulation values. A clear separation of circulation values for vortices 2 and 3 compared to vortices 1 and 4 emerges at the higher angles. Also, Reynolds number does not affect the values of normalized circulation greatly, with the averaged circulation of vortices 1 - 4 all being on the same order, see Figure , further supporting the notion that Reynolds number plays only a minor role in establishing the vortex patterns on the modified hydrofoils.

The circulation data presented in Figs. 59 – 63 are replotted in Figs. 65 – 68 to present the development of scaled circulation with chordwise location at specific angles of attack. Figure 65 shows that scaled circulation is nearly the same, to within experimental uncertainty, for all four vortices examined at $\alpha = 6°$ over the range of chordwise locations tested. This is due to the lack of vortex interactions at low angles of attack. Streamwise vorticity and circulation remain weak at the lower angles of attack reducing the likelihood of vortex interactions. As the angle of attack is increased to $\alpha = 12°$, see Fig. 66, signs of vortex interaction begin to appear. This is especially evident at locations greater than $x = 0.12\,c$ where the circulation of vortices 1 and 4 differing significantly from vortices 2 and 3. This trend is also evident at angles of attack of 18° and 24°, shown in Figs. 67 and 68, with a maximum scaled circulation Γ being reached at the chordwise location of $x = 0.12\,c$. Circulation appears to get reduced as the vortices develop further along the hydrofoil as a result of vorticity cancelation due to vortex interactions. As the counter-rotating vortices interact, opposite signed vorticity cancel each other and produce a reduction in circulation of some vortices.
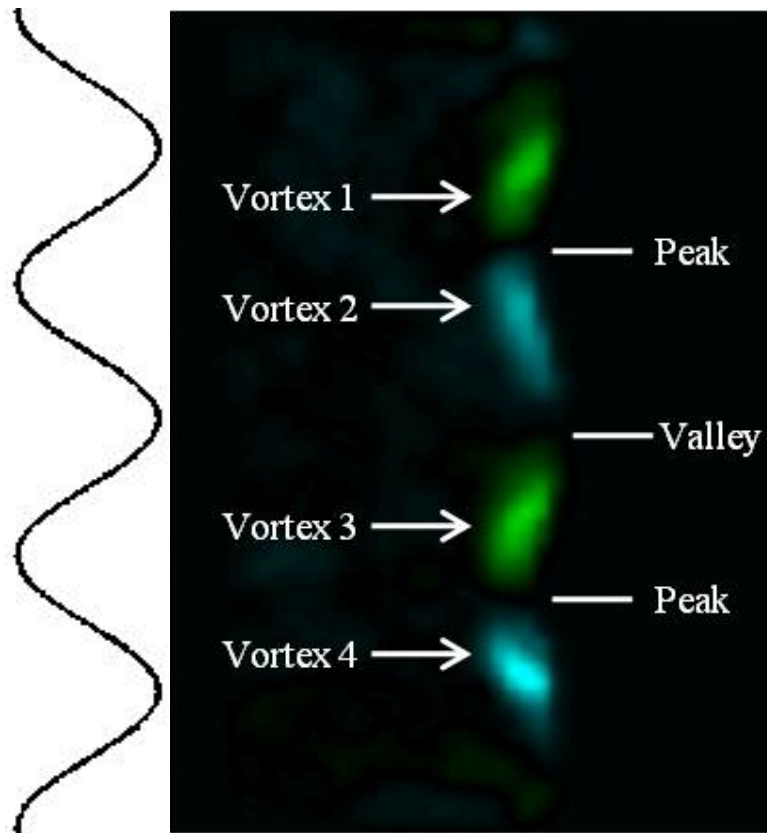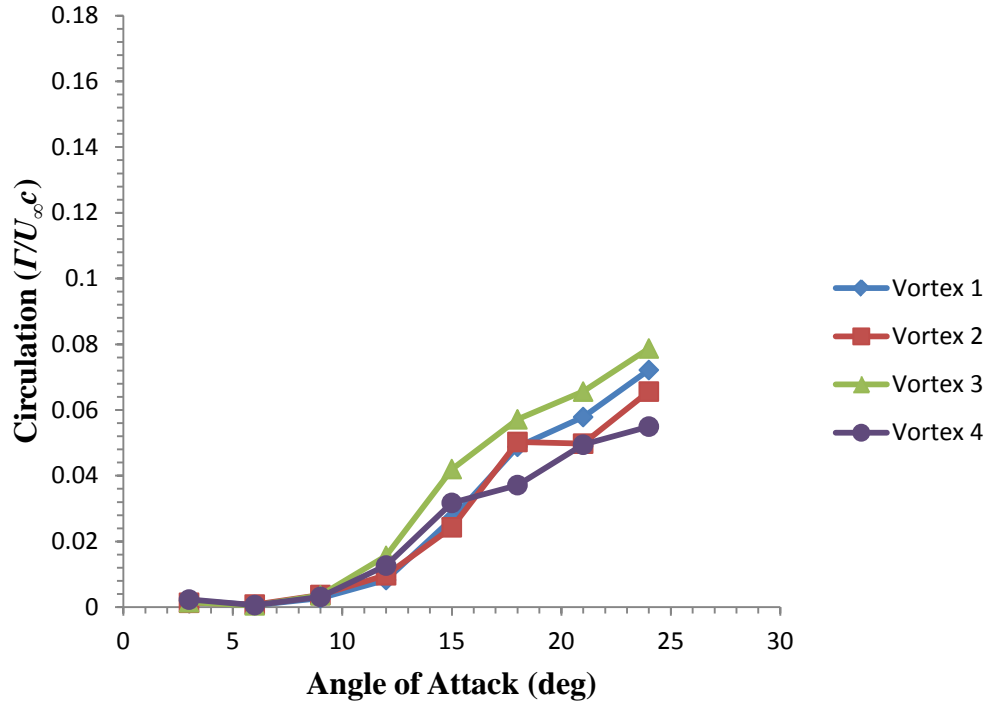
Figure 58. Vortex nomenclature.

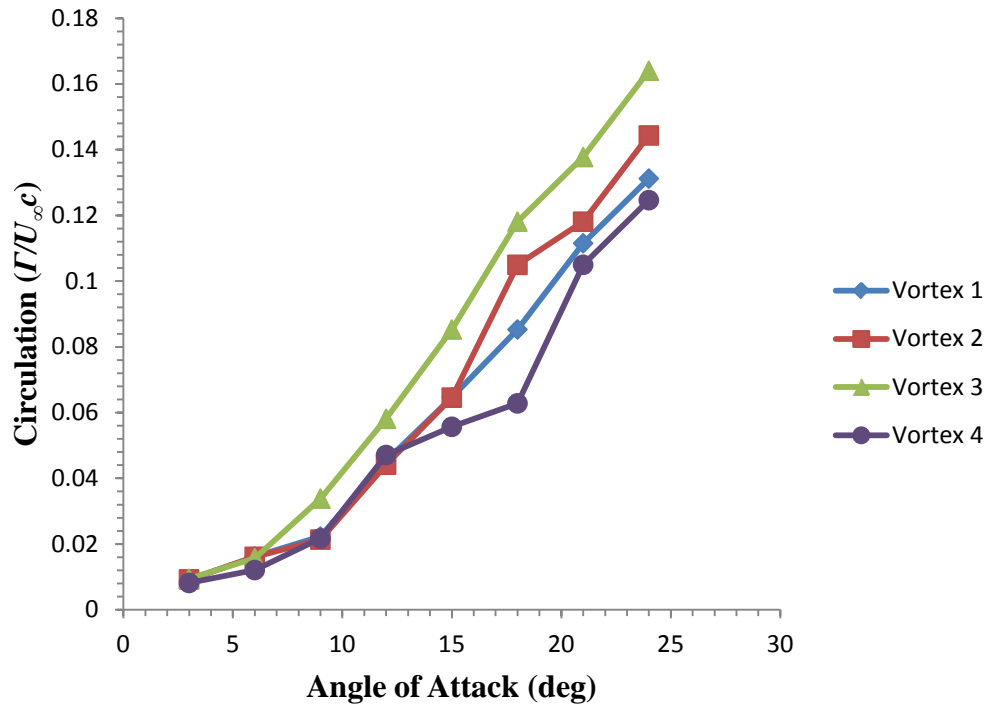Figure 59. Γ as a function of α at the chordwise location of $x/c = 0$ at $U_\infty = 0.15$ m/s.

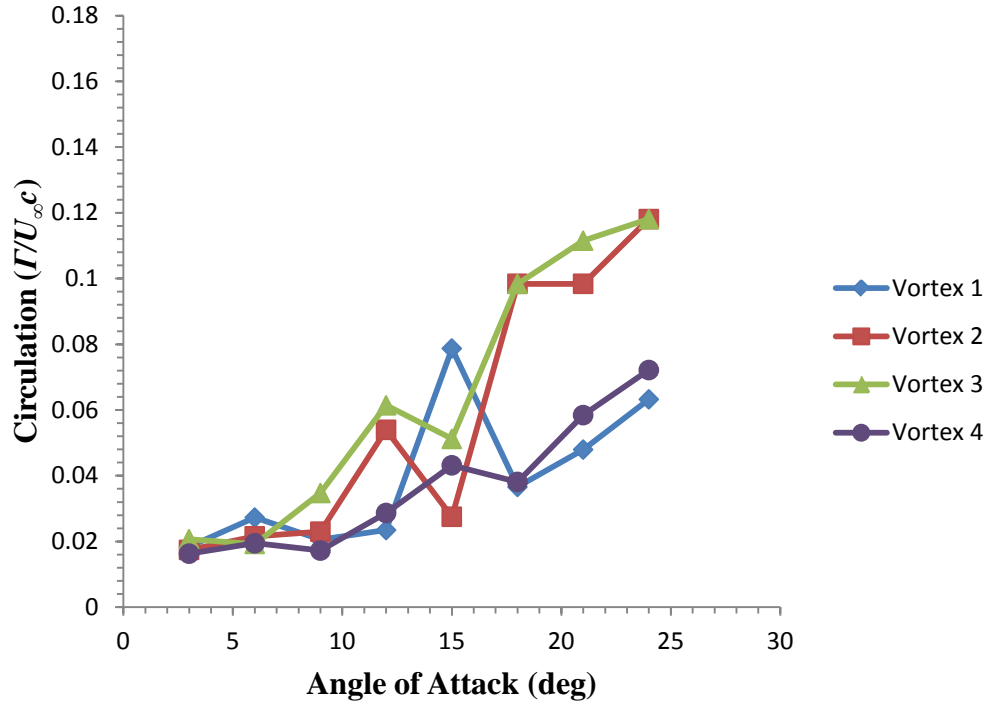Figure 60. Γ as a function of α at the chordwise location of $x/c = 0.12$ at $U_\infty = 0.15$ m/s.

Figure 61. Γ as a function of α at the chordwise location of $x/c = 0.25$ at $U_\infty = 0.15$ m/s.
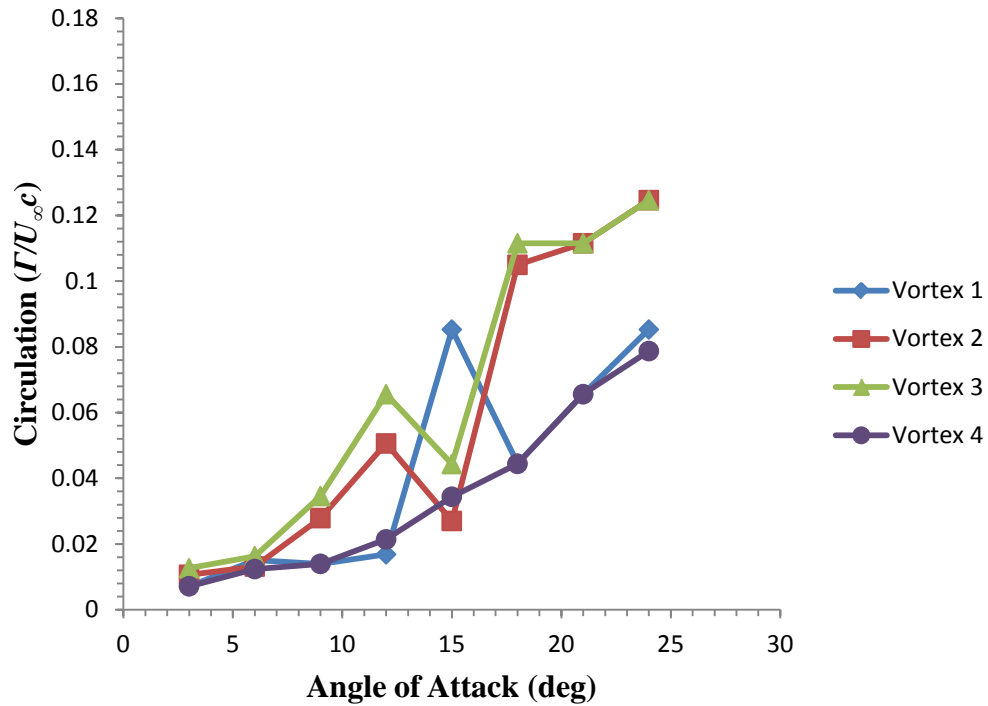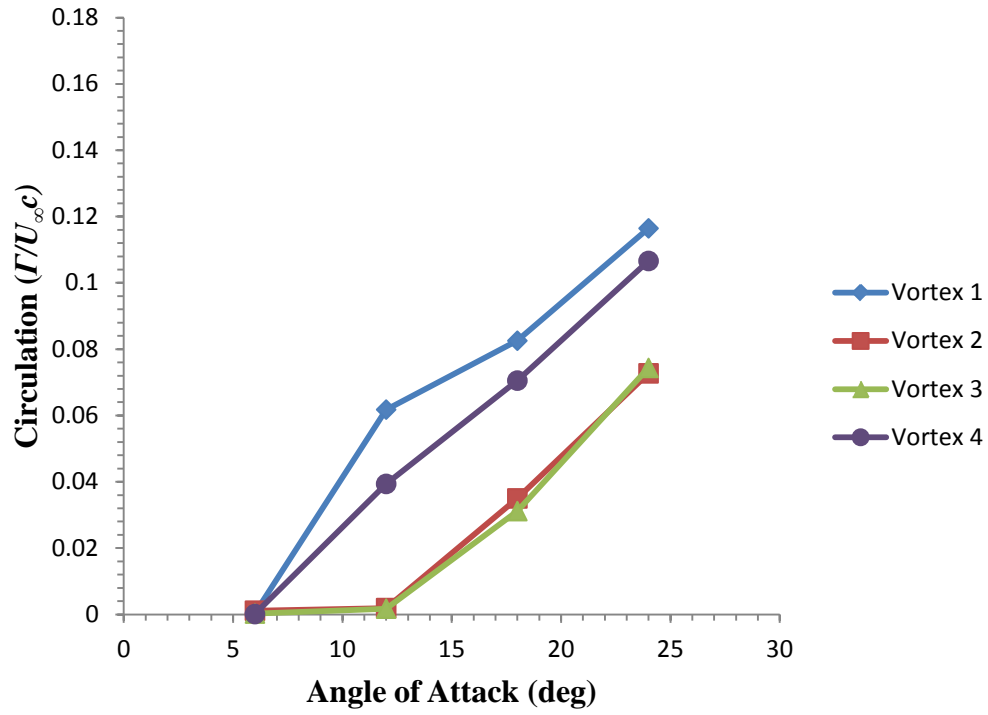

Figure 62. Γ as a function of α at the chordwise location of $x/c = 0.36$ at $U_\infty = 0.15$ m/s.

Figure 63. Γ as a function of α at the chordwise location of $x/c = 0.36$ at $U_\infty = 1.8$ m/s.
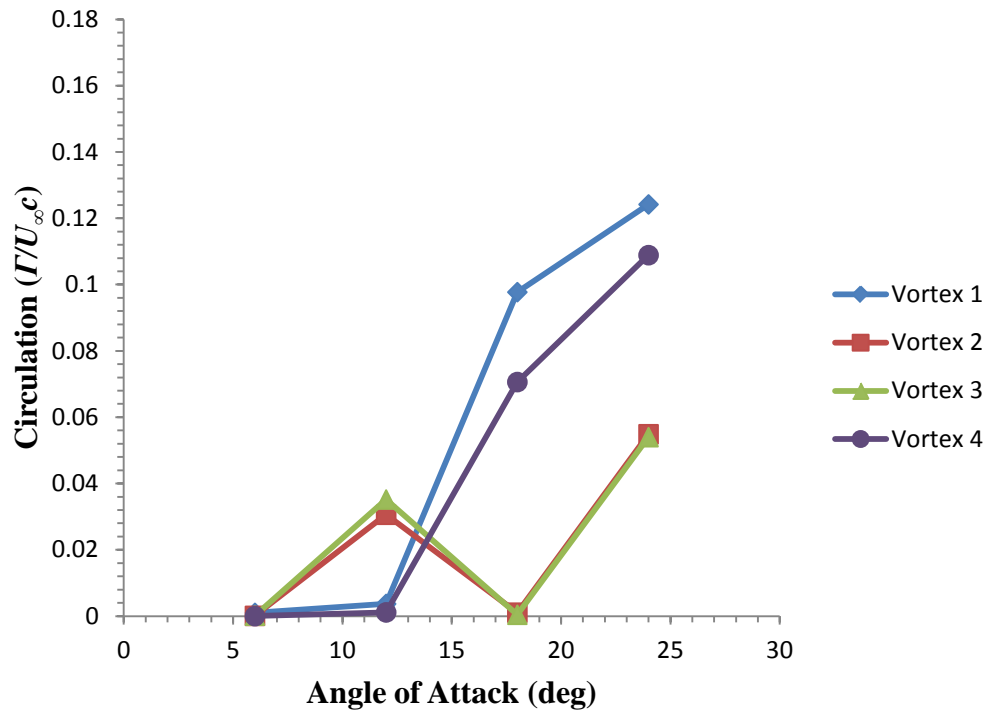

Figure 64. Γ as a function of α at the chordwise location of $x/c = 0.36$ at $U_\infty = 4.5$ m/s.

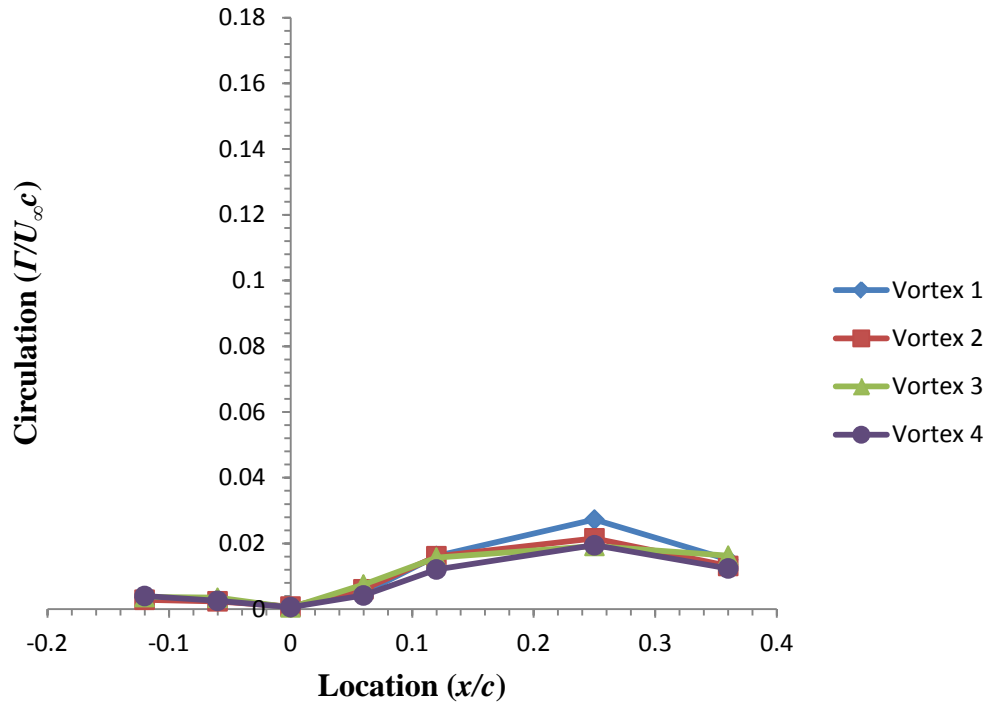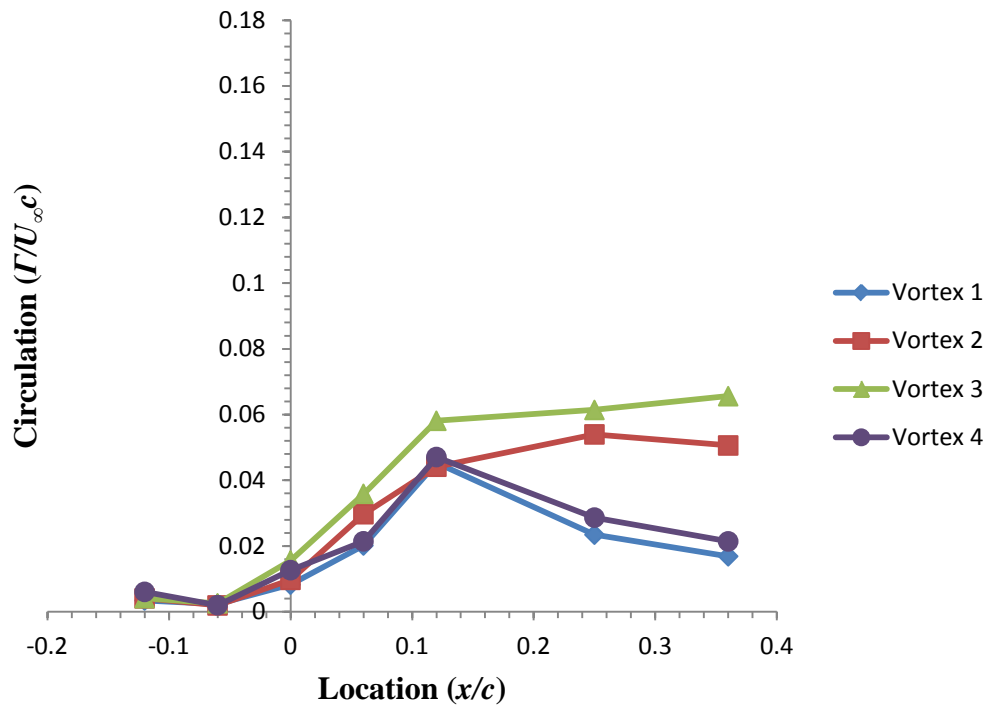Figure 65. Scaled circulation as a function of chordwise location for $\alpha = 6°$ at $U_\infty = 0.15$ m/s.

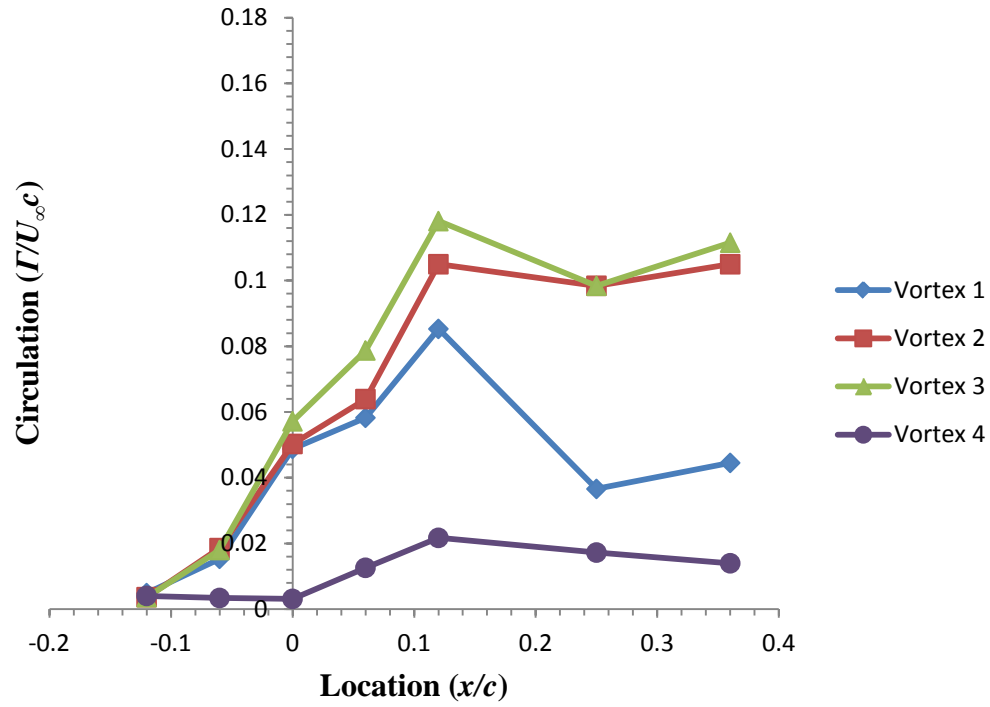Figure 66. Scaled circulation as a function of chordwise location for $\alpha = 12°$ at $U_\infty = 0.15$ m/s.

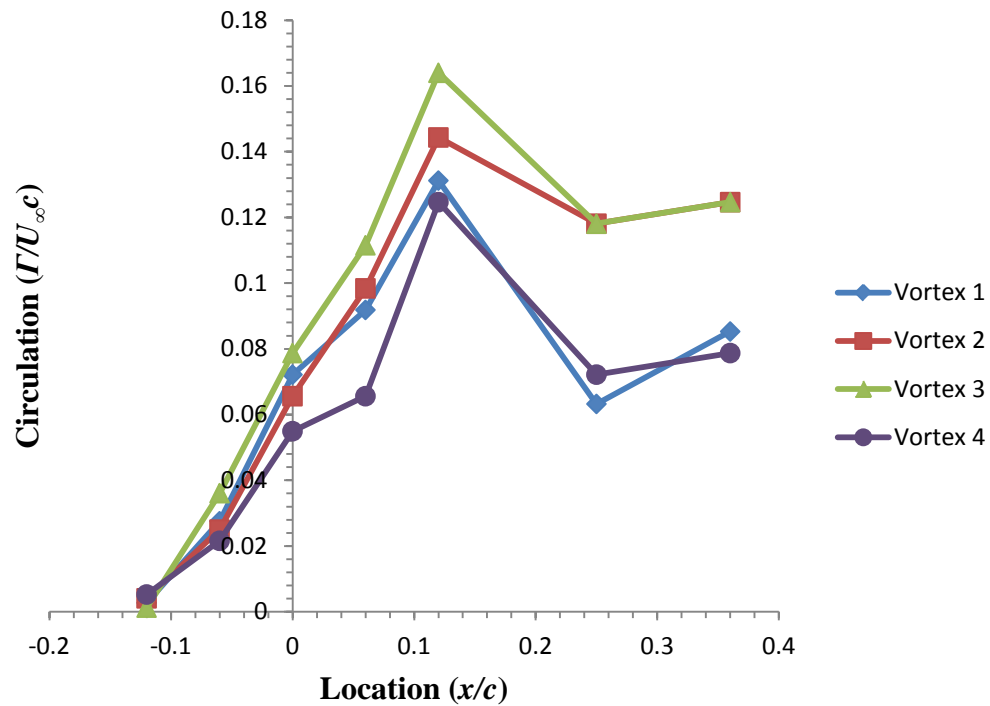Figure 67. Scaled circulation as a function of chordwise location for $\alpha = 18°$ at $U_\infty = 0.15$ m/s.

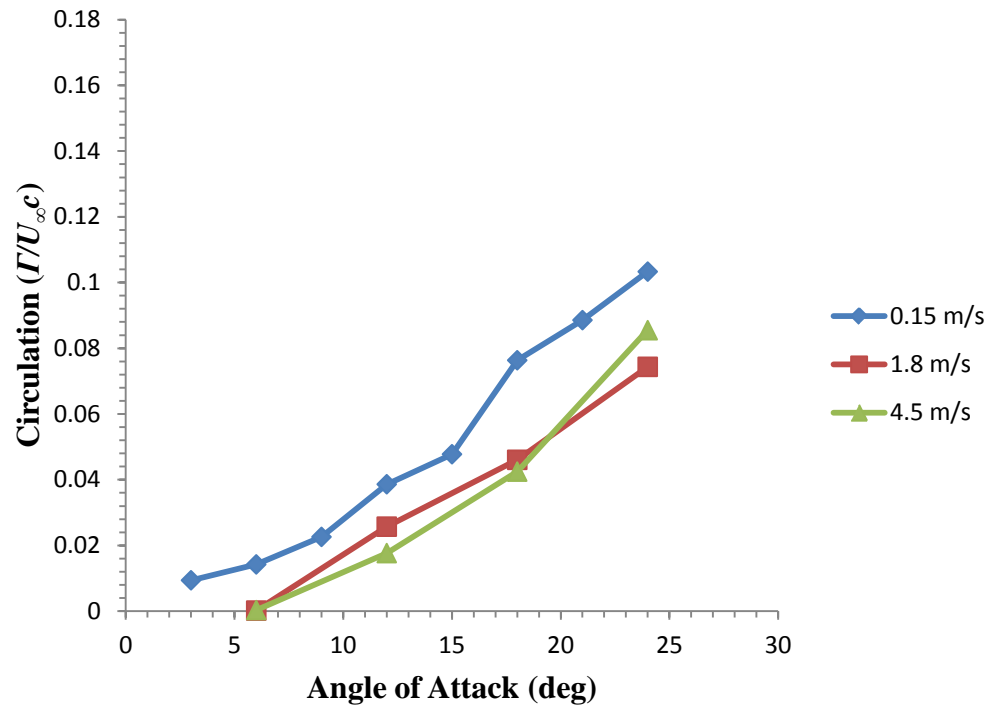Figure 68. Scaled circulation as a function of chordwise location for $\alpha = 24°$ at $U_\infty = 0.15$ m/s.

Figure 69. Averaged circulation of four vortices as a function of α at the chordwise location of $x/c = 0.36\ c$.

Finite-Span Flow Field Measurements

The presence of a tip vortex for finite-span wings and hydrofoils corresponds to an increase in drag, induced drag. Therefore, an investigation into whether leading edge protuberances are capable of mitigating the detrimental effects of a tip vortex was carried out. A stereo-PIV (SPIV) system was used to measure the flow field associated with the tip vortex of finite-span, rectangular planform hydrofoils at several angles of attack and at two spatial locations. The streamwise vorticity was computed from the measured velocity fields, and the data are presented in Figs. 70 – 73. The tip vortex emanating from the baseline hydrofoil at the freestream velocity of $U_\infty = 1.8$ m/s at two spatial locations of $x = 1.5\ c$ and $3.0\ c$ is shown in Figs. 70a and 71a, respectively. As expected, the shape and size of the tip vortex changes with the angle of attack near the trailing edge. As the angle of attack is increased to 12°, there is a corresponding increase in vortex size and strength. Further increasing the angle of attack to 18° leads to a growth of the vortex core as a result of increased lift. At an angle of 24°, concentrated vorticity in the tip vortex core of the baseline hydrofoil is spread out partially due to stall effects. The loss in lift that accompanies stall leads to a reduction in the tip vortex circulation. A similar trend can be seen at the spatial location of $x/c = 3$ for the baseline model. Likewise, comparable characteristics exist at the freestream velocity of $U_\infty = 4.5$ m/s for the baseline hydrofoil, see Figs. 72 and 73, with the exception of $\alpha = 24°$. The tip vortex core appears to persist at this high angle perhaps as a result of the higher Reynolds number. These SPIV data correspond well to the load data which show that the lift and stall characteristics at the high angle are not abrupt at the highest Reynolds number considered.

The effect of leading edge protuberances on the tip vortex of the 4L hydrofoil is shown in Figs. 70b – 73b. At the spatial location of $x = 1.5\ c$ and a freestream velocity of $U_\infty = 1.8$ m/s, the 4L hydrofoil has very similar characteristics to the baseline hydrofoil at the lower angles of attack. However, the tip vortex core remains more organized at the angle of 24°. The baseline hydrofoil has already stalled at this angle and its tip vortex has nearly dissipated. Increased lift on the leading edge modified hydrofoils observed at the higher angles of attack is primarily responsible for a stronger and more cohesive tip vortex.

Tip vortex of leading edge modified hydrofoils show similar trends to the baseline hydrofoil at both spatial locations examined. However, whereas the tip vortex of baseline hydrofoil has nearly dissipated at post-stall angles of attack at the freestream velocity of 1.8 m/s, the tip vortex

of the modified hydrofoils remain more organized. This correlates well with load data; in the post-stall regime of the baseline hydrofoil, the modified hydrofoils tend to generate more lift than the baseline model. The increased lift corresponds directly to an increase in the streamwise vorticity. At the freestream velocity of 4.5 m/s, the tip vortex is minimally affected by the presence of protuberances akin to the lift coefficient trends discussed earlier.
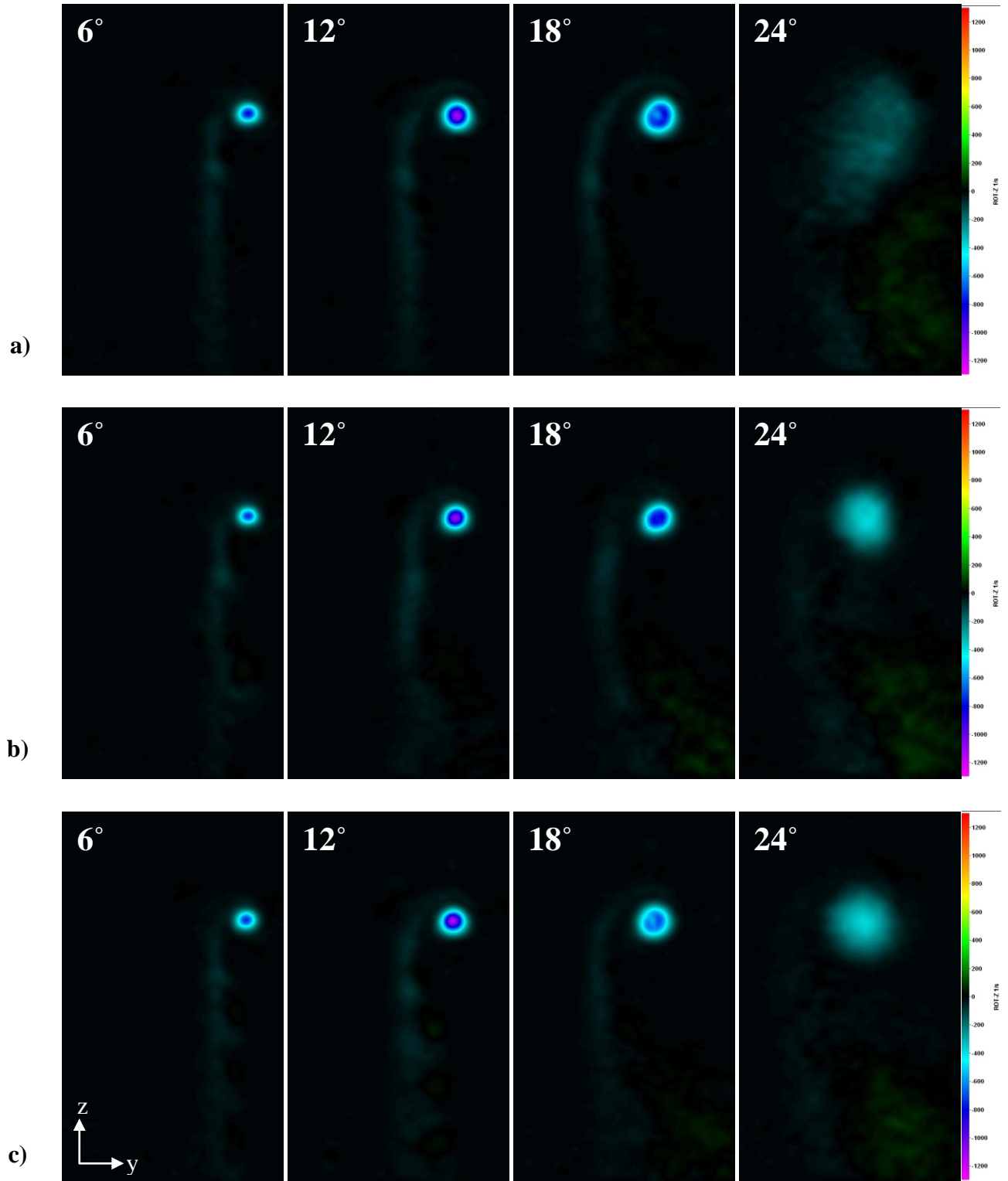
Figure 70. Streamwise vorticity contours of the tip vortex on finite-span rectangular hydrofoils 1.5 c downstream of the mean leading edge, $U_\infty = 1.8$ m/s: a) baseline, b) 4L, c) 8M.

Figure 71. Streamwise vorticity contours of the tip vortex on finite-span rectangular hydrofoils 3.0 c downstream of the mean leading edge, $U_\infty = 1.8$ m/s: a) baseline, b) 4L, c) 8M.

Figure 72. Streamwise vorticity contours of the tip vortex on finite-span rectangular hydrofoils 1.5 c downstream of the mean leading edge, $U_\infty = 4.5$ m/s: a) baseline, b) 4L, c) 8M.
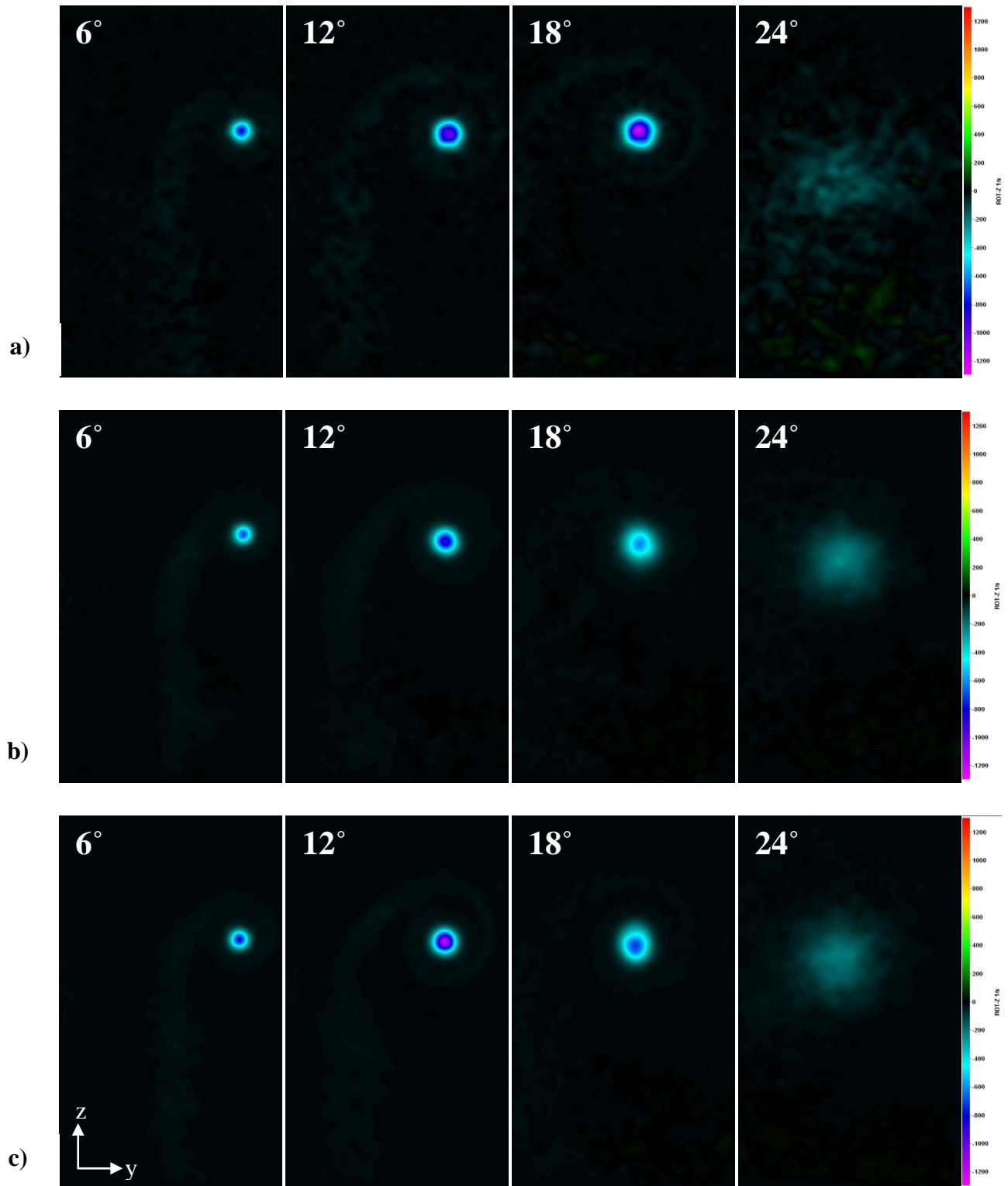
Figure 73. Streamwise vorticity contours of the tip vortex on finite-span rectangular hydrofoils 3.0 c downstream of the mean leading edge, $U_\infty = 4.5$ m/s: a) baseline, b) 4L, c) 8M.
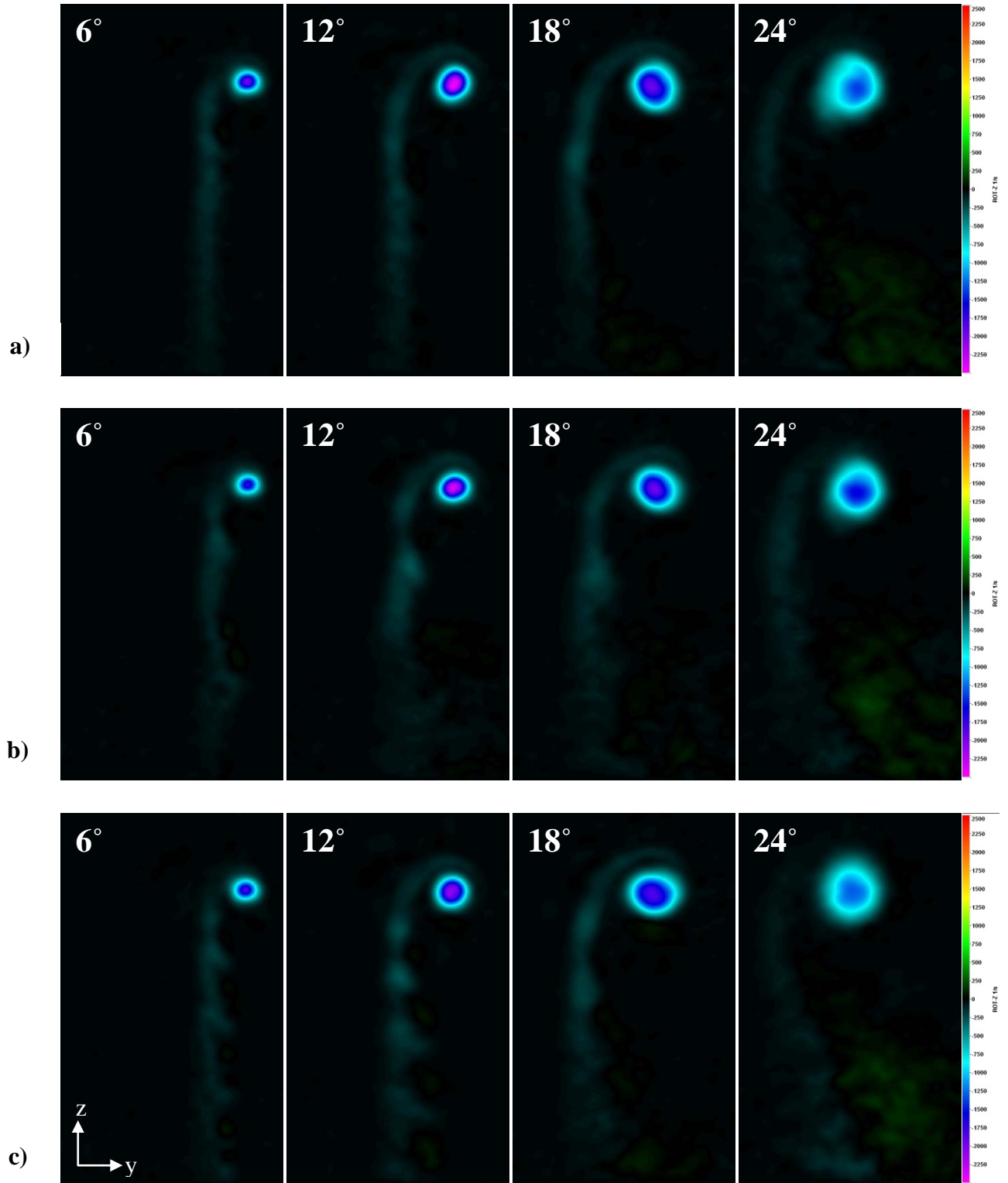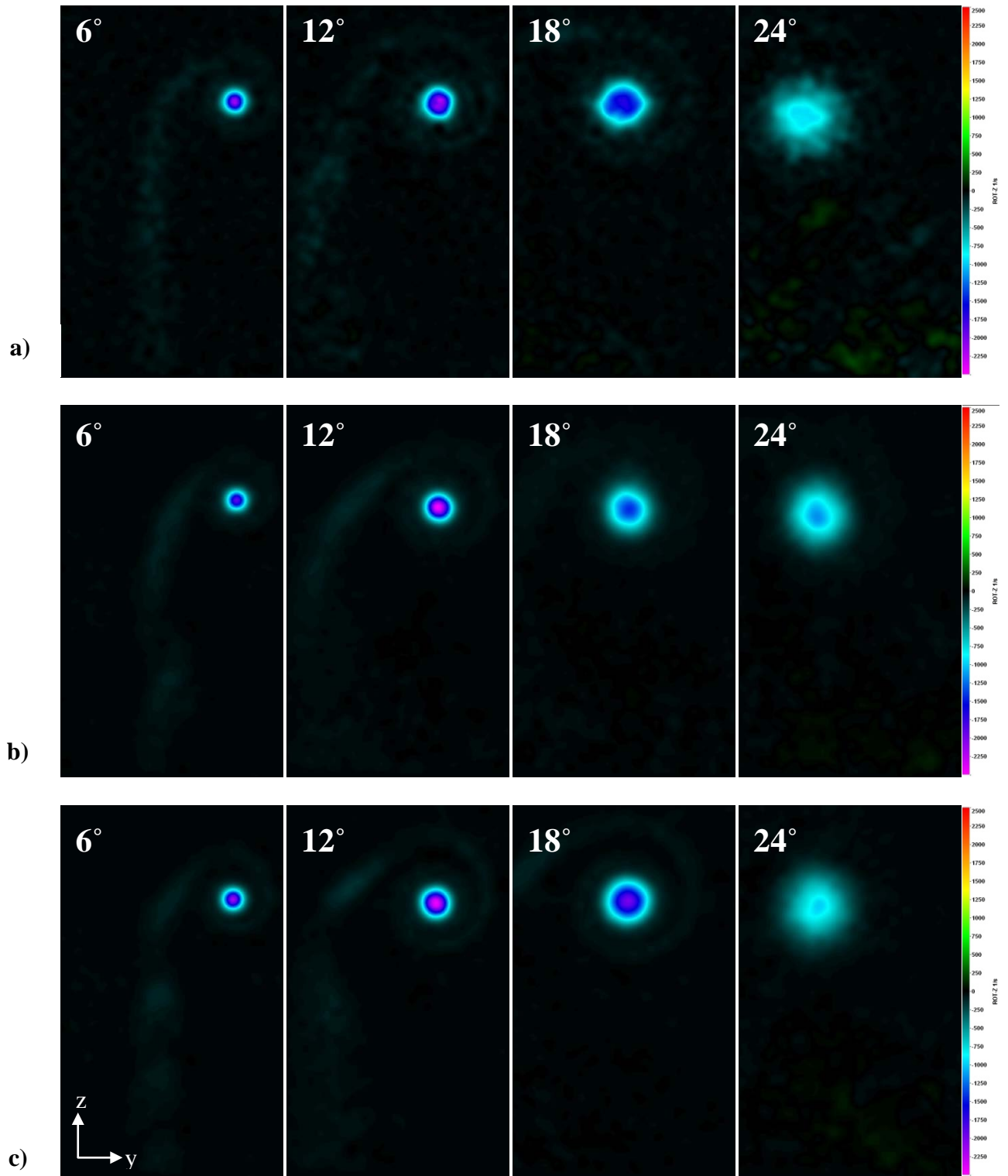
Cavitation

Finite-span rectangular hydrofoils

To investigate the effects of protuberances on cavitation characteristics, photographs were taken of finite-span rectangular and swept hydrofoils at a freestream velocity of $U_\infty = 7.2$ m/s. The images are shown in Figs. 74 – 76. Cavitation can be distinguished by the white color of the vapor that is produced in the low pressure regions. Vaporous cavitation indicates that locally the pressure has been reduced to at least the vapor pressure of water, leading to phase change.

Tip vortex cavitation

The cavitation characteristics of modified hydrofoils with a wavelength of $\lambda = 0.50 \, c$ are presented in Fig. 74. Cavitation effects on the baseline hydrofoil are shown in Figure a. As with all the hydrofoils examined, cavitation is observed first in the core of the tip vortex and is apparent at $\alpha = 12°$, the lowest angle of attack tested. With increased angle of attack, the amount of cavitation in the tip vortex grows until $\alpha = 21°$, after which point the amount of cavitation in the tip vortex decreases as a result of stall at high angles. Figures 74b and 75b illustrate that the modified hydrofoils with protuberance amplitude of $A = 0.025 \, c$ (4S and 8S) have tip vortex cavitation characteristics similar to the baseline hydrofoil, with an increase in the vortex cavity size until $\alpha = 18°$. At angles of attack greater than $\alpha = 18°$, the size of the cavity generated by the tip vortex decreases gradually. The 4M hydrofoil produces a vortex cavity that diminishes at an earlier angle than the baseline (see Fig. 74c) while the 8M hydrofoil, shown in Fig. 75c, reveals a trend similar to that of the baseline. Figures 74d and 75d show that hydrofoils with the largest amplitude protuberances (4L and 8L) have tip vortex cavities that diminish at an earlier angle than the baseline. At high freestream velocities, Reynolds number effects lead to sustained flow attachment on the baseline hydrofoil producing higher lift than the modified hydrofoils with large protuberances. This creates a stronger tip vortex on the baseline hydrofoil, in turn generating a larger tip vortex cavity.

Leading edge cavitation

The rapid acceleration of flow near the leading edge of the hydrofoils leads to reduced pressure and cavitation along the leading edge as well. Similar to the cavitation that occurs in the tip vortex, cavitation at the leading edge is also modified by the presence of protuberances. Figure 74a shows that sheet cavitation develops on the leading edge of the baseline hydrofoil with increasing angle of attack. Incipient cavitation occurs on the baseline hydrofoil at an angle

of $\alpha = 15°$. At $\alpha = 18°$, sheet cavitation has developed along the majority of the baseline hydrofoil leading edge. As the angle of attack is further increased to $\alpha = 21°$, the cavity associated with sheet cavitation enlarges and remains essentially the unchanged as the angle of attack reaches $\alpha = 24°$.

For all modified hydrofoils, incipient sheet cavitation on modified hydrofoils initiates in the troughs of the protuberances. This is due to the large leading edge radius in the troughs of modified hydrofoils leading to the lowest local pressures. Modified hydrofoils with the largest protuberance amplitude of $A = 0.12\,c$ show incipient cavitation at angles as low as $\alpha = 12°$ whereas all other modified hydrofoils show the incipient condition at an angle of $\alpha = 15°$. Hydrofoils with the smallest protuberance amplitude of $A = 0.025\,c$, shown in Figs. 74b and 75b, develop sheet cavitation similar to the baseline hydrofoil, with increasing sheet size corresponding to an increase in angle of attack and nearly the full extent of the span cavitating at the higher angles. However, sheet cavitation along the leading edge of the 4S and 8S hydrofoils is limited to a smaller fraction of the chordlength.

At high angles of attack, vortex interactions on the surface of the modified hydrofoils leads to increased pressures and transient cavitation cells behind the troughs. Therefore, cavitation along the leading edge of modified hydrofoils is somewhat unsteady. This is true for all modified hydrofoils at the higher angles of attack but especially true for the hydrofoils with the larger amplitude protuberances. The 4L and 8L modified hydrofoils with large protuberance amplitudes cavitate only in the troughs and not along the entire leading edge. Hydrofoils with middle (4M and 8M) and large amplitude (4L and 8L) protuberances have similar cavitation characteristics.

Wavelength plays only a minor role in establishing the cavitation patterns observed on the modified hydrofoils. Generally, hydrofoils with a shorter wavelength develop transient cavitation cells at higher angles of attack than the hydrofoils with a longer wavelength.

Swept hydrofoils

The effect of protuberances on the cavitation characteristics of finite-span swept hydrofoils is shown in Fig. 76. Cavitation is apparent in the tip vortex of the baseline hydrofoil at the lowest angle examined. However, at angles of attack greater than $\alpha \geq 18°$, tip vortex cavitation disappears all together. This is likely caused by stall effects at the tip of the hydrofoil that result in increased pressures. Little to no cavitation is apparent on the leading edge of the baseline hydrofoil until an angle of $\alpha = 21°$ is reached. At angles of attack $\alpha \geq 21°$, leading edge sheet

cavitation occurs over nearly 1/3 – 1/2 of the span. The lack of cavitation near the root as well as the tip of the hydrofoils are the result of low-speed and/or spanwise flow at these locations.

The cavitation characteristics of the leading edge modified swept hydrofoil are shown in Fig. 77b. Contrary to the baseline hydrofoil, tip vortex cavitation is apparent at all angles of attack considered, with similar characteristics throughout the entire range of angles. Incipient sheet cavitation can be seen in the troughs of the modified hydrofoil at angles as low as $\alpha = 12°$. As the angle of attack is increased, the extent of cavitation along the span increases somewhat. Vortex interactions account for lack of cavitation in the central tough of the modified swept hydrofoil at $\alpha \geq 18°$.
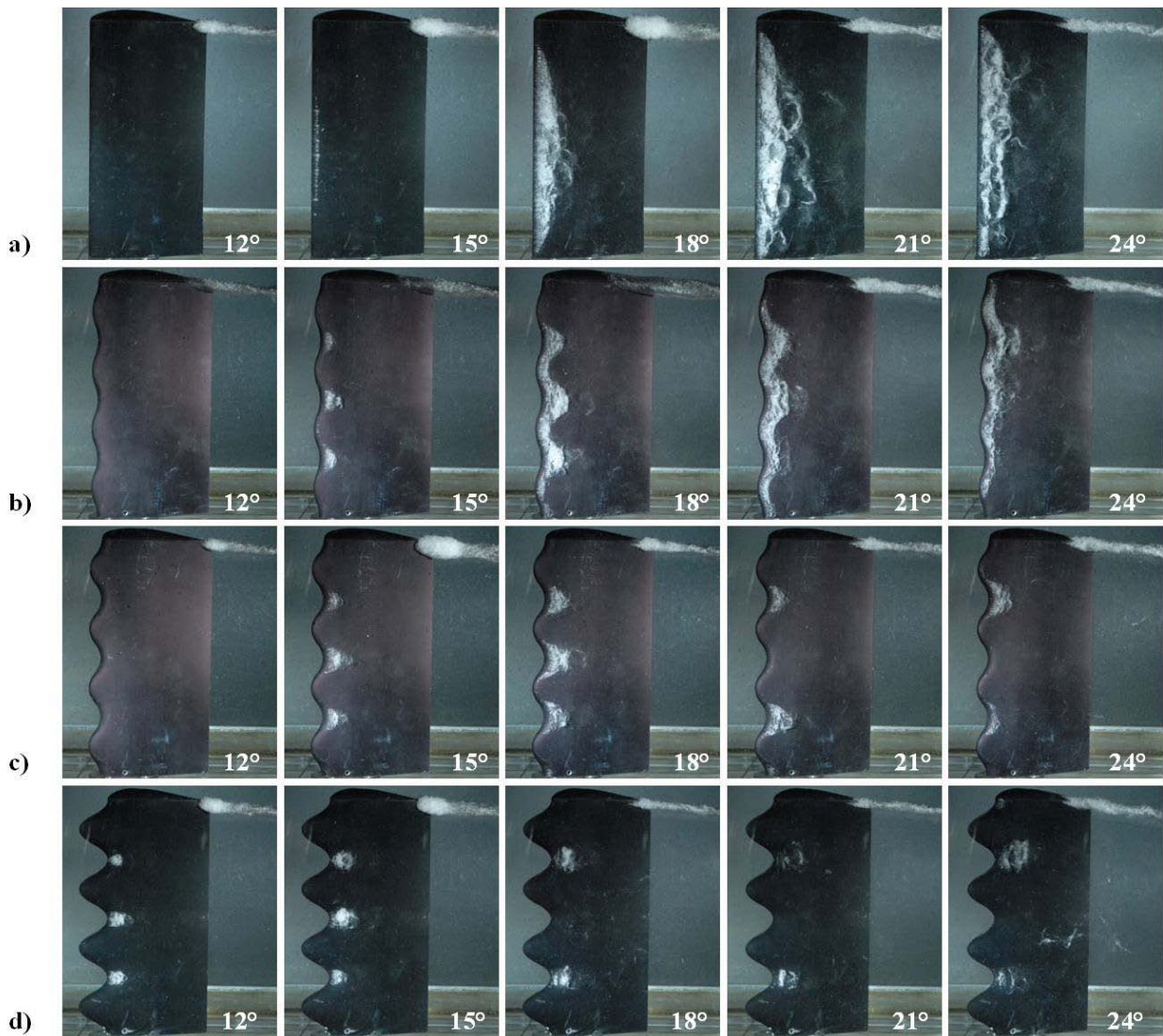

Figure 74. Vaporous cavitation on the leading edge and tip vortex of finite-span rectangular hydrofoils: a) baseline, b) 4S, c) 4M, and d) 4L.
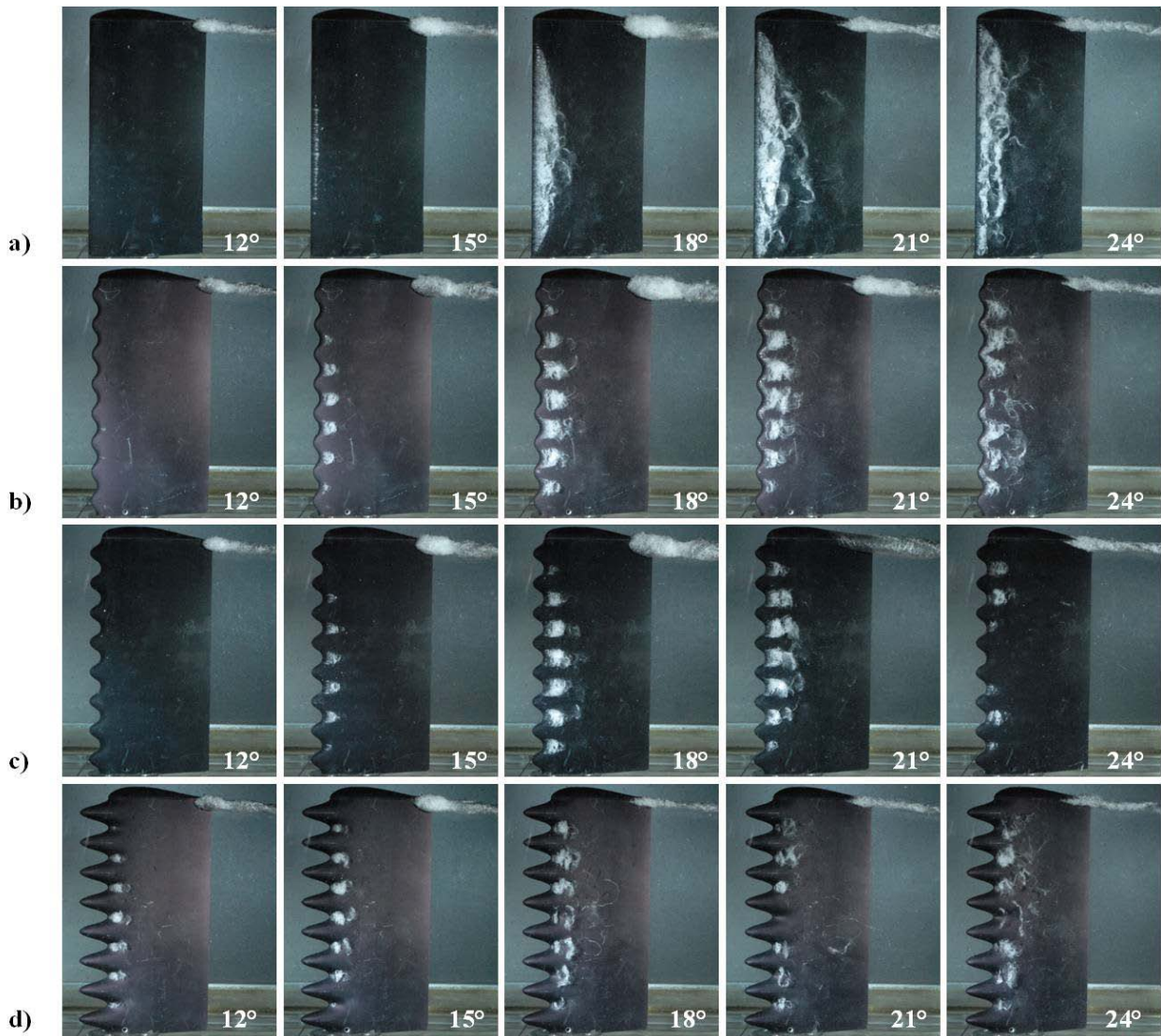
Figure 75. Vaporous cavitation on the leading edge and tip vortex of finite-span rectangular hydrofoils: a) baseline, b) 8S, c) 8M, and d) 8L.
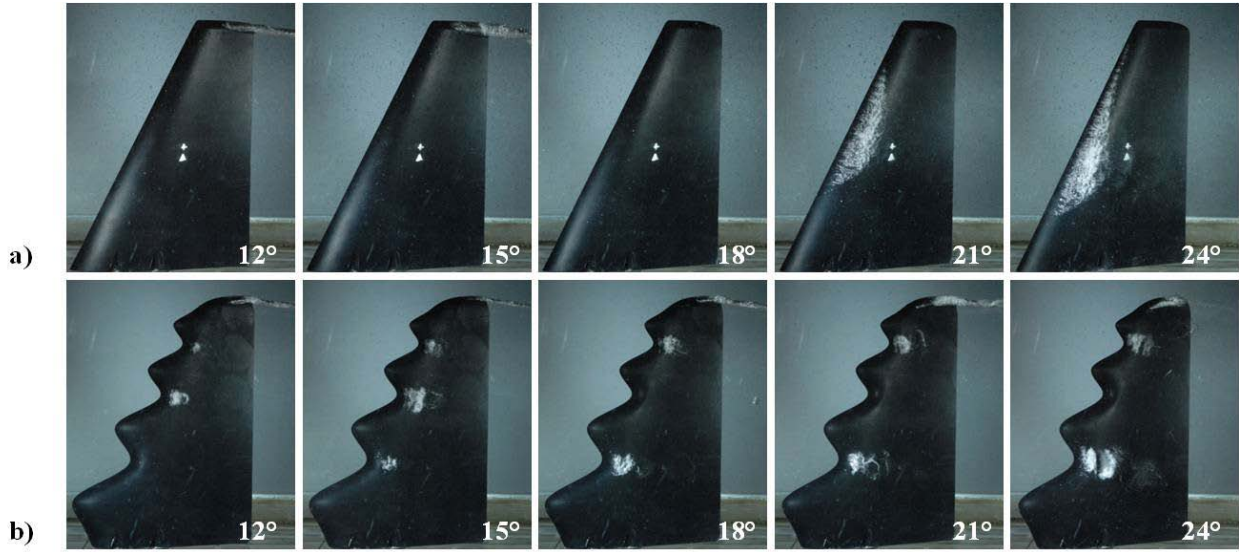
Figure 76. Vaporous cavitation on the leading edge and tip vortex of finite-span swept hydrofoils: a) baseline, b) modified.

Loads on finite-span rectangular hydrofoils with cavitation

Load measurements were carried out on the baseline and modified finite-span rectangular and swept planform hydrofoils to determine the effects of cavitation patterns on the loads. These tests were performed at a freestream velocity of $U_\infty = 7.2$ m/s, which corresponds to the freestream velocity at which incipient leading edge sheet cavitation occurs on the baseline hydrofoil at an angle $\alpha = 15°$. At angles of attack $\alpha \geq 15°$, all hydrofoils exhibited cavitation in the tip vortex core as well as at the leading edge to various extents. At angles of attack $\alpha \leq 15°$, all hydrofoils had indications of cavitation in the tip vortex cavitation core, with leading edge cavitation apparent on select modified hydrofoils as described in the previous section.

The lift coefficient of the baseline hydrofoil in Fig. 77a increases linearly at low angles of attack and continues to produce increasing lift with angle of attack until $\alpha \approx 22°$, after which point a gradual stall and loss of lift occurs. Cavitation appears to play a minor role in the lift characteristics of the baseline hydrofoil. The drag coefficient of the baseline hydrofoil, shown in Fig. 77b, increases quadratically with angle of attack for nearly the entire range of angles of attack. Table 20 presents important hydrodynamic characteristics of the finite-span rectangular hydrofoils with cavitation.

106

Table 20. Hydrodynamic characteristics of finite-span rectangular planform hydrofoils with cavitation.

$Re_c = 7.2 \times 10^5$	$\frac{dC_L}{d\alpha}$ [deg^{-1}]	C_{Lmax}	α @ C_{Lmax} [deg]	C_{Dmin}	L/D_{max}	α @ L/D_{max} [deg]	α_{stall} [deg]
Baseline	0.055	1.12	22.3	0.02	11.4	7.2	23.7
4S	0.055	1.06	20.8	0.02	11.4	7.4	20.8
4M	0.054	1.05	19.5	0.02	10.8	7.6	21.0
4L	0.048	0.91	17.8	0.02	8.6	7.6	19.2
8S	0.054	1.07	20.7	0.02	11.3	7.3	22.2
8M	0.052	1.02	20.9	0.02	10.5	7.6	20.9
8L	0.051	0.77	15.8	0.02	9.7	7.5	18.7

Effect of amplitude

The effect of protuberance amplitude on the load characteristics of modified hydrofoils under cavitating conditions are presented in Figs. 77 and 78. The lift coefficient of modified hydrofoils with a protuberance amplitude of $\lambda = 0.50\,c$, shown in Fig. 77a, reveals that the all hydrofoils perform similarly at angles of attack in the range of $0° \leq \alpha \leq 16°$. However, over a small range of angles of attack of $16° \leq \alpha \leq 20°$, the lift coefficient of the 4S and 4M hydrofoils are slightly greater than that of the baseline. With this exception, the baseline lift coefficient outperforms all modified cases. The same trend is also present for the modified hydrofoils with a wavelength of $\lambda = 0.25\,c$, shown in Fig. 78a. Under cavitation condition, hydrofoils with protuberances amplitudes of $A = 0.025\,c$ and $0.050\,c$ perform similarly to each other, while hydrofoils with the protuberance amplitude of $A = 0.12\,c$ have the poorest lift coefficient performance of all hydrofoils when cavitation is present.

The drag coefficients of modified hydrofoils with cavitation are shown in Figs. 77b and 78b. The drag coefficients are very similar to that of the baseline hydrofoil. This trend is much different than that shown in cases in which cavitation was absent. Whereas the drag on modified hydrofoils is significantly higher than that of the baseline at the lower freestream velocities without cavitation, the drag of modified hydrofoils is very similar to the baseline case when significant regions with cavitation is present.

Effect of wavelength

The load characteristics of hydrofoils with protuberances amplitudes of $A = 0.025c - 0.12c$ are presented in Figs. 79 – 81, respectively. The series of plots reveals that, with the exception of modified hydrofoils with the protuberance amplitude of $A = 0.12\,c$, wavelength does not play a major role in establishing the load characteristics on hydrofoils with cavitation throughout the angle of attack range considered.

The lift coefficient of the two leading edge modified hydrofoils with protuberance amplitude of $A = 0.12\,c$ is shown in Fig. 81a. The baseline and these two hydrofoils perform similarly until $\alpha \approx 15°$, at which point C_L of the modified hydrofoils begin to decrease gradually. For the rest of angles of attack, there is a 7% difference between the lift coefficient of the 4L and 8L hydrofoils.

The drag coefficient of the two leading edge modified hydrofoils with protuberance amplitude of $A = 0.12\,c$, shown in Figure 81b, reveals that there is no difference in C_D between the modified cases at low angles of attack. However, at angles of attack greater than 20°, drag characteristics become increasingly diverse, with C_D of the 8L hydrofoil becoming nearly constant while that of the 4L hydrofoil continues to increase.
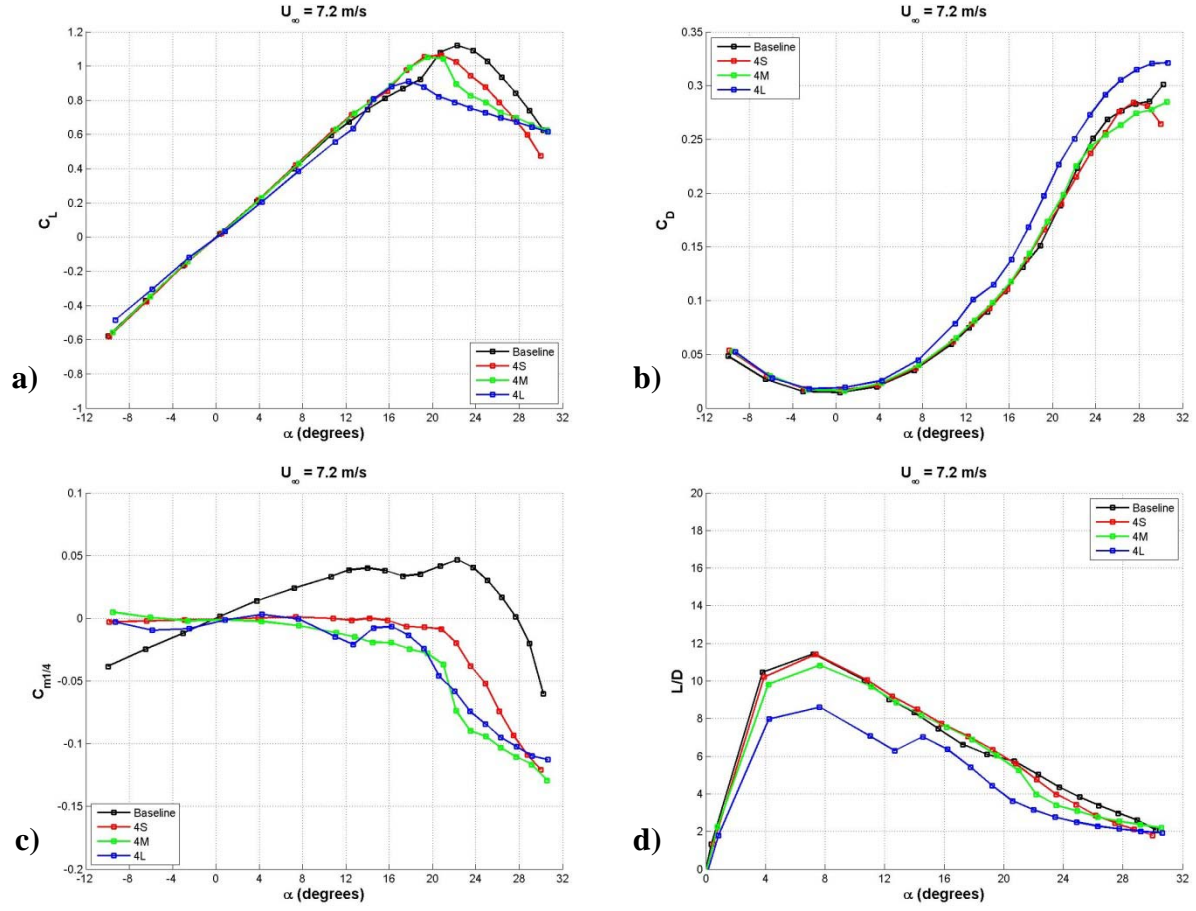
Figure 77. Effect of protuberance amplitude on the load characteristics of cavitating hydrofoils with a protuberance wavelength of $\lambda = 0.50$ c: a) lift coefficient, b) drag coefficient, c) pitching moment coefficient, d) lift-to-drag ratio.
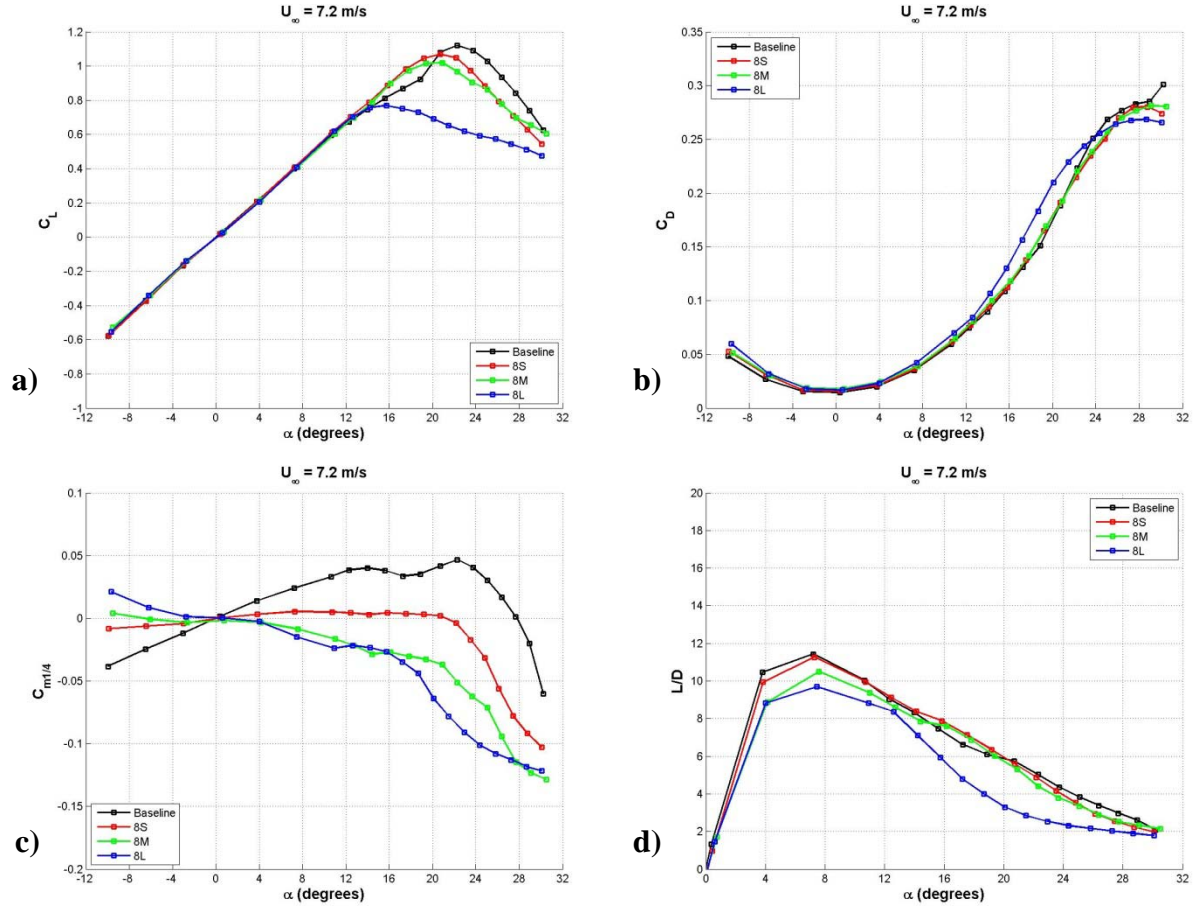
Figure 78. Effect of protuberance amplitude on the load characteristics of cavitating hydrofoils with a protuberance wavelength of $\lambda = 0.25$ c: a) lift coefficient, b) drag coefficient, c) pitching moment coefficient, d) lift-to-drag ratio.
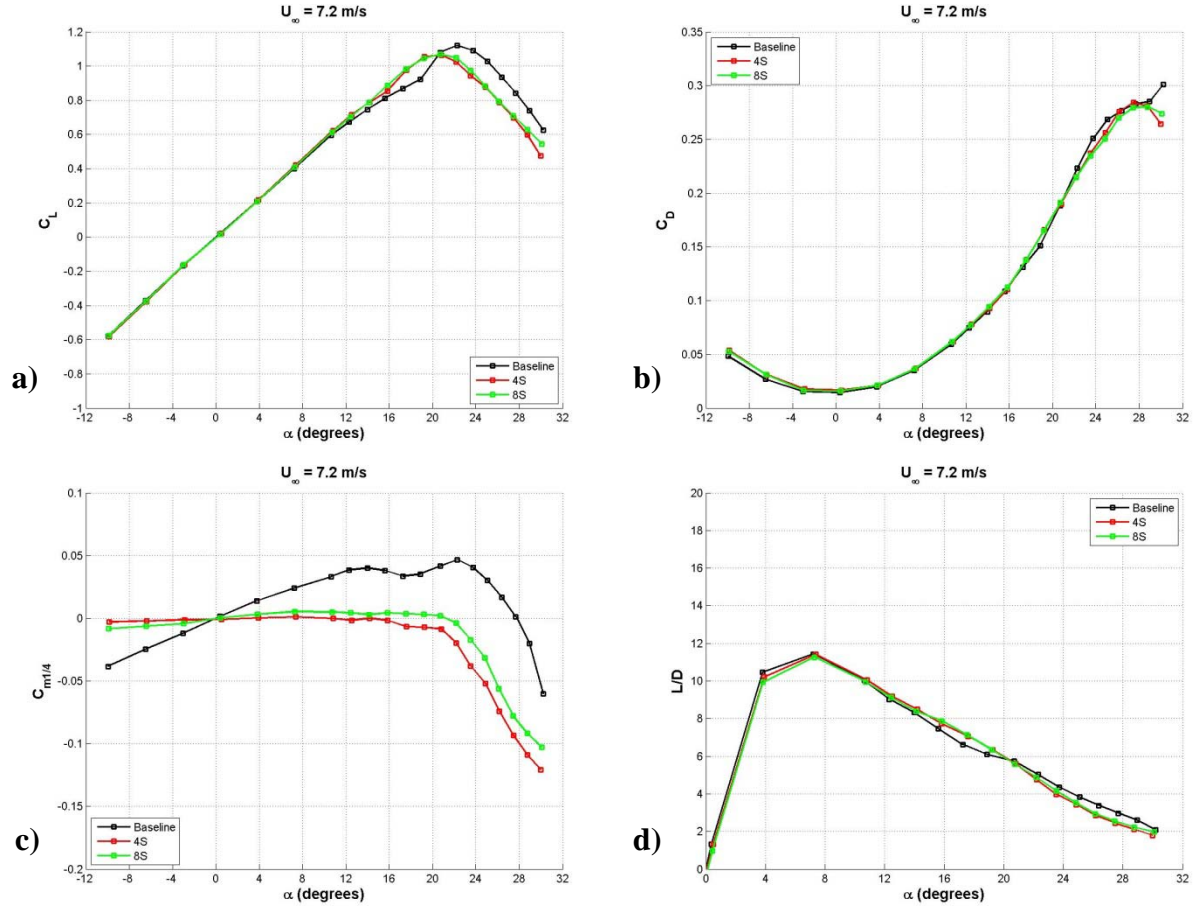
Figure 79. Effect of protuberance wavelength on the load characteristics of cavitating hydrofoils with a protuberance amplitude of $A = 0.025\ c$: a) lift coefficient, b) drag coefficient, c) pitching moment coefficient, d) lift-to-drag ratio.

Figure 80. Effect of protuberance wavelength on the load characteristics of cavitating hydrofoils with a protuberance amplitude of $A = 0.05$ c: a) lift coefficient, b) drag coefficient, c) pitching moment coefficient, d) lift-to-drag ratio.

Figure 81. Effect of protuberance wavelength on the load characteristics of cavitating hydrofoils with a protuberance amplitude of $A = 0.12$ c: a) lift coefficient, b) drag coefficient, c) pitching moment coefficient, d) lift-to-drag ratio.
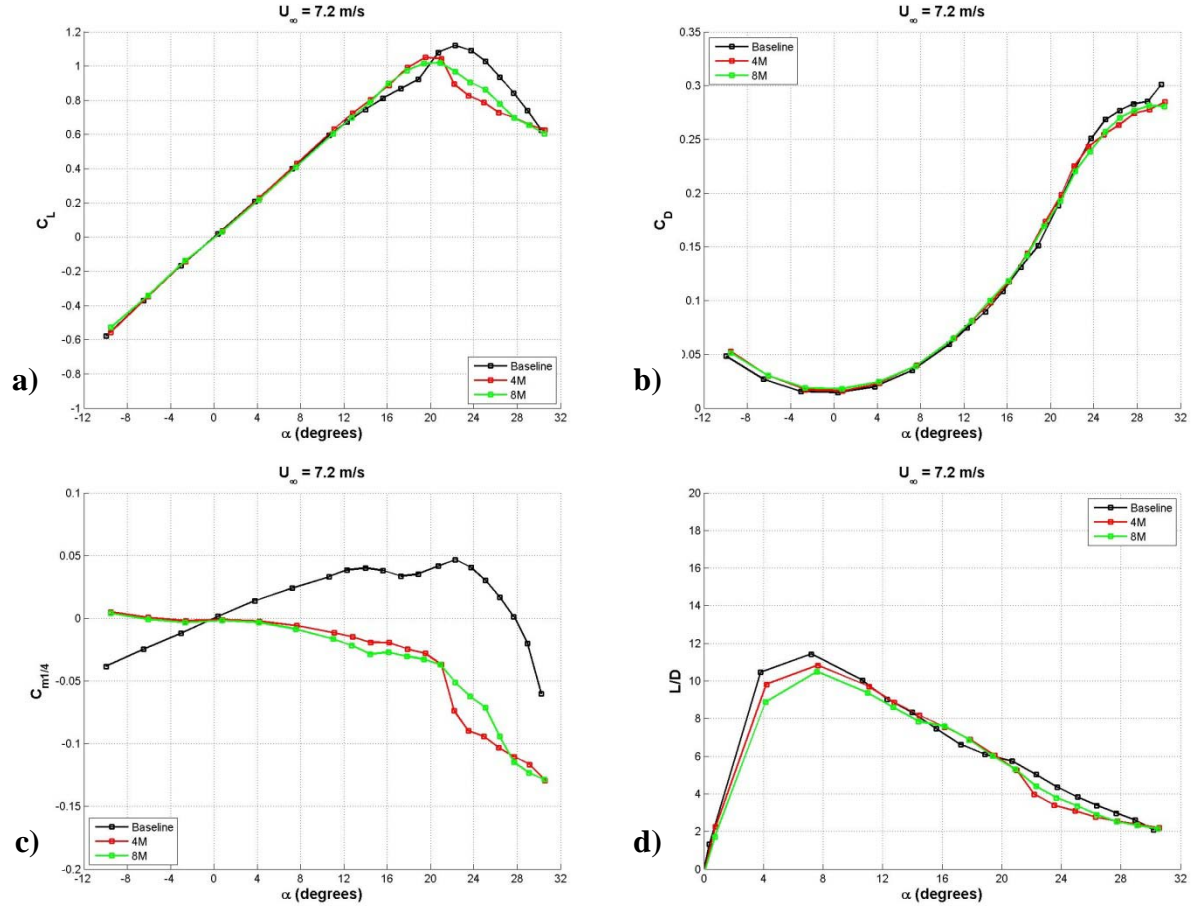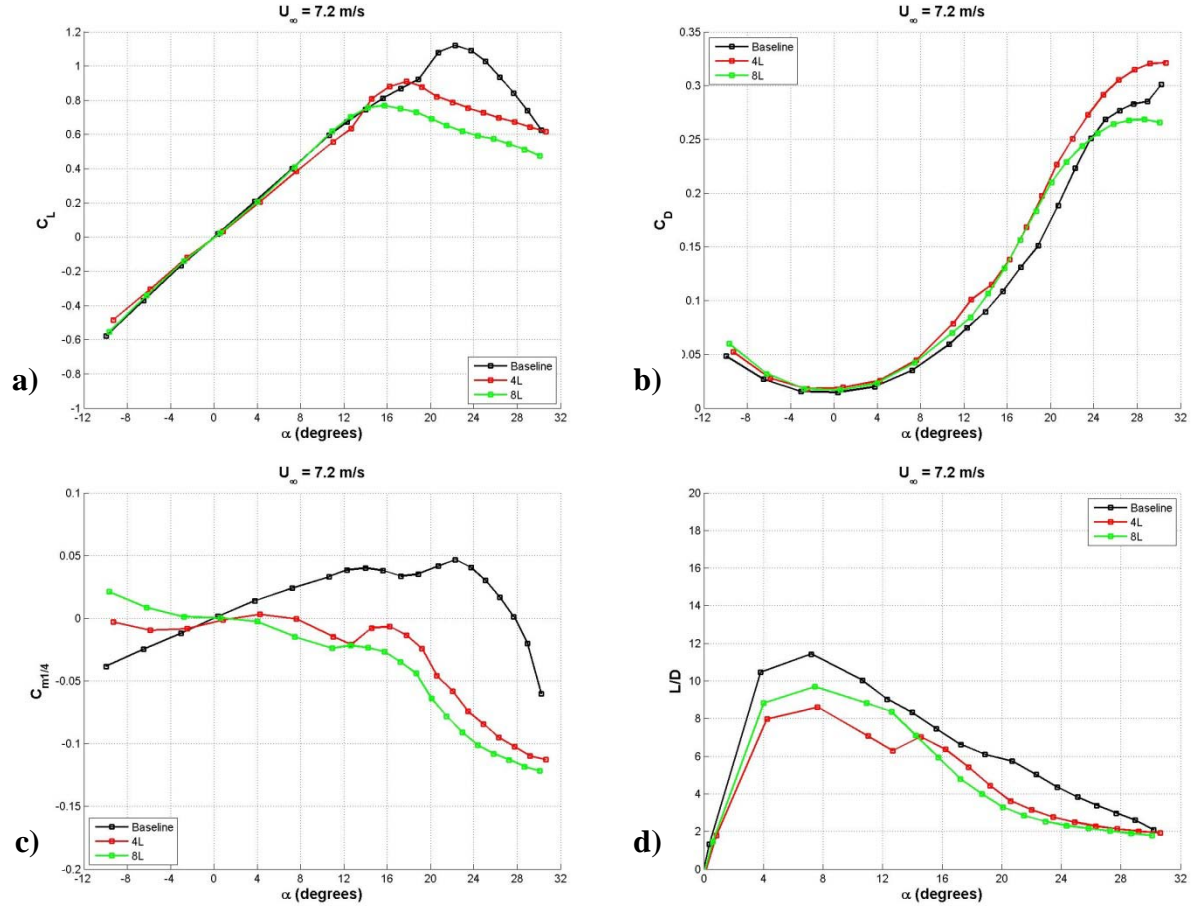
Swept hydrofoil loads with cavitation

The load characteristics of the modified swept planform hydrofoil are compared to the baseline hydrofoil in Fig. 82. The lift coefficient of the baseline hydrofoil is either greater than or nearly equal to that of the modified case for all angles of attack, see Fig. 82a. There is a gradual or 'soft' stall in both cases with no signs of a dramatic loss of lift at high angle of attack. The baseline lift coefficient is significantly greater than the modified hydrofoil over the range of angles of attack of $15° \ \alpha \le 29°$ producing as much as 20% more lift than the modified hydrofoil.

The drag coefficient of the swept planform hydrofoils is shown in Fig. 82b where the drag coefficient is nearly the same for the two hydrofoils at angles of attack less than $\alpha \approx 15°$. Over the range of angles $15° \le \alpha \le 29°$, C_D of the modified hydrofoil is slightly greater than that of the baseline with an increase in drag of $\approx 12\%$. At even greater angles of attack, drag coefficients of the baseline and modified hydrofoils become nearly equal, to within experimental uncertainty. Table 21 shows important hydrodynamic characteristics of the swept planform hydrofoils under cavitation conditions.

Table 21. Hydrodynamic characteristics of swept planform hydrofoils under cavitation conditions.

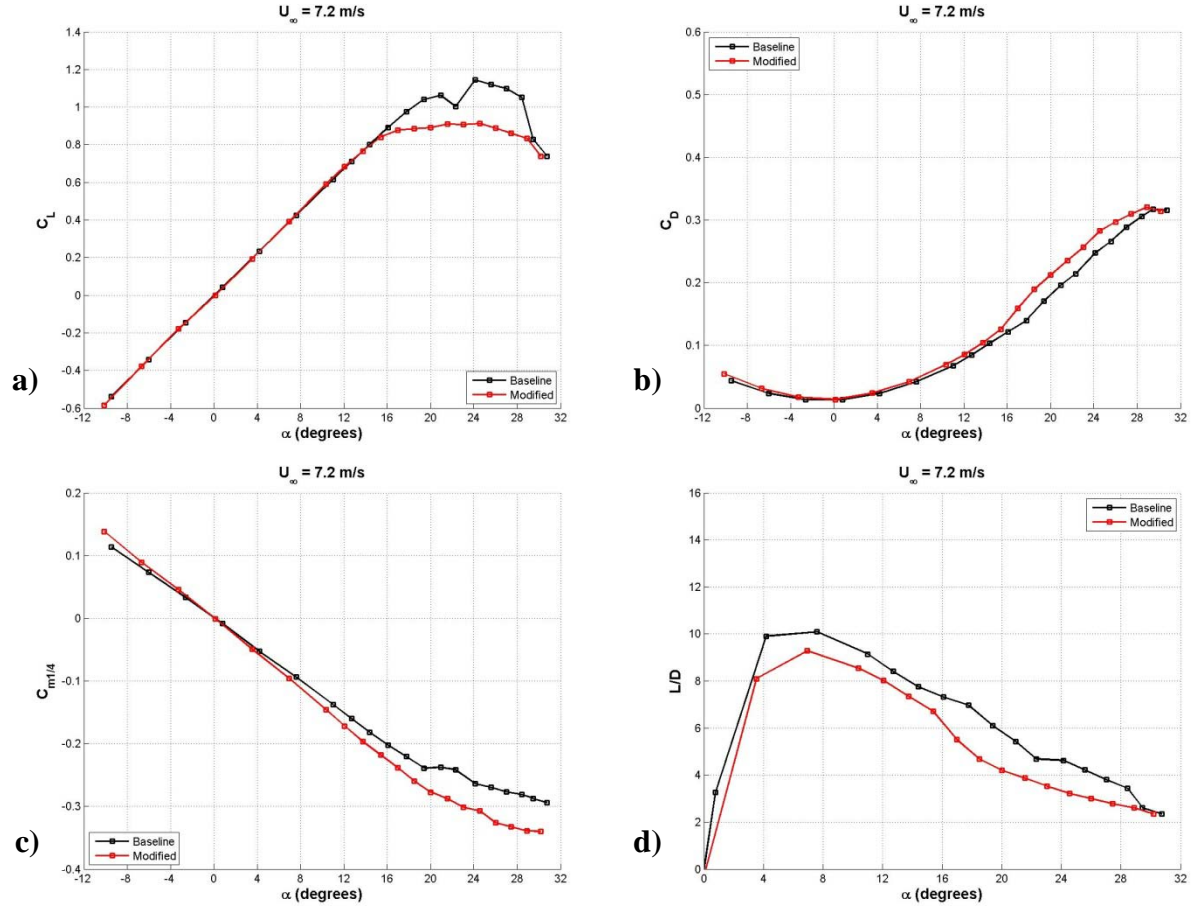| $Re_c = 7.2 \times 10^5$	$\frac{dC_L}{d\alpha}$ [deg^{-1}]	C_{Lmax}	α @ C_{Lmax} [deg]	C_{Dmin}	L/D_{max}	α @ L/D_{max} [deg]	α_{stall} [deg]
Baseline	0.056	1.15	24.1	0.01	10.1	7.6	28.4
Modified	0.055	0.91	24.6	0.01	9.3	7.0	N/A

Figure 82. Effect of protuberances on the load characteristics of swept planform hydrofoils with cavitation: a) lift coefficient, b) drag coefficient, c) pitching moment coefficient, d) lift-to-drag ratio.

Cavitation Number

The cavitation numbers of finite-span rectangular and swept planform modified hydrofoils were compared to their baseline counterparts over a range of angles of attack $3° \leq \alpha \leq 24°$. The cavitation number was calculated at the incipient leading edge cavitation condition, i.e. when sheet cavitation was first visually apparent on the leading edge of the hydrofoils. Cavitation number was computed in the following manner:

$$K = \frac{p - p_v}{\frac{1}{2}\rho U_\infty^2}$$

where p is the freestream static pressure, p_v is the vapor pressure of water, ρ is the density of water, and U_∞ is the freestream velocity. Cavitation number is essentially the ratio of local static pressure to the dynamic pressure and is a way of quantifying the cavitation characteristics of the hydrofoils. Consequently, higher values for cavitation number imply that, for a given local static pressure and angle of attack, incipient cavitation will occur at a lower freestream velocity. A set of experiments was carried out to compute the cavitation number at each angle of attack. This dataset shows the velocity below which a hydrofoil will operate without leading edge cavitation.

Finite-span rectangular hydrofoils

The cavitation number as a function of angle of attack for finite-span rectangular hydrofoils is shown in Fig. 83. The cavitation number for the baseline hydrofoil was less than that for the modified hydrofoils for the entire range of angles of attack. The modified hydrofoils with protuberance amplitudes of $A = 0.025\ c$ and $0.05\ c$ perform similar to the baseline with incipient cavitation being nearly independent of protuberance wavelength. The cavitation numbers of the hydrofoils with smaller amplitudes (4S and 8S) are always greater than that of the baseline model with a maximum difference of $\approx 20\%$ at the higher of angles of attack. Past the angle of attack of $\alpha = 6°$, the 4L hydrofoil has a cavitation number consistently greater than the baseline and the other modified hydrofoils with the same protuberance wavelength. The data in Fig. 83 also show that the incipient cavitation number of hydrofoils with the largest protuberance amplitudes $A = 0.12\ c$ is highly dependent on wavelength. The 8L hydrofoil, which has a wavelength that is half that of the 4L, exhibits a maximum cavitation number that is nearly 72% and 125% greater than that of the 4L and baseline hydrofoils, respectively. In terms of freestream velocities at which the hydrofoils will cavitate; Fig. 83 shows that if at an angle of $\alpha = 15°$ the

baseline hydrofoil shows incipient leading edge cavitation at a freestream velocity of $U_\infty = 7.2$ m/s, as shown in Figures 74 and 75, the 4L and 8L hydrofoils will have incipient cavitation at freestream velocities of $U_\infty = 5.49$ and 4.8 m/s, respectively, for the same local static pressure.
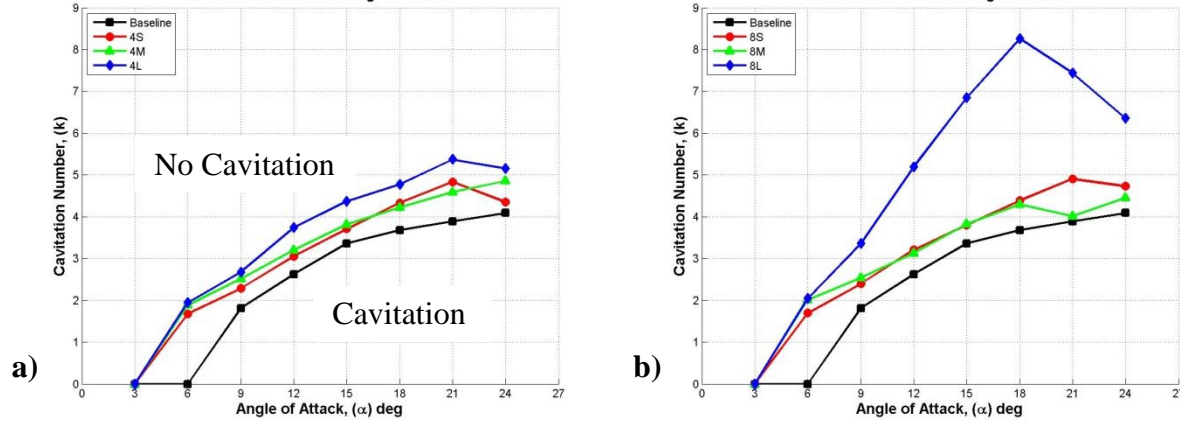

Figure 83. Incipient cavitation number of finite-span rectangular modified hydrofoils as a function of angle of attack: a) $\lambda = 0.50 \ c$, and b) $\lambda = 0.25 \ c$.

Finite-span swept hydrofoils

The cavitation number for the swept planform hydrofoils is shown in Fig. 84. For all angles of attack at which leading edge cavitation was present, the cavitation number of the modified hydrofoil was $\approx$ 50% greater than that of the baseline hydrofoil. Consequently, this implies that for a given angle of attack and local static pressure, the modified model will cavitate at freestream velocities 19% lower than the baseline. In general, the values for cavitation numbers of the modified hydrofoils are nearly a constant percentage greater than the baseline model.
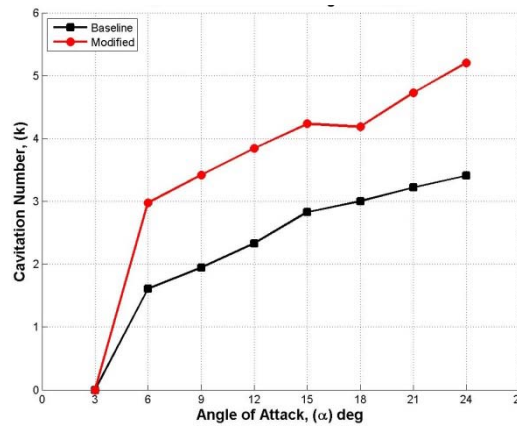

Figure 84. Incipient cavitation number for the swept planform hydrofoils.

Conclusions

The work presented here represents the first detailed and systematic study of the effect of leading edge protuberances on hydrofoil performance. Based on the work carried out in this project, the following conclusions are drawn.

Load Measurements

The load characteristics of leading edge modified hydrofoils were compared with baseline counterparts without protuberances. Several protuberance geometries and hydrofoil planforms were examined at Reynolds numbers ranging from $9.0 \times 10^4 \leq Re_c \leq 4.5 \times 10^5$. The data revealed a number of differences between the modified hydrofoils and their baseline counterparts. Even though the load measurements were performed at several Reynolds numbers, the following statements apply for Reynolds numbers above $Re_c = 1.8 \times 10^5$ because the results were only weakly dependent on Reynolds number in this range. With this in mind, the following can be said for the force and moment measurements:

1. Whereas the baseline hydrofoils had force and moment characteristics consistent with the type of profile tested, modified hydrofoils exhibited 'soft' stall or a lack of stall in the traditional sense, and in select cases, increased maximum lift and reduced drag coefficients were observed.

2. Reynolds number has little effect on the lift and drag coefficients of all hydrofoils. Stall angle, angle of maximum lift, and maximum lift coefficient increase with Reynolds number up to $Re_c = 3.6 \times 10^5$. However, past a Reynolds number of $Re_c = 3.6 \times 10^5$ the lift characteristics change negligibly. The drag coefficient changes little over the entire range of angles for all hydrofoil planforms.

3. With the exception of the modified flipper model, which showed a lower drag coefficient than its baseline equivalent over a limited ranges of angles of attack of $17° < \alpha < 22°$, all hydrofoils showed comparable or greater drag coefficients than their baseline counterparts over all angles of attack and Reynolds numbers tested.

4. With the exception of the modified swept planform hydrofoil which had a reduced lift curve slope in the linear regime, all other hydrofoils exhibited lift curve slopes comparable to their baseline counterparts.

5. The 8S and 8M rectangular planform hydrofoils had 13% – 18% higher maximum lift coefficients than their baseline counterpart at several Reynolds numbers over the range of

angles of $16° \leq \alpha \leq 22°$. All other modified hydrofoils had a maximum lift coefficient comparable to their baseline equivalents, within the experimental uncertainty.

6. The modified flipper model showed slightly greater lift-to-drag ratio at high Reynolds numbers than the baseline model over the limited range of angles of $16° \leq \alpha \leq 22°$. The *L/D* values at these angles, however, are significantly less than the maximum values for the baseline model. All other modified hydrofoils had lift-to-drag ratios either less than or comparable to the baseline model.

7. Of all planforms tested, protuberances affect the swept planfrom most. Drag is much higher than the baseline model over the entire range of angles and Reynolds numbers. On the other hand, the lift coefficient remains nearly linear throughout the entire range of angles of attack tested. It is likely that the introduction of protuberances alters the spanwise flow over the suction side of the hydrofoil.

Flow Visualization

Particle Image Velocimetry (PIV) experiments were carried out on full-span and finite-span hydrofoils to examine the flow field and the streamwise vorticity and to determine the physical mechanisms responsible for the observed load alterations. The following conclusions can be drawn from flow visualization measurements:

1. Streamwise vorticity produced by a spanwise pressure gradient that is generated by the change in leading edge radius from peak to trough is responsible for generating lift at the higher angles of attack.

2. Neighboring streamwise vortices emanating from the leading edge of modified hydrofoils are counter-rotating and the circulation of these vortices increases with angle of attack.

3. The proximity of neighboring streamwise vortices to each other and to the hydrofoil surface causes them to interact.

4. Protuberances have little effect on the tip vortex at low angles of attack. However, depending on the Reynolds number, at high angle of attack, the additional lift generated by the modified hydrofoils is responsible for maintaining the structure of the tip vortex core past the stall angle of the baseline hydrofoil.

Cavitation

A series of tests were conducted to determine the effect of protuberances on the cavitation pattern of finite-span rectangular and swept planform modified hydrofoils. Load measurements

were also performed along with corresponding photographs and incipient cavitation number calculations. From these experiments, the following statements can be made:

1. The lift coefficient of the 4S and 4M finite-span rectangular hydrofoils is greater than the baseline hydrofoil over a limited range of angles of attack of $17° < \alpha < 22°$ under cavitation conditions. The baseline swept planform hydrofoil outperforms the modified model over the entire range of angles.

2. With the exception of the rectangular planform hydrofoils with a protuberance amplitude of $A = 0.12\ c$, drag on the modified hydrofoils remained comparable to the baseline model under cavitation conditions.

3. Still images show that cavitation on the modified hydrofoils is largely confined to the area directly behind the troughs of protuberances, whereas the baseline hydrofoils exhibit sheet cavitation over the entire span.

4. The incipient cavitation number of the baseline hydrofoil is always less than that of the modified hydrofoils, implying that for a given local static pressure, modified hydrofoils will always cavitate at lower velocities than their baseline counterparts.

5. At high angle of attack, the cavitation number of the 8L foil is much greater than all other hydrofoils tested. This is most likely due to the close proximity of protuberances, which leads to the most significant peak-to-trough pressure gradient among all hydrofoils tested.

References

Abbott, I.H. and von Doenhoff, A.E., *Theory of Wing Sections*, Dover, New York, 1959.

Coleman, H. and Steel, W., *Experimentation and Uncertainty Analysis for Engineers*, Wiley-Interscience, 1989.

Custodio, D., "The Effect of Humpback Whale-Like Leading Edge Protuberances on Hydrofoil Performance," M.S. Thesis, Worcester Polytechnic Institute, Worcester, MA, 2007.

Johari, H., Henoch, C., Custodio, D., and Levshin, A., "Effects of Leading Edge Protuberances on Airfoil Performance," *AIAA Journal*, Vol. 45, No. 11, 2007, pp. 2634-2642.

Murray, M.M., Miklosovic, D.S., Fish, F.E., and Howle, L., "Effects of Leading Edge Tubercles on a Representative Whale Flipper Model at Various Sweep Angles," *Proceedings of Unmanned Untethered Submersible Technology (UUST), UUST05, Durham*, New Hampshire, August 2005.

Pope, A. and Rae, W.H., *Low-Speed Wind Tunnel Testing,* 2nd ed., Wiley, NY, 1984, Chap. 6.

Wheeler, A.J. and Ganji, A.R., *Introduction to Engineering Experimentation,* Prentice-Hall, Inc., NJ, 1996, Chap. 7.

Publications

Custodio, D., Henoch, C., and Johari, H., "Aerodynamic Characteristics of Finite Span Wings with Leading Edge Protuberances," 50th AIAA Aerospace Sciences Meeting, Nashville, TN, January 2012, paper 2012-0054. Also, in preparation for submission to the *AIAA Journal*.

Dropkin, A., Custodio, D., Henoch, C., and Johari, H., "Computation of Flow Field around an Airfoil with Leading Edge Protuberances," *AIAA Journal of Aircraft*, to appear, 2012.

Custodio, D., Henoch, C., and Johari, H., "Flow Field on Hydrofoils with Sinusoidal Leading Edge Protuberances," in preparation for submission to an archival journal.

Presentations

Custodio, D., Henoch, C., and Johari, H., "The Flow Field on Hydrofoils with Leading Edge Protuberances," 61st Annual Meeting of the APS-DFD, San Antonio, TX, Nov. 2008, p. 64.

Custodio, D., Henoch, C., and Johari, H., "The Flow Field on Hydrofoils with Leading Edge Protuberances," 62nd Annual Meeting of the APS-DFD, Minneapolis, MN, Nov. 2009, p. 183.

Custodio, D., Henoch, C., and Johari, H., "The Performance of Finite-span Hydrofoils with Humpback Whale-like Leading Edge Protuberances," 63rd Annual Meeting of the APS-DFD, Long Beach, CA, Nov. 2010, p. 147.

Custodio, D., Henoch, C., and Johari, H., "The Flow Field Characteristics of Hydrofoils with Leading Edge Protuberances," 64th Annual Meeting of the APS-DFD, Baltimore, Nov. 2011.

Annual presentations at the ONR-ULI meeting.

Graduate Student

Mr. Derrick Custodio was the graduate student on this project, and he will complete his Ph.D. in Mechanical Engineering from WPI in May 2012.

Navy Lab Mentor

Dr. Charles W. Henoch, Hydrodynamics Branch, Naval Undersea Warfare Center, Newport, RI.